Innovative Swirl Energy Recovery Design Measures for Propeller Aircraft

Chris Hendrik Nieuwboer

Delft University of Technology

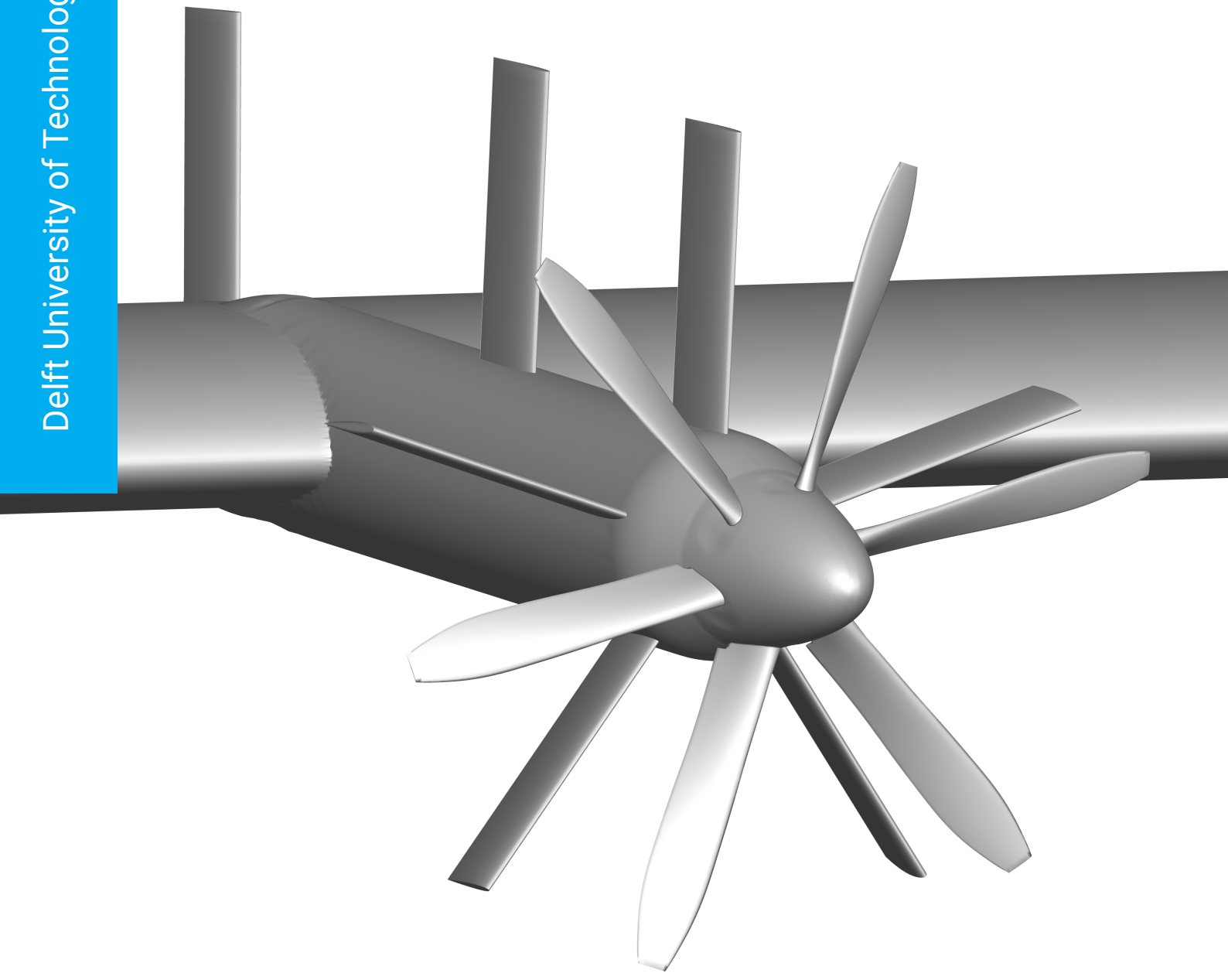

TU Delft

Innovative Swirl Energy Recovery Design Measures for Propeller Aircraft

MSc Thesis Aerospace Engineering

by

Chris Hendrik Nieuwboer

in partial fulfillment of the requirements for the degree of

Master of Science
in Aerospace Engineering

at the Delft University of Technology,
to be defended publicly on Friday July 11, 2025 at 09:30.

Student number:	5063663	
Thesis duration:	September, 2024 - July, 2025	
Thesis committee:	Dr.ir. M.F.M. Hoogreef	Chair
	Prof. dr. ir. L.L.M. Veldhuis	Supervisor
	Dr. L.T. Lima Pereira	Examiner

An electronic version of this thesis is available at https://repository.tudelft.nl/

TU Delft Delft University of Technology

This page is intentionally left blank.

Preface

This thesis report marks the end of my academic study period at TU Delft. I can proudly look back on a period filled with academic and personal growth, for which I am extremely grateful.

I would like to express my deepest gratitude towards my supervisor, Professor Veldhuis, for his guidance and insights during this project. I am truly thankful for his support during the challenging moments of this thesis. I would also like to thank my committee members, Dr.ir. M.F.M. Hoogreef and Dr. L.T. Lima Pereira for investing their time and expertise in evaluating my thesis.

Finally, I would like to extend my heartfelt thanks to my parents, sister and direct family for their unwavering support and trust in me and my academic goals, as it means the world to me. I would also like to thank my friends for their direct support and academic distractions.

Chris Hendrik Nieuwboer
Delft, July 2025

Executive Summary

Optimising aircraft engines for overall efficiency is becoming increasingly important, given rising concerns about global warming and the depletion of natural resources. As improvements in specific fuel consumption with current turbofan engines plateau, renewed interest is emerging in open rotor propeller engines. These engines allow for a higher bypass ratio, which can improve the the propulsive efficiency and thus overall aircraft performance.

An important flow characteristic in the slipstream of open rotor propellers is induced swirl, caused by the propeller torque. This rotating flow component represents a form of energy loss and should therefore be minimised. A possible design measure to improve the propulsive efficiency is to add swirl recovery vanes, as implemented in the recently introduced RISE engine from CFM International. This engine features ten stationary swirl recovery vanes, intended to improve the efficiency by up to 20 %. The implementation of the RISE engine raises an important question about the location and number of swirl recovery vanes placed on the engine. This thesis research aims to determine the optimal location for addition of swirl recovery vanes to increase the overall aircraft efficiency.

This thesis research is into two main parts. In the first part, a lower-order aerodynamic solver is selected to analyse and validate with experimental. The reference model is slightly modified to simplify the analysis and reduce the computational time. The available experimental data consists of velocity and flow parameter data at several locations, as well as two spanwise locations of pressure tabs. The outputs of the aerodynamic solver are then compared to experimental data.

It was found that the slipstream modelling, with the lower-order analysis tool, did not accurately match the experimental data. A specific wake-handling setting, related to the wake handling in close proximity to the model, significantly affected the results. The velocity ratio and total pressure coefficient are compared for this setting, leading to some important observations. The velocity ratio was underpredicted, and the total pressure coefficient overpredicted, resulting in an overestimation of propeller thrust. Both aerodynamic properties showed that the solver failed to accurately capture wake contraction and deformation. Pressure tab data on the wing's surface required a correction factor, but comparison with experimental was limited due to the sparse spanwise available data. Despite these limitations, the solver was used in the second part of this thesis, as it still allowed for a valid comparison of relative vane performance.

The second part of this thesis focuses on the design and placement of additional swirl recovery vanes on the reference model. A total of seven configurations were tested. Three axial locations behind the propeller were selected: directly behind the propeller, between the propeller and the wing's leading edge, and on the upper surface of the wing. Each axial location was evaluated with an initial vertical and an optimised vane location based on vane thrust. The final configuration represented the RISE engine, with several vanes placed directly behind the propeller. All configurations were analysed to determine the total propulsive axial efficiencies and to identify the optimal vane location.

The results show that the most efficient configuration was a vertical vane placed directly behind the propeller. A second vane, located slightly farther aft, performed marginally worse, indicating that the axial distance between the propeller and van has a limited effect on the overall performance. Both the initial and optimised vane placed on the upper surface of the wing performed the worst, due to flow interactions with the wing and distorted inflow conditions. It was additionally observed that interaction effects between aerodynamic components had a significant impact on the overall performance, and that vane performance could not be linearly superimposed to estimate multi-vane efficiency gains.

Contents

List of Figures

List of Tables

List of symbols and abbreviations

Abbreviations

AoA	Angle of Attack
APIAN	Advanced Propulsion Integration Aerodynamics
AR	Aspect Ratio
avg	Average
BPR	Bypass Ratio
CAD	Computer-Aided Design
CFD	Computational Fluid Dynamics
CRORP	Counter-Rotating Open Rotor Propeller
EXP	Experiment
Ff	Force factor
FS	Flightstream
GE	General Electric
LLT	Lifting Line Technology
OpenVSP	Open Vehicle Sketch Pad
opt	Optimal
RANS	Reynolds Average Navier Stokes
RISE	Revolutionary Innovation for Sustainable Engines
RPS	Rotations Per Second
SFC	Specific Fuel Consumption
SPA	Surface Proxmity Avoidance
SRV	Swirl Recovery Vane
VLM	Vortex Lattice Model

Greek Symbols

α	Angle of attack	[deg]
α_{eff}	Effective angle of attack	[deg]
β	Blade pitch angle	[deg]
β_{side}	Side-slip angle	[deg]
η_x	Axial propulsive efficiency	[%]
η_p	Propulsive efficiency	[%]
$\eta_{x,tot}$	Total axial propulsive efficiency	[%]
Γ	Circulation	$[m^2/s]$

λ	Taper ratio	[-]
μ	Dynamic viscosity	[kg/m $\cdot s$]
ϕ	Helix angle	[deg]
ρ_∞	Air density	[kg m^{-3}]

Latin Symbols

A_D	Actuator disk area	[m^2]
b_w	Wing span	[m]
c	Chord length	[m]
C_L	Lift coefficient	[-]
C_l	Sectional lift coefficient	[-]
C_P	Power coefficient	[-]
C_p	Pressure coefficient	[-]
C_T	Thrust coefficient	[-]
$C_{D,i}$	Induced drag coefficient	[-]
$C_{P,T}$	Propeller thrust coefficient	[-]
c_{ref}	Reference length	[m]
c_r	Root chord	[m]
Cp_T	Total pressure coefficient	[-]
D	Propeller diameter	[m]
d	Characteristic length	[m]
D'	Sectional drag force	[N]
F'	Sectional resultant force	[N]
h/c	Maximum airfoil camber	[-]
h_p/c	Location of maximum airfoil camber	[-]
J	Advance ratio	[-]
L	Lift force	[N]
L'	Sectional lift force	[N]
M	Mach number	[M]
n	Propeller rotational speed	[RPS]
P	Propeller power	[W]
P_C	Power coefficient velocity based	[-]
P_s	Static pressure	[Pa]
P_T	Total pressure	[Pa]
P_x	Pressure	[kg/m s^{-2}]

Q'	Sectional force in the propeller plane	[N]
q_∞	Dynamic pressure	[kg/m s^{-2}]
q_{AD}	Actuator disk dynamic pressure	[kg/m s^{-2}]
R	Radius	[m]
r	Radial distance	[m]
Re	Reynolds number	[-]
S	Surface area	[m^2]
T	Thrust force	[N]
T'	Sectional thrust force	[N]
t/c	Maximum airfoil thickness	[-]
T_C	Thrust coefficient velocity based	[-]
t_p/c	Location of maximum airfoil thickness	[-]
T_x	Axial thrust component	[N]
T_{temp}	Temperature	[K]
V	Velocity	[m/s]
$V^{*'}$	Outflow velocity	[m/s]
V^*	Inflow Velocity	[m/s]
V_a	Axial velocity	[m/s]
V_e	Exhaust velocity	[m/s]
V_t	Tangential velocity	[m/s]
V_x	Velocity in x-direction	[m/s]
V_y	Velocity in y-direction	[m/s]
V_z	Velocity in z-direction	[m/s]
V_∞	Free stream velocity	[m/s]
X, Y, Z	Global axis system	[-]
x, y, z	Local axis system	[-]

Subscripts

n	Nacelle
p	Propeller
R	Reference
v	Vane
w	Wing

1

Introduction

An ever-evolving sector like the aviation industry strives towards perfection and the most optimal designs. The main development drivers in civil aviation were initially speed, range and comfort, but have shifted in recent history to a more environmentally oriented mindset. A reason for this is global warming and the depletion of natural resources [1].

Reducing the Specific Fuel Consumption (SFC) has always been an important driver for the development of new aircraft engines. The reason for this was the associated operational cost for the airlines, as a reduced fuel consumption increases profit. It has become even more important with the increasing price of kerosene and the just-mentioned concerns regarding global warming [2]. Improvements in the SFC of aircraft engines and the fuel consumption per passenger can be seen in Figure 1.1. This graph shows, especially in the mid-to-late nineteenth century, a significant reduction in engine fuel consumption. A more efficient turbofan was introduced during this period, for which the efficiency increments now seem to decrease. The increased efficiency from these turbofan engines was mainly a result of the higher Bypass Ratios (BPR) of these new engines.

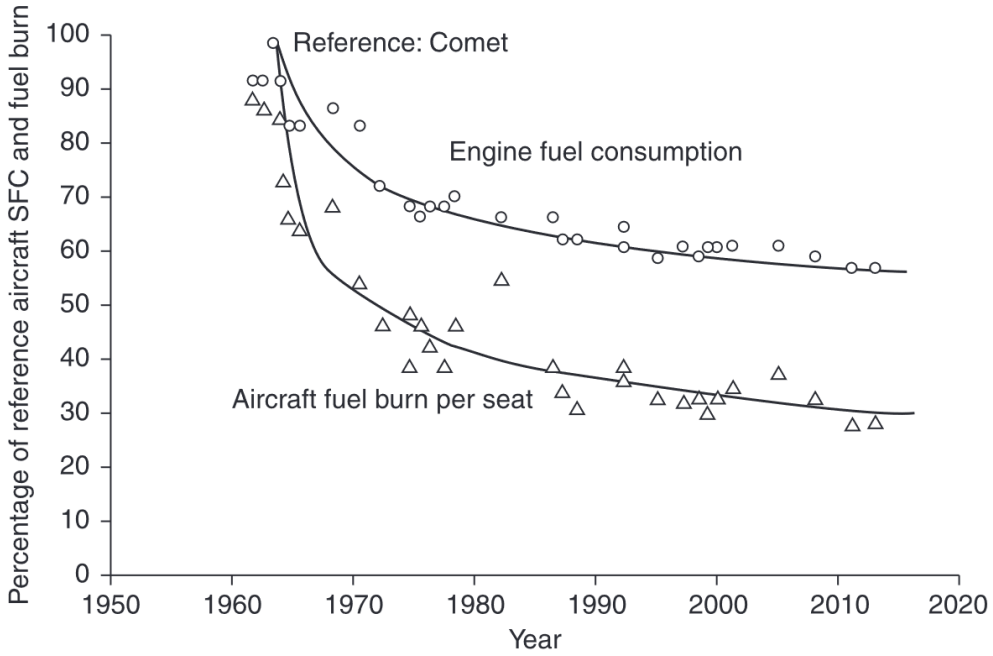

Figure 1.1: *Aero gas turbine fuel consumption and fuel consumption per seat evolution between the* 1950 *and* 2020 *[2]*

Propfans or open-rotor propeller engines have, relative to turbofans, an even higher BPR [3]. A higher BPR means that, for the same thrust, a larger volume of air can be accelerated by a smaller amount. The effect this has on the propulsive efficiency can be seen in Equation 1.1 [4]. In this equation, the propulsive efficiency is presented as a function of the engine exit velocity V_e and free stream velocity V_∞. The highest efficiency is reached when the difference between the exhaust velocity and airspeed is the smallest. It is for this reason that recent interest in larger open-rotor propeller engines has picked up again [5].

$$\eta_p = \frac{2}{1 + \frac{V_e}{V_\infty}} \tag{1.1}$$

This thesis research is related to improving the propulsive efficiency of open-rotor propeller engines. Figure 1.2 shows typical axial and tangential velocities in the propeller slipstream. An axial and tangential flow component within this slipstream are respectively denoted with V_a and V_t. The tangential velocity component results in a rotating flow around the propeller hub, which is called propeller swirl. Wang et al. [6] discusses propeller swirl losses of a propeller at 0.8 M, which accounted for 7-11 % of the total loss. It is possible to increase the propulsive efficiency of open-rotor propellers by reducing this swirl component in the propeller slipstream. Reducing the swirl velocity will add to the axial exit velocity of the propeller slipstream, thus improving the propeller efficiency.

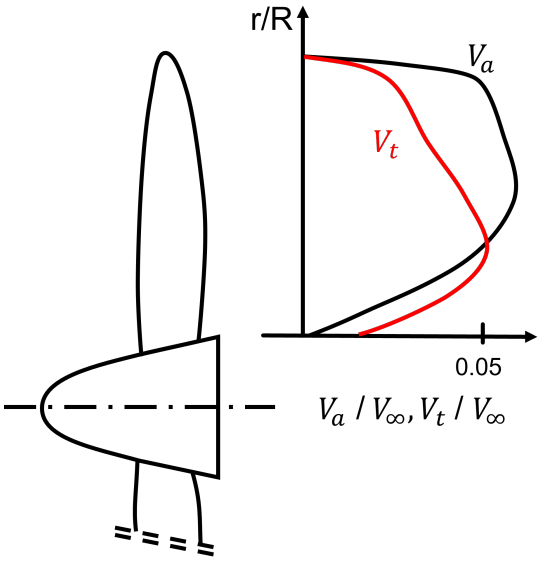

Figure 1.2: *Typical radial distribution of axial and tangential velocities of a lightly loaded propeller (changed from [7])*

An example of a swirl-reducing design measure is the Counter-Rotating Open Rotor Propeller (CRORP). NASA investigated this concept of counter-rotating propellers and found that the propeller swirl could be reduced by up to 8 % [8, 9]. This proposed counter-rotating propeller would, however, have some disadvantages. The two main downsides are the increased complexity, leading to an increased weight [10, 11] and a significant noise penalty [12, 13, 14]. The latter is because of the unsteady flow interactions between the first and second set of rotors.

The counter-rotating propeller utilises a second row of propeller blades, spinning in the opposite direction, to redirect the swirl in the propeller slipstream [15]. Another design option would be to include stationary vanes instead of rotating blades. This would, similarly to the counter-rotating propeller, reduce the propeller swirl, but is lighter and less complex. An example of a newly developed aircraft engine incorporating these so-called Swirl Recovery Vanes (SRV) is the Revolutionary Innovation for Sustainable Engines (RISE) engine as presented in Figure 1.3. The RISE engine program started in 2021 and is a joint venture between General Electric (GE) and Safran to develop the next-generation open-rotor aircraft engines with lower fuel consumption and emissions. An efficiency increase by up to 20 % is aimed for with this engine at 0.8 M, similar to current turbofan engines [4]. The incorporation of SRVs is the topic of many recent research papers, as will be discussed in Section 2.4.

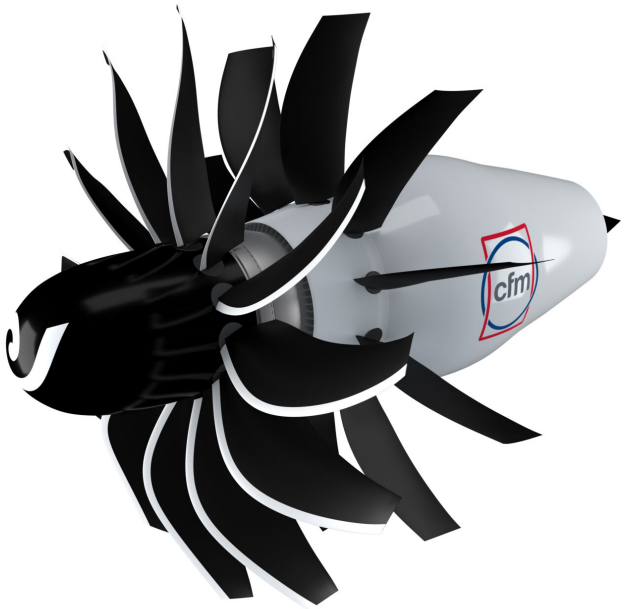

Figure 1.3: *CFM International RISE engine with* 12 *highly loaded propeller blades and* 10 *stationary SRVs [4]*

The vanes on the RISE engine are placed on the nacelle, which, in a regular tractor propeller configuration, would be placed in front of the wing. The wing itself naturally plays a part in the recovery of swirl in the propeller slipstream, as it is, in essence, a large horizontal vane. Vanes placed in front of the wing will affect the airflow over the wing and add to the swirl recovery effect of the wing. This is important to note as the combined effects should be optimised for optimal performance, which will be discussed in detail in Section 2.3.

Additional vanes would, in theory, allow for better propulsive efficiency, as they would create thrust without requiring any additional energy input. Adding one or more additional vanes could, however, also have some disadvantages. The presence of a vane in front of the wing, for example, could affect the aerodynamic performance of the wing, resulting in an overall less efficient configuration. There are also structural considerations that need to be accounted for, such as the added weight and structural integrity. This all leads to a more complex design, which was determined to be a drawback for the CRORPs.

A remaining question is thus whether the current implementation of SRVs of the RISE engine is the most effective design measure to reduce propeller swirl and increase the propulsive efficiency, or if there are other, more effective design options. This question is the foundation for this thesis research and presents a knowledge gap related to the optimal position of swirl recovery vanes. The research objective for this thesis considers multiple different swirl recovery locations and is formulated as stated below:

The research objective is to determine the most optimal SRV location for total efficiency increase of a propeller aircraft by analysis/modelling of swirl recovery vanes.

1.1. Research Questions

The research question for this thesis is formulated based on the thesis objective statement presented above. The research question will contribute to the research objective and link the problem, methods, theoretical framework, and conclusion. The research question for this thesis is formulated as presented below.

To what extent can the effectiveness of swirl recovery design in open-rotor propeller aircraft be improved utilising a lower-order aerodynamic solver by implementation and careful placement of swirl recovery vanes on the nacelle or wing?

This research question is rather broad and consists of multiple elements. The research question is, for this reason, divided into sub-questions to answer the posed research question more clearly:

1. How well does a low-mid fidelity aerodynamic analysis tool capture the aerodynamic phenomena involved in the propeller slipstream?
2. What is the effect of implementing Swirl Recovery Vanes on the overall propulsive efficiency of an aircraft with an open-rotor propeller?
3. Can the vane thrust contribution of individual SRVs, placed in the propeller slipstream, be added to accurately predict the overall aerodynamic performance of a multi-vane configuration?
4. What is the optimal SRV placement for the generation of thrust and propulsive efficiency?

These sub-questions will be answered individually, helping to answer the research question. This will, in turn, allow for the research objective to be fulfilled.

1.2. Research Significance and Scope

The concept of SRVs is a relatively new area of research, but is well-represented in current research. Previous papers discuss the potential in great detail by considering different energy recovery design measures as well as positions, based on several analysis methods. A detailed description of these papers will be discussed in Chapter 2, of which the significance for this research is presented below. The papers reach slightly different conclusions on how effective an additional SRV is to the overall performance because of different methods and geometric models used. These aspects are crucial for the understanding of swirl recovery and determining the propulsive efficiency gain potential, to which this research aims to contribute.

A low-mid fidelity approach is important to note for this research, as the required computational time for such a method is significantly lower compared to a full Reynolds Average Navier Stokes (RANS) Computational Fluid Dynamics (CFD) analysis. The results of this research will indicate the analysis accuracy of lower-fidelity solvers and whether these solvers could potentially be used in an initial optimisation, reducing the development time. The potential of swirl energy recovery design measures could have a large impact on future aircraft and currently operating propeller aircraft. Newly designed aircraft could incorporate SRVs to increase propulsive efficiency. The same is true for operational propeller aircraft by retrofitting these aircraft.

The main focus of this research is to determine the ability of a low-mid fidelity aerodynamic analysis to correctly model the aerodynamic phenomena present in the propeller slipstream and thereby determine the optimal vane position. This will be done for a single propeller, nacelle and wing configuration in the low subsonic regime and relatively low blade loading. The reason for this is the available experimental data for this particular configuration, as will later be discussed in Chapter 3. The author recognises that this application is rather limited and only valid for comparable models, but the method and results would be sufficient to answer the posed questions and form a sound base for future research.

1.3. Report Structure

This thesis report is divided into seven chapters, as presented in Figure 1.4 below. Chapter 2 starts with describing background information necessary to understand the contents of this thesis. The methodology used to answer the posed research question is then described in Chapter 3. Chapter 4 presents the validation performed on the used aerodynamic solver and model, after which the model modifications for different configurations are discussed in Chapter 5. The results of this thesis research are presented in Chapter 6. This report concludes with Chapter 7, where the research questions are answered and some recommendations are presented for this and future work

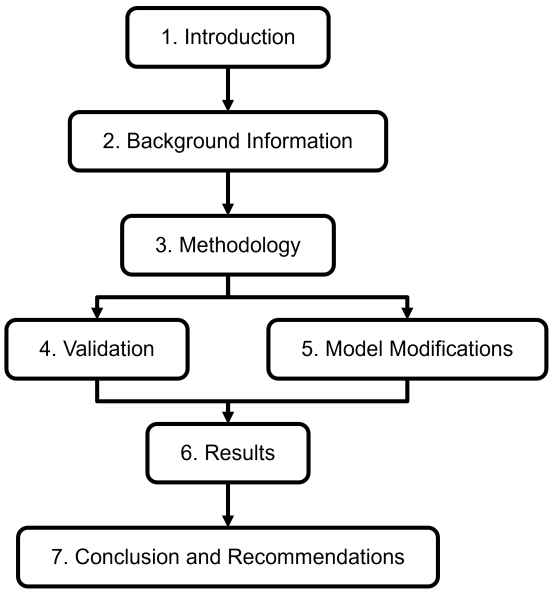

Figure 1.4: *Visual flowchart representation of the report structure for this thesis work*

2

Background Information

This chapter presents the background information necessary to understand the contents of this thesis work. First, general propeller aerodynamics are discussed in Section 2.1, which is a fundamental part of this thesis. This section is followed by an extensive explanation of the most important aerodynamic interactions between the propeller slipstream and aerodynamic surfaces in Section 2.2. Section 2.3 discusses how swirl energy recovery works and is followed by Section 2.4, where the results of several research papers are discussed. Section 2.5 concludes this chapter by discussing propeller performance parameters and the propeller swirl efficiency effect.

2.1. Propeller Aerodynamics

The general purpose of a propeller is to generate thrust by adding momentum to the slipstream behind the propeller [16]. The airflow over the propeller blades, which create this thrust, can be compared to a regular aircraft wing, as is depicted in Figure 2.1. The incoming airspeed of the propeller blade (denoted by V^*) is the result of the free stream velocity V_∞, axial induced velocity V_a and the radial induced velocity V_t. These induced velocities are the result of the acting forces on the airflow and streamlines, as discussed in [17]. The angles β, ϕ and α_{eff} are respectively the blade pitch angle, helix angle and effective angle of attack as presented in the figure. The sectional resultant force F' can be decomposed into a sectional lift and drag component (L' and D') or thrust and planar force (T' and Q'), as presented in the figure.

The propeller blades deflect the stream tube behind the propeller blade and create a thrust and a so-called swirl component. This swirl velocity originates from the flow not being aligned with the free stream velocity, which is a form of energy loss and should be minimised [16].

It should be noted that the propeller rotation causes the propeller slipstream to have a spanwise (V_y) velocity component above and below the spinner. This velocity causes the slipstream on the upper and lower surfaces of the wing to move spanwise in opposite directions. This relative spanwise shift in the propeller slipstream is explained in great detail by Ribeiro et al. [18], where the propeller slipstream and wake development were analysed. The findings of this work can be seen in Figure 2.2, where the propeller rotation determines the direction of the relative spanwise shift. The shown deformation is, in this image, also affected by the wing and flap settings as specified in the figure caption. The propeller slipstream development is important for this thesis research, as the aim is to determine the optimal SRV location. The location of the vanes should be considered carefully with this slipstream spanwise shift in mind before any meaningful analysis can be performed.

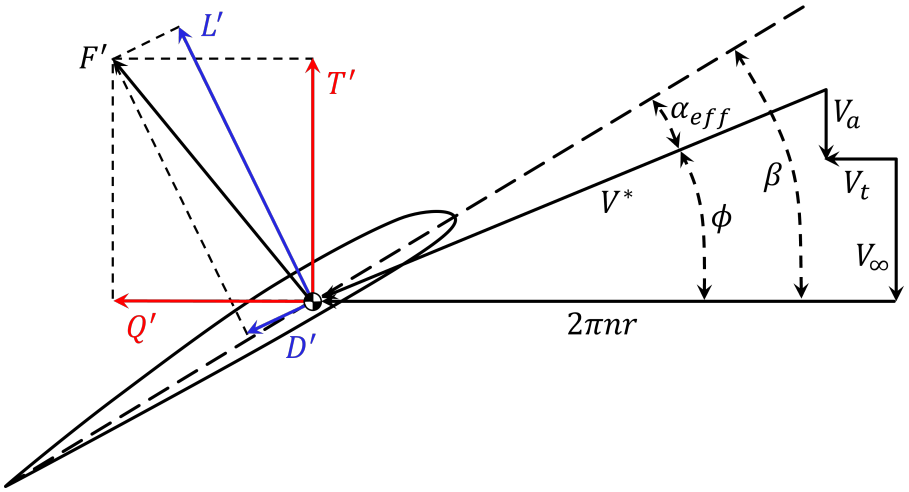

Figure 2.1: *Sectional propeller blade velocity diagram with resultant and decomposed forces (changed from [17])*

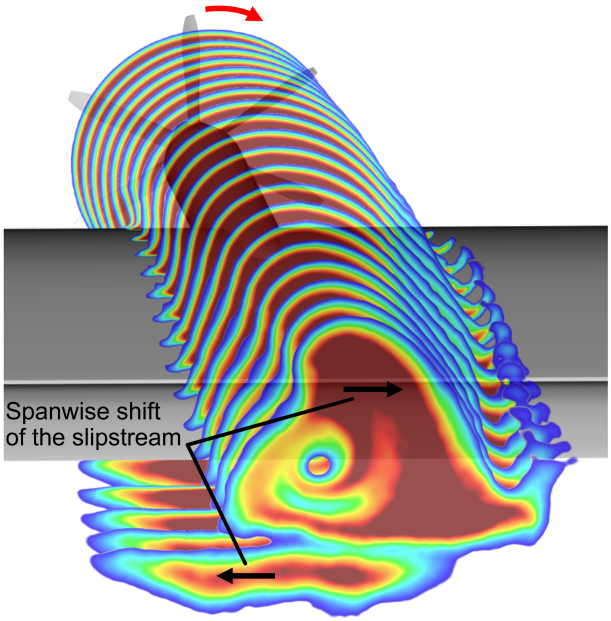

Figure 2.2: *Time averaged total pressure slices showing the propeller slipstream deformation as as result of swirl velocity for a model at an angle of attack at* 8° *and a flap element at* 15° *(changed from [18])*

2.2. Propeller Slipstream Interactions

The slipstream, as discussed earlier, will influence several aircraft components. These aerodynamic interactions will affect the lift and handling of an aircraft and should therefore be taken into account. This section discusses the key interactions of the propeller slipstream and aircraft components. Subsection 2.2.1 first discusses the interactions between the propeller slipstream and the nacelle, after which Subsection 2.2.2 continues with the propeller-wing interaction. The interactions with possible swirl recovery systems are discussed later, as this chapter focuses solely on the required background information.

2.2.1. Propeller-nacelle Interaction

The nacelle is the body that attaches the propeller to the wing or aircraft fuselage and is often the enclosure for the engine itself. The nacelle shape can significantly affect the velocity and pressure distribution of the propeller as described by Samuelsson [19]. Samuelsson showed that nacelle shape variations close to the propeller affect the propeller inflow conditions. This indicates that optimising an isolated propeller would not guarantee an optimal propeller design when integrated.

Three different propeller-nacelle interaction effects are presented in Figure 2.3. Figure 2.3a shows how the presence of a nacelle reduces the local axial velocity V_a, which in turn will change the blade loading. Figure 2.3b shows how a large Angle of Attack (AoA) will, comparable to a flat plate or wing, cause a change in local angle of attack of the propeller blade. This change in AoA adds to the already established AoA of the propeller relative to the aircraft orientation. Figure 2.3c is related to the specific case of push propellers, where the nacelle itself could create a vortex pair at high angles of attack. These vortices would then be ingested by the propeller, affecting the flow significantly. [20]

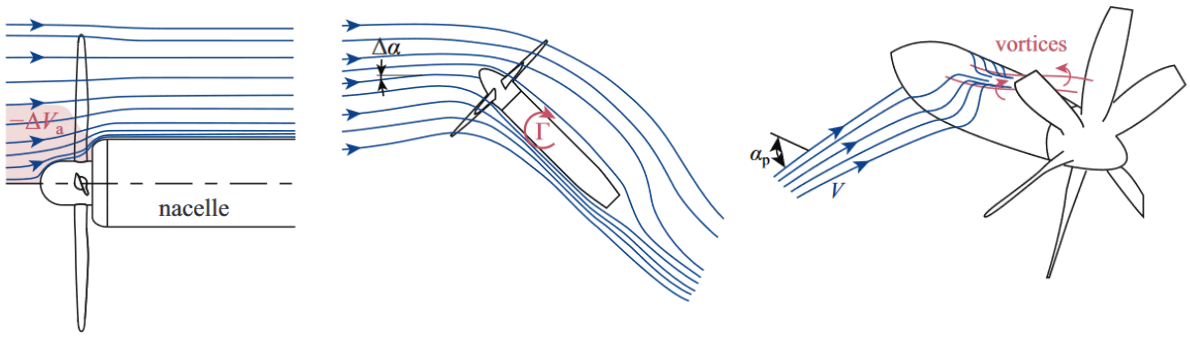

(a) *Upstream V_a reduction* **(b)** *Upstream change in α* **(c)** *Formation of a vortex pair on the nacelle*

Figure 2.3: *propeller-nacelle interaction effects, reduced velocity (a), change in AoA (b), and vortex pair (c) [20]*

2.2.2. Propeller-wing Interaction

The slipstream of a propeller affects the wing lift distribution to a large extent in a propeller tractor configuration. This is because the propeller is positioned in front of the wing [7]. The slipstream of a propeller consists of a swirl/tangential and axial component as previously discussed in Section 2.1, which will both affect the wing lift distribution. The individual and combined slipstream effects are depicted in Figure 5.6. Figure 2.4a shows how the propeller slipstream increases the wing lift at both the inboard and outboard side of the propeller due to an increase in the axial velocity. This is because of the increased dynamic pressure q_∞ behind the propeller [7]. The effect of the slipstream swirl/tangential component on the wing lift is presented in Figure 2.4b. The swirl effect is, contrary to the axial component, not symmetrical. The upward-going blade will generate a velocity component in the positive z-direction, increasing the local angle of attack and thus the lift. The downwards-going blade has an opposite effect and reduces the local AoA, decreasing the local lift contribution on this side of the propeller. The combined propeller effects on the spanwise wing lift coefficient can be seen in Figure 2.4c. The effects of both the inboard-up and outboard-up propeller rotations extend further than the propeller diameter in the regions W-I and W-IV. This is because of the distorted vorticity sheet leaving the wing. The increased dynamic pressure

and tangential slipstream of the propeller influence both W-II and W-III. The effect of the slipstream swirl, in case the propeller rotates inboard-up, would counteract the increase in lift coefficient in W-III. This results in a lower lift coefficient but differs relatively little from the isolated wing. [7]

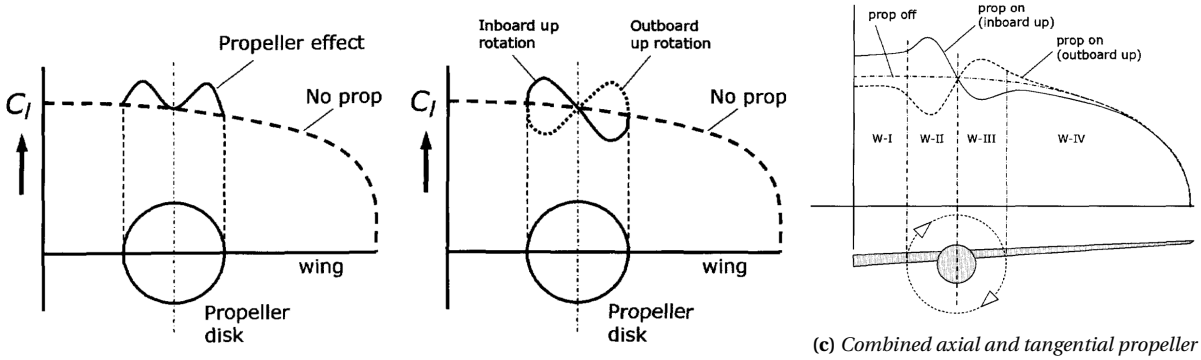

(a) *Axial propeller slipstream effect on the spanwise lift coefficient*

(b) *Tangential propeller slipstream effect on the spanwise lift coefficient*

(c) *Combined axial and tangential propeller slipstream effects on the spanwise lift coefficient*

Figure 2.4: *Propeller-wing interaction effects on the spanwise lift distribution as a result of the propeller slipstream shown for axial (a), tangential (b) and combined (c) effects compared to an isolated wing at an angle of attack of* 0° *[7]*

2.2.3. Upstream Effect

It is important to note that the propeller inflow conditions are also affected by the aerodynamic components downstream of the propeller. The wing, for instance, increases the local AoA because of the wing's upwash effect. A vane would, similarly to the described upstream effect as presented in Figure 2.3a, change the propeller inflow conditions when placed in close proximity to the propeller. It is difficult to isolate the individual effects influencing the propeller, but should be kept in mind when interpreting the results.

An important relation between the propeller inflow conditions and performance is presented in Figure 2.5. This graph shows the relationship between the propeller propulsive efficiency and so-called advance ratio (J). The advance ratio is a non-dimensional propeller parameter, relating the distance travelled during one propeller rotation to the propeller diameter [21]. The equation for the advance ratio can be seen in Equation 2.1. In this formula, V_∞ is the incoming free stream velocity in m/s, n is the rotational speed of the propeller in Rotations Per Second (RPS), and D is the propeller diameter in meters.

It can be seen that the efficiency of a propeller increases when the advance ratio increases until a certain maximum efficiency. This initial increase in efficiency is due to the operating conditions approaching optimal conditions for thrust generation for a particular propeller blade profile. The efficiency decreases when the advance ratio is increased past this optimum because the effective angle of attack would become negative [21]. This means that the propeller is essentially becoming a turbine, reducing the total energy of the flow instead of adding energy. The specific inflow conditions, affected by upstream effects, change the local advance ratio and, therefore, the propeller performance.

$$J = \frac{V_\infty}{nD} \tag{2.1}$$

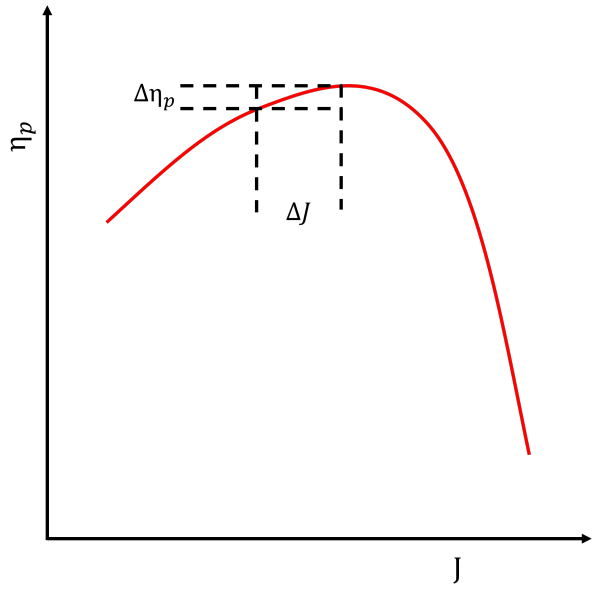

Figure 2.5: *Schematic representation of the relation between the propeller advance ratio and propulsive efficiency*

2.3. Swirl Energy Recovery

Swirl energy in the propeller slipstream can be extracted from the flow and converted into additional thrust using an SRV. Figure 2.6 shows a schematic figure of how this works. The inflow conditions are shown on the left-hand side of the figure, where the free stream, axial induced propeller and tangentially induced propeller velocities are respectively denoted by V_∞, $V_{a,p}$ and $V_{t,p}$. The tangential velocity behind the vane is reduced as a result of the tangential velocity induced by the vane ($V_{t,v}$), which is in the opposite direction of the propeller-induced tangential velocity. The resultant thrust force is presented in this figure, as well as the decomposed and thrust components. [15]

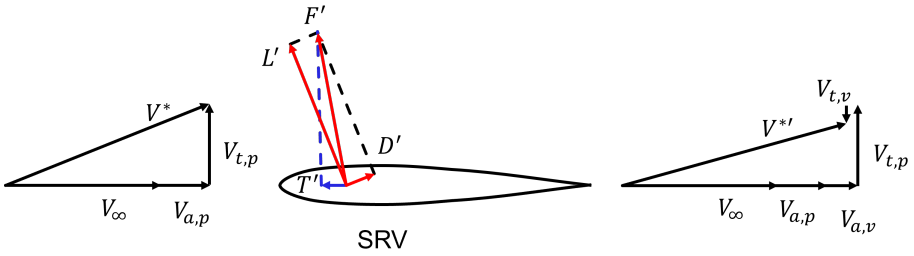

Figure 2.6: *Illustration of how an SRV extracts propeller swirl and generates thrust from inflow conditions when being placed in the slipstream of a propeller (changed from [15])*

An observant reader will recognise that the shape and location of an SRV are practically identical to where a wing could be located. This is a comparable situation, where the induced tangential velocity of the propeller, on the blade upwards-going side, will result in a local higher AoA and, on the blade downwards-going side, a lower/negative AoA. Figure 2.7 shows how a wing will perform a similar role as the just-mentioned vane in the propeller slipstream.

The situation as presented in Figure 2.6 is identical to the situation on the blade upwards-going side but with induced axial and tangential wing velocities, denoted by subscript w. The wing will contribute to the swirl energy recovery on the blade's upwards-going side. The velocities as seen in cross section A-A on the blade's downwards-going side show an opposite effect. The sectional lift decreases, and the drag increases because of the backwards tilt of the force vector [22]. The effectiveness of an SRV or wing element is thus dependent on the inflow conditions and relative positioning to the propeller. The findings of other papers on the topic of swirl energy recovery are discussed in Section 2.4 below. This

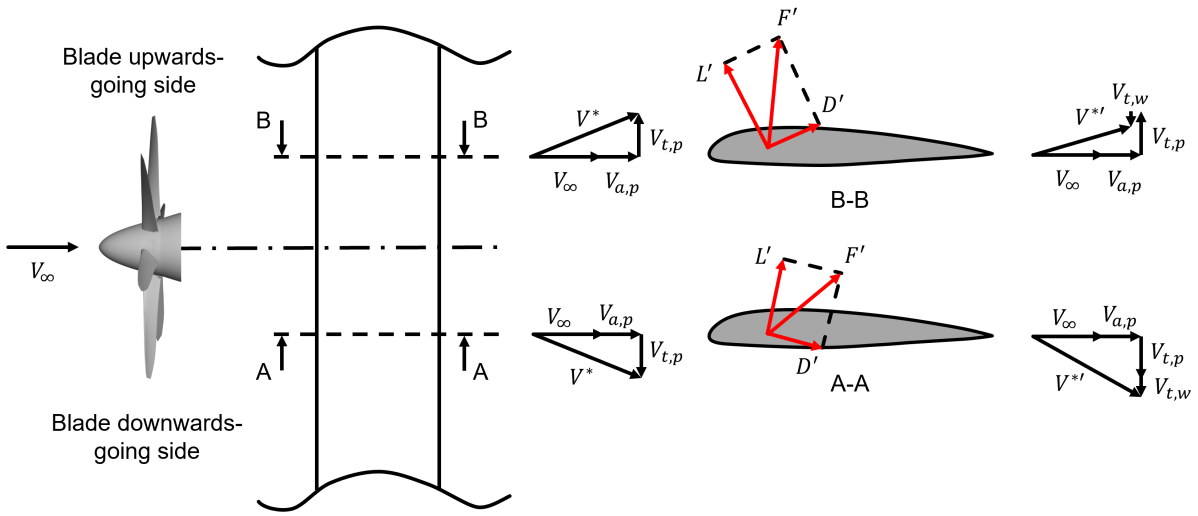

Figure 2.7: *Figure showing the swirl recovery contribution of a wing at* 0° *AoA in the slipstream of a propeller, with the cross-sectional velocities and forces presented for the propeller upwards- and downward-going side (changed from [15])*

2.4. Previous Research

The relatively new concept of SRVs is the topic of several previously published research papers. The two most important aspects to consider are the effectiveness of this design measure and the positioning of these additional vanes. This section discusses previously performed research in this field. Subsection 2.4.1 first discusses two papers regarding the most optimal design aspects of kinetic swirl energy loss optimisation. Subsection 2.4.2 then continues with a discussion on the optimal SRV positioning.

2.4.1. Kinetic Energy loss design measures

Stokkermans [23] performed, in his master thesis, an analysis on an isolated propeller with SRVs, as well as a combination of a wing-mounted tractor propeller. The model used for the combined wing-mounted tractor propeller is shown in Figure 2.8. The propeller in this model is the 6-bladed propeller from the European Advanced Propulsion Integration Aerodynamics and Noise (APIAN) project [3]. The wing is based on the Fokker F50 wing, which was scaled to match the relative dimensions of the propeller. The isolated propeller-SRV results show that the propulsive efficiency could be improved with the incorporation of SRVs by up to 4.53 % for a design with 9 vanes in high-trust conditions. The vanes were in Stokkermans' thesis, optimised for maximum vane thrust by using a modified lifting line code for

an isolated propeller-nacelle and SRV case, as this was determined to be the most effective. It was found that the propulsive efficiency increased the most when the SRV thrust was maximised instead of minimising the propeller slipstream swirl. The highest efficiency increase was found in high-lift conditions, where the results were found to be more accurate for higher advance ratios compared to lower ratios. The last part of his thesis describes the effect of adding a wing to this isolated propeller system. It was assumed that the effect of adding a wing would be very small, but this was incorrect. The inflow conditions of each of the SRVs would change due to the upwash effect of the wing, resulting in a degraded SRV performance. The combined configuration had a total efficiency increase of 2.14 %, which is much lower than the efficiency obtained for the isolated propeller-SRV configuration. It was thus concluded that the wing should be included in the optimisation for propulsive efficiency and that each of the SRV blades should take into account the upwash effects of the wing.

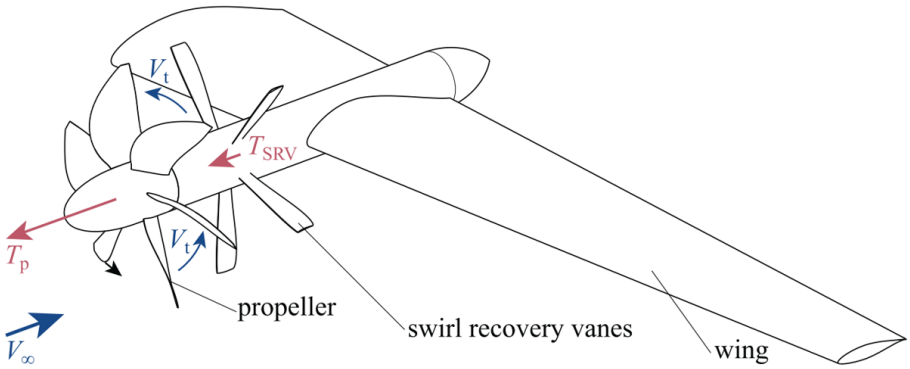

Figure 2.8: *Figure showing Stokkermans' APIAN propeller an Fokker F50 wing combined model [20]*

Stokkermans et al. [24] performed a later study on the same model, comparing two design concepts to increase the overall propulsive efficiency. The first concept was to utilise the principle of boundary layer ingestion by analysing a pusher propeller mounted at the aft fuselage in the wake. This was done to minimise the axial kinetic energy loss and resulted in a power benefit of 7 %. The second was to analyse a complete model with SRVs to determine the difference between the analysis of an isolated propeller and propeller-wing combination, as was also discussed in [23]. The results once again confirmed the conclusion, as stated in Stokkermans' thesis, that the wing and individual SRV blades should be included in the analysis.

2.4.2. SRV positioning and Design

The results from the papers in the previous subsection show the importance of designing the aerodynamic system in its entirety. This subsection continues by discussing the importance of vane positioning as discussed in other papers.

Several research papers looked into the effect of SRV placement on the overall propulsive efficiency and performance. The papers seem to agree that the distance between the propeller blades and the swirl recovery vane (axial position) has a negligible impact on the overall propulsive efficiency when modelling the propeller and vanes. Yamamoto [25] and Miller

[26] both used a three-dimensional Euler code and found that SRVs were able to recover about half of the swirl energy loss, independent of the relative axial positions tested. The close and far axial spacing between the propeller and vanes, as used by Miller, can be seen in Figure 2.9 below. The model features twelve vanes, which are slightly tapered and have NACA 16-series airfoil sections. The red arrows represent the distance between the pitch axis of the propeller blades and vanes in relation to the propeller diameter D_p.

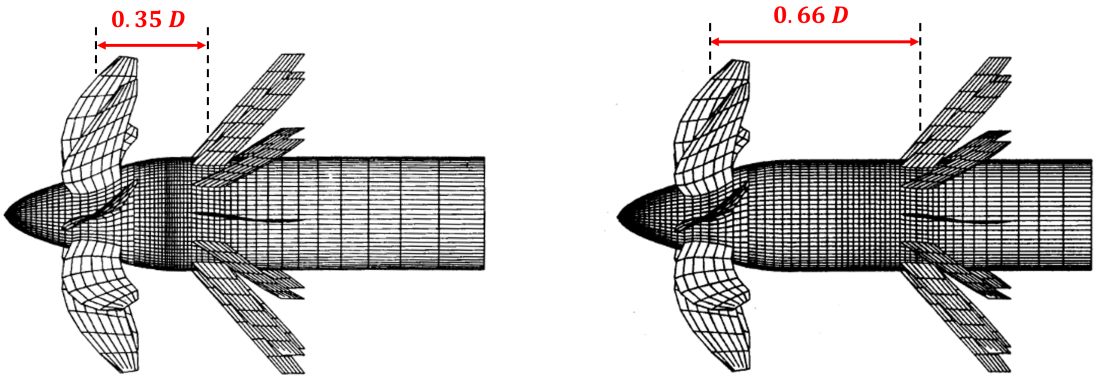

(a) *Near propeller-vane spacing with a distance of* 0.35 D

(b) *Far propeller-vane spacing with a distance of* 0.66 D

Figure 2.9: *Figure showing the model used by Miller to determine the effect of axial distance between the propeller and vanes, with near propeller-vane spacing of* 0.25 D *(a) and far propeller-vane spacing of* 0.66 D *(b) (changed from [26])*

Li et al. [22] considered several aspects of the optimal SRV placement. These were: the axial position, azimuthal position and blade count. A multi-fidelity optimisation procedure determined that the most optimal position for an SRV would be downstream of the wing on the blade's downwards-going side. This was because placing a vane in front of the wing deteriorated the wing's performance by increasing the induced drag of the wing. The induced velocity downstream of the wing on the blade upwards-going side would have a lower angular velocity due to the wing-induced velocity, meaning that this placement would also be sub-optimal compared to the blade downwards-going side. A disadvantage of placing an SRV at this location is that the SRV generates downforce instead of lift, which has to be compensated by the wing. The results of this paper can be seen in Figure 2.10 below. Figure 2.10a shows the performance of the SRV versus the axial distance of the vane downstream of the wing. It can be seen that the total performance increases with the addition of an SRV and that the total performance is highest when the distance between the wing and vane is smallest. Figure 2.10b shows how the performance of multiple SRVs are related to each other with the azimuthal positions as presented below the figure. The total drag count of the model decreases with adding vanes.

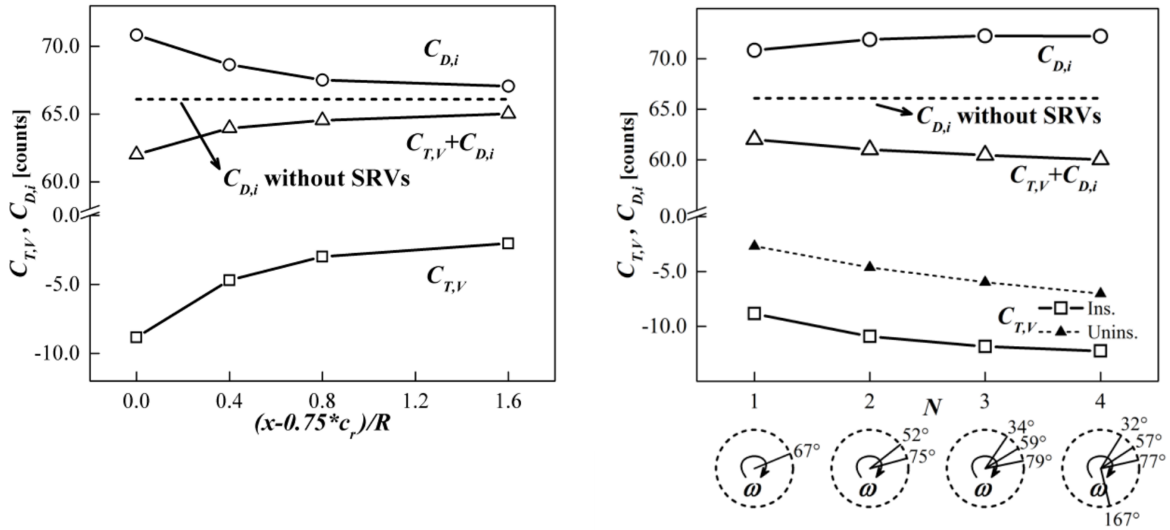

(a) *Relationship between the total drag count and axial distance between the trailing edge of the wing and vane*

(b) *Total drag count comparison for configurations with several vanes compared to a clean model without vanes*

Figure 2.10: *Figure showing the results found by Li et al. for the relation between the axial vane position and model drag counts compared to a vaneless model (a) and the relation between the number of vanes and total drag count (b) [15]*

Wang et al. [6] found similarly to Yamamoto and Miller that the axial distance between the propeller and SRV had little influence on the total performance. Wang however also considered the effect of blade tip-chord ratio on the swirl energy recovery performance. Three blade geometries, presented in Figure 2.11, were evaluated, where the tip-chord ratios for model $V1$, $V2$ and $V3$ were respectively 1, 2 and 3. The vane span was for this tip-ratio research equal to 0.92 R to prevent the possible interactions of tip-vortices. It was found that the most divergent blade shape had the most uniform outflow at multiple advance ratios but a lower overall efficiency due to a larger observed absorbed power.

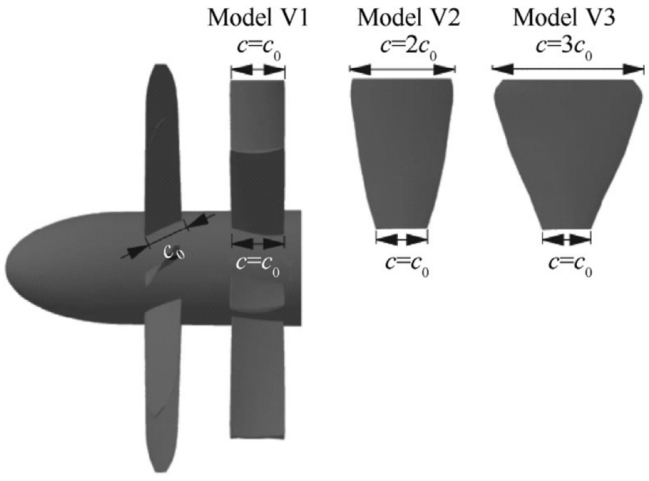

Figure 2.11: *Figure showing the model configurations used by Li et al. to determine the effect of tip-chord ratio on the overall efficiency, where the vanes are positioned at an incidence angle of* 2.5° *and have a span equal to* 0.92 R *to avoid tip vortex interactions [6]*

Most of the previously mentioned papers were performed with SRVs of the same length. Avallone et al. [27] considered in their work the effect of two SRV vane lengths to determine the difference in performance. The baseline case and corresponding experimental data were taken from Wang et al. [6] and had an SRV vane length equal to the propeller radius. This setup had an increased propulsive efficiency of 2.4 % with respect to the isolated propeller. The SRV blade tips contributed to approximately 1.9 % of the SRV thrust, and it was assumed that reducing the length would thus only have minimal effect on the overall propulsive efficiency. Shortening the SRV blade lengths would also prevent the propeller tip vortices from impinging on the SRV blades and reduce the unsteady noise. Both of these assumed effects were, however, proven incorrect, as the model with a shorter SRV blade of 0.84 R had a reduced propulsive efficiency by 13 % and no significant far-field noise reduction was observed.

2.5. Propeller Performance Parameters and Swirl Recovery

There are a number of important parameters to consider regarding the individual and overall propulsive performance of an aircraft model. This section describes which parameters are of interest for this thesis research. The advance ratio, as discussed in Subsection 2.2.3, is one of these parameters but will not be repeated in this section.

The propeller performance coefficients of interest are the thrust and power coefficients as presented in Equation 2.2 and Equation 2.3. These coefficients are based on the advance ratio and model/flow conditions [20]. In these equations, the thrust and power are denoted by T and P. The parameters in the denominator are the air density (ρ_∞), free stream velocity (V_∞), propeller diameter (D) and propeller rotational speed (n). An important note to these equations is that the free stream velocity could be at a relative angle to the propeller as a result of the angle of attack or sideslip angle. This should be accounted for by determining the axial inflow component.

$$T_C = \frac{T}{\rho_\infty {V_\infty}^2 D^2} = \frac{C_T}{J^2} \quad \text{with,} \quad C_T = \frac{T}{\rho_\infty n^2 D^4} \tag{2.2}$$

$$P_C = \frac{P}{\rho_\infty {V_\infty}^3 D^2} = \frac{C_P}{J^3} \quad \text{with,} \quad C_P = \frac{P}{\rho_\infty n^3 D^5} \tag{2.3}$$

The propulsive efficiency, based on classical momentum theory for a propeller without the presence of slipstream swirl, can be determined with Equation 2.4 [21]. This is referred to as the ideal efficiency when the flow is inviscid, incompressible and irrotational.

$$\eta_p = \frac{T V_\infty}{P} = \frac{C_T J}{C_P} = \left[\frac{1}{2} + \sqrt{\frac{1}{4} + \frac{2C_T}{\pi J^2}} \right]^{-1} \tag{2.4}$$

Neglecting the rotational part of the slipstream, called swirl, is naturally unrealistic, as this component would decrease the propulsive efficiency for any given thrust coefficient. Equation 2.5 presents the propulsive efficiency when a uniform tangential velocity is assumed and no restriction is set on a uniform pressure distribution at each cross-section of the stream tube as derived in [21]. The difference between these two formulas can be seen in Figure 2.12.

It can be observed that the propulsive efficiency is overpredicted when the swirl component is not included. This is especially true at higher thrust coefficients, as is evident from the larger difference for $C_T = 0.65$. The momentum loss due to the propeller torque can be minimised by introducing SRVs in the propeller slipstream. When designed and positioned correctly, these vanes can recover part of the loss in angular momentum and increase the propulsive efficiency.

$$\eta_p = \left[\frac{1}{2} + \sqrt{\frac{1}{4} + \frac{\pi^2}{4J^2}\left(1 - \sqrt{1 - \frac{16C_T}{\pi^3}}\right)}\right]^{-1} - \frac{J^2}{\pi^2}\left[\sqrt{1 + \frac{\pi^2}{J^2}\left(1 - \sqrt{1 - \frac{16C_T}{\pi^3}}\right)} - 1\right] \tag{2.5}$$

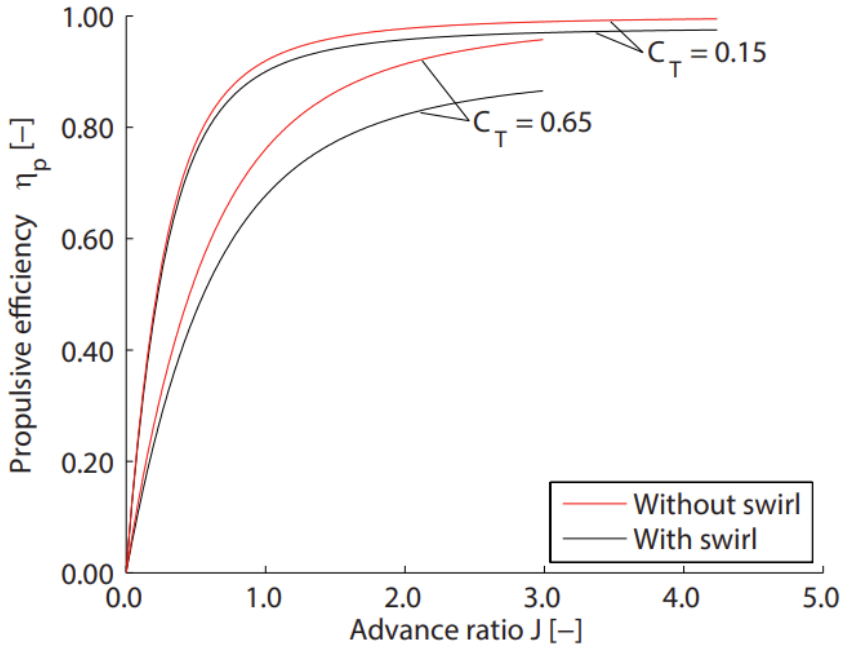

Figure 2.12: *Propulsive efficiency with and without the effects of propeller swirl versus the advance ratio for two thrust coefficients [23]*

The formulas, as presented above, are valid for the propeller but not the entire model. The total model efficiency is, however, the parameter of interest, as this will indicate if the placement of an additional vane is beneficial for the overall model performance. The efficiency formula used in this thesis research, based on Equation 2.4, is presented below in Equation 2.6. The axial thrust of each aerodynamic component will be used to determine the total axial propulsive efficiency, with T_x being the total axial thrust of all components in the reference coordinate system. The individual component contributions as used for the final results will be discussed in Section 3.3. The definition of this coordinate system will be presented in Chapter 3 as well as some additional parameters used for model validation.

$$\eta_x = \frac{T_x \cdot V_\infty}{P} \tag{2.6}$$

3

Methodology

This chapter describes how the research question, stated in the introduction of this thesis work, will be answered. The goal of this thesis research is to determine the optimal vane placement for axial propulsive efficiency. This will be determined based on a predetermined reference model, as will be discussed in Section 3.1. This chapter also discusses the aerodynamic solver used for this research in Section 3.2, after which several performance and analysis parameters are discussed in Section 3.3. The validation and model modifications with additional vanes, to determine the optimal SRV placement, will be addressed in Chapter 4 and Chapter 5, as several design decisions are based on the validation of the reference model. This chapter concludes with a short summary of the discussed topics in Section 3.4.

3.1. Model Geometry

The reference model used for this thesis research is based on the model described by Duivenvoorden et al. [28], which can be seen in Figure 3.1. The pressure and suction side of the model are respectively presented in Figure 3.1a and Figure 3.1b, with annotated components. This model was chosen because of the availability of flow characteristics at several locations in the flow, which would allow for a comparison of the propeller slipstream velocities at those locations. Pressure tab measurements on the wing's surface in the propeller slipstream were also performed during the experiment, providing pressure distribution and sectional lift data, which will later be discussed in Chapter 4. Another reason for choosing this model was the possibility of placing SRVs on the model. The nacelle is relatively long, allowing for the placement of SRVs at different locations, which was an important consideration for a reference model. A drawback of this model is that the experiment was performed at relatively low sub-sonic conditions and blade loading, which have less swirl compared to faster flight conditions with highly loaded blades. This will be considered later in the results.

The complete reference model, based on the shown experimental setup, will be discussed in this section for each of the main components. The wing airfoil profile and geometry will first be discussed in Subsection 3.1.1. The Nacelle and propeller geometry will be discussed in Subsection 3.1.2, which is followed by Subsection 3.1.3, where an overview of the reference model is presented as well as the coordinate systems used in this thesis research.

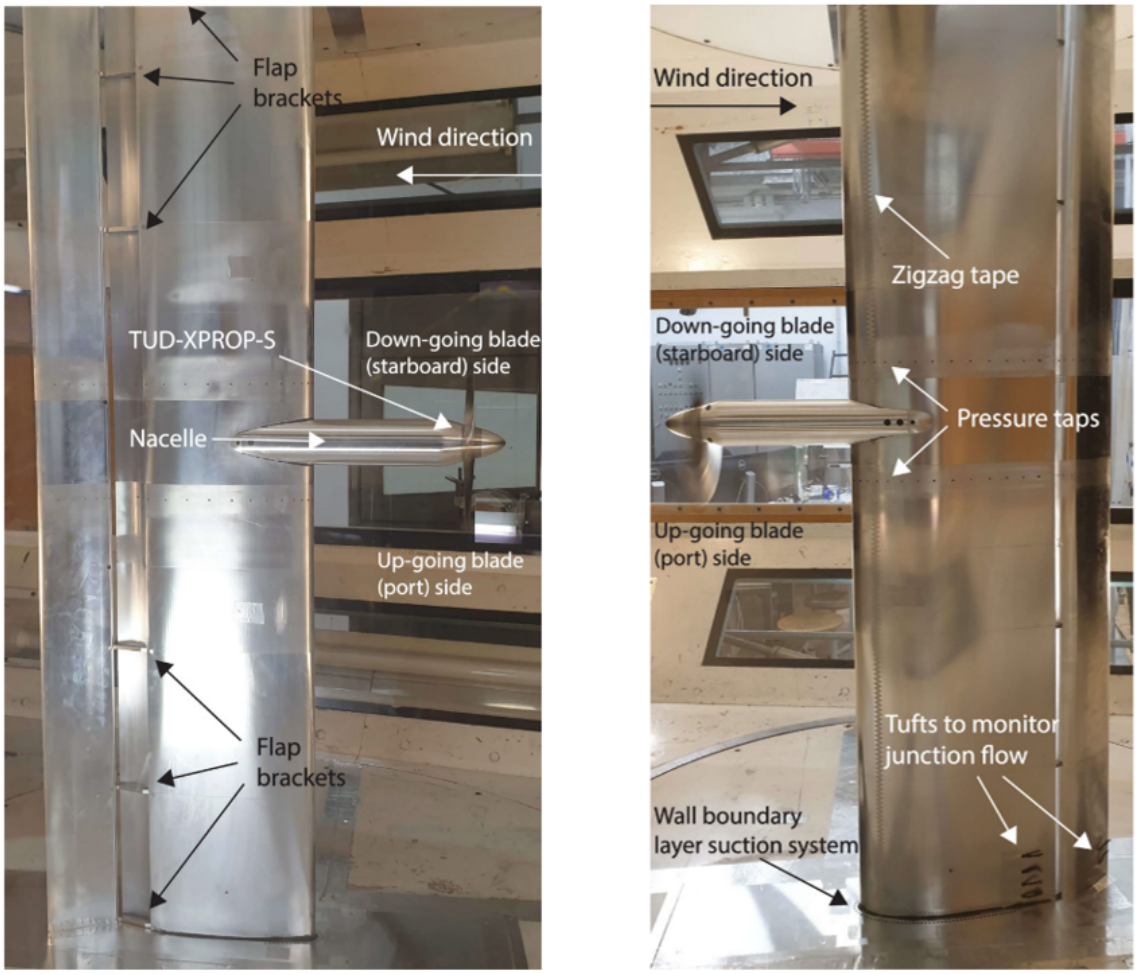

(a) *Pressure side of the experimental wind tunnel setup*

(b) *Suction side of the experimental wind tunnel setup*

Figure 3.1: *Duivenvoorden experimental setup pictures of the wind tunnel model pressure (a) and suction (b) side of the model at an angle of attack of* 0° *[29]*

3.1.1. Wing

The wing airfoil profile is the NLF-mod22(B) profile as initially designed by Boermans and Rutten [30], and consists of a main element as well as a fowler flap. A wing with deployed fowler flap adds, for this thesis, unnecessary complexity, which is why a wing airfoil with retracted flap will be used. The main element and fowler flap were combined into one airfoil profile to reduce model complexity and prevent possible solver divergence. This was done by connecting the elements with a third-order polynomial to ensure smooth surface transitions. The main element, fowler flap and combined NFL-mod22(B) airfoil, as will be used in this thesis, are presented in Figure 3.2 below. The combined airfoil coordinates can also be found in Appendix A.

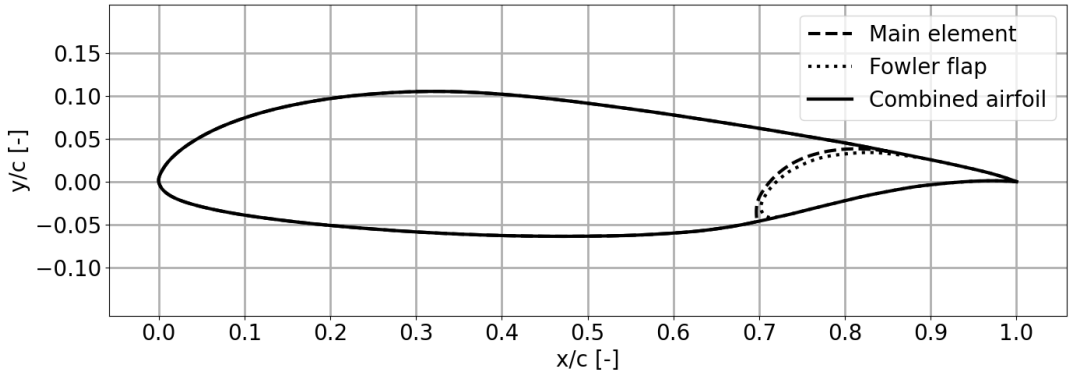

Figure 3.2: *Figure showing the NLF-mod22(B) main and flap element as defined by Boermans and Rutten [30] and combined airfoil element used in this thesis research*

During the experiment, the wing was clamped between the wind tunnel walls, spanning a distance of 1.25 m. This means that the wind tunnel data, regarding the wing pressure distribution, is essentially two-dimensional. "In contrast, a finite wing is a three-dimensional body, and consequently, the flow over the finite wing is three-dimensional; that is, there is a component of flow in the spanwise direction."[31] There is an imbalance of pressure between the lower pressure on the upper surface of the wing and the higher pressure on the lower surface. This causes the flow to curl around the wing tip from the lower to the upper surface of the wing, resulting in a circular motion in the flow that trails downstream, which is called a wing-tip vortex. [21]

It was initially considered to model the wind tunnel section in the aerodynamic solver. This idea was later determined not to be appropriate because of the additional required computational time for modelling the wind tunnel. The added model complexity was also deemed not suitable for the goal of performing a low-mid fidelity analysis. The difference in 2D and 3D aerodynamics would be accounted for by modifying the wing span such that the local lift coefficient at the experimental pressure tab measurements, located at ±0.7 y/R, would be equal. It was determined with XFOIL[1] that the 2D lift coefficient of the NLF-mod22(B) airfoil is equal to 0.3667. XFOIL is a 2D “inviscid linear-vorticity panel method” analysis tool, which is especially suited for flows at low Reynolds numbers [32]. The spanwise lift coefficient distributions of several wings with different wing spans were evaluated with the aerodynamic solver used for this thesis research for an isolated wing, which will be described in Section 3.2. These distributions were determined with steady aerodynamic analysis performed with the aerodynamic solver for this research, which will be discussed in more detail in Section 3.2. The results of this spanwise lift distribution test are presented in Figure 3.3. In this figure, the 2D lift coefficient is represented by a horizontal red dashed line, and black lines represent the spanwise lift coefficients for the tested wing spans. The spanwise locations of the pressure tab locations are also indicated in the figure by blue vertical lines.

It can be seen that the spanwise lift distribution of the wing with a wing span of 1.25 m, as used in the experiment, does not reach the 2D lift coefficient. The reason for this are 3D wing tip effects, which reduce the spanwise lift coefficients near the tip. The influence of these wing tip vortices affects more of the centre of the wing due to the relatively small wing

[1]XFOIL Subsonic Airfoil Development System by M. Drela, H. Youngren, version 6.99 (2000).

span and low aspect ratio. The wing with a wingspan of 1.75 m best matches the local lift coefficient at the pressure tab locations. It is for this reason that this wing was chosen for further modelling of the wing.

The final wing geometry for this thesis research, presented in Figure 3.4, is thus slightly modified compared to the wing used in the wind tunnel experiment. These changes were made to simplify the analysis and account for the difference in 2D and 3D flow conditions. An overview of the geometric wing parameters is presented in Table 3.1.

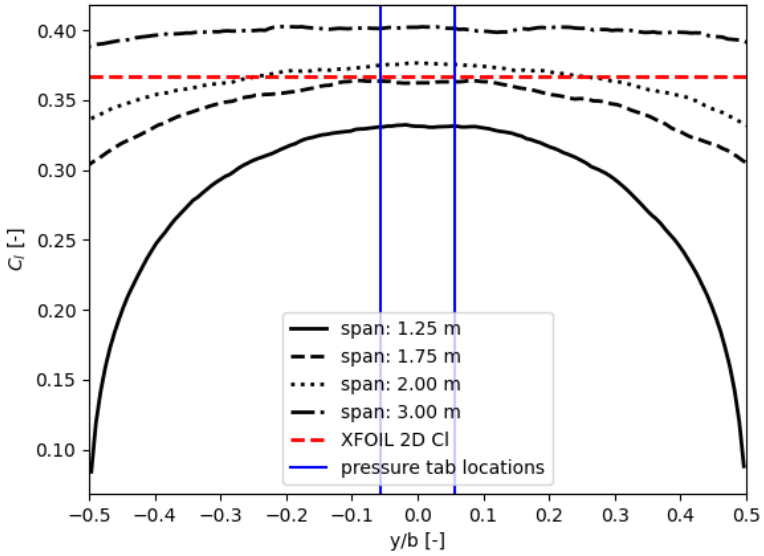

Figure 3.3: *Figure showing the 2D lift coefficient as determined with XFOIL (red dashed line), compared to the spanwise lift distribution as determined by the aerodynamic solver with steady analysis for different wing spans (black lines) and indicated location of spanwise location of pressure tab data (blue vertical lines) for a wing at* 0° *angle of attack and a constant* 0.3 m *chord*

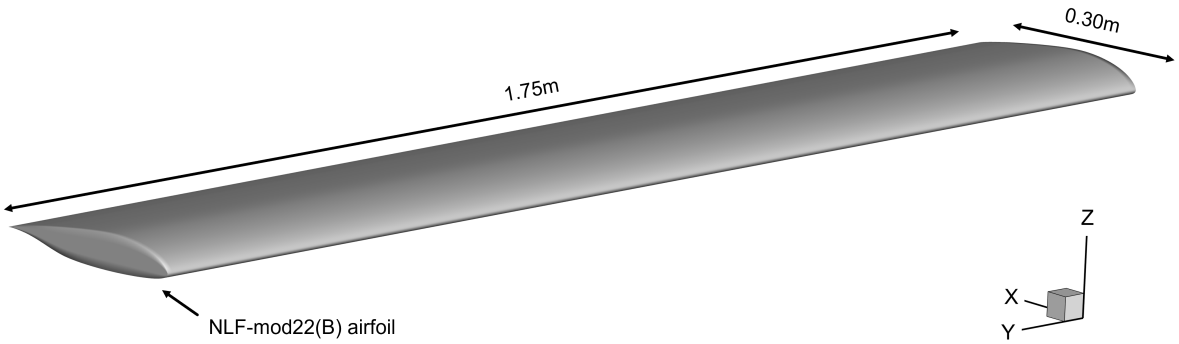

Figure 3.4: *3D representation of the combined wing geometry at* 0°*, with annotated airfoil profile and dimensions*

Table 3.1: *Geometric parameters of the combined NLF-mod22(B) wing as used in this thesis research*

Parameter	Symbol	Value	Unit
Wing span	b_w	1.75	m
Wing chord	c	0.3	m
Taper ratio	λ	1.0	-
Surface area	S	0.525	m^2
Aspect ratio	AR	5.83	-

3.1.2. Propeller and Nacelle

The propeller, used by Duivenvoorden during the experiment, is the TUD-XPROP-S propeller as described by van Arnhem [33]. This is a six-bladed propeller with a diameter of 0.2032 m and a blade pitch of 30° at 0.70 r/R. Figure 3.5 shows the local pitch and chord distribution of the propeller blades in Figure 3.5a and several airfoil profile sections in spanwise direction in Figure 3.5b, for which the data can be found in [33]. The propeller geometry is presented in Figure 3.6, where a front-view and zoomed-in section of the propeller blade and spinner are presented in Figure 3.6a and Figure 3.6b. It can be seen that there is a small gap present between the propeller blade and nacelle, which will be justified in Subsection 3.1.3, where the component integration is discussed. The combined propeller and nacelle geometry is lastly presented in Figure 3.7. In this figure, the TUD-XPROP-S propeller and slender nacelle are shown with an area marked of the nacelle, where the wing and nacelle intersect.

The relatively long cylindrical nacelle connects the wing, spinner and propeller to the centre of the wing. The nacelle has a diameter of 0.056 m and is mounted with a relative angle to the wing of –5°. The TUD-XPROP-S propeller is placed at approximately 0.85 D from the leading edge of the wing, where nacelle diameter is ≈0.044 m [28]. The next subsection will show an overview of the entire model, where the shape and positioning of the propeller are presented more clearly.

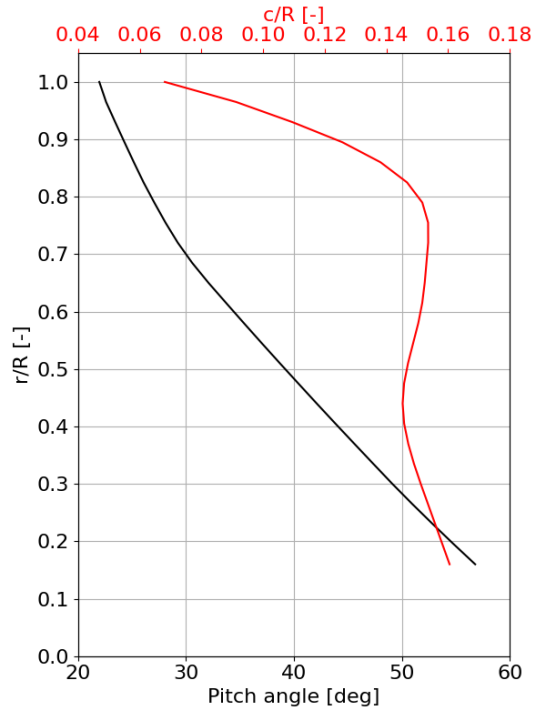

(a) *Local chord and pitch angle distribution for a TUD-XPROP-S propeller blade*

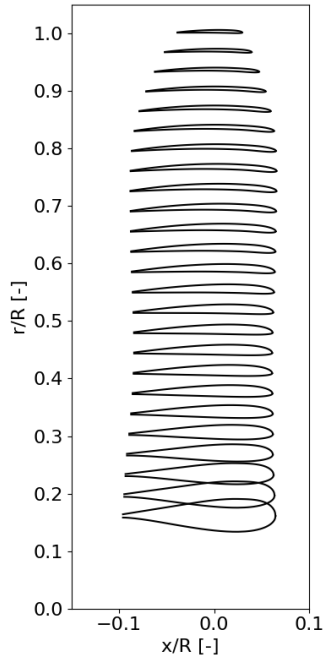

(b) *Blade airfoil sections of a TUD-XPROP-S propeller blade*

Figure 3.5: *Blade geometry for TUD-XPROP-S ($\beta_{0.7R} = 30°$) propeller based on van Arnhem et al. [33], with the local chord and pitch angle distribution (a) and spanwise blade airfoil sections (b)*

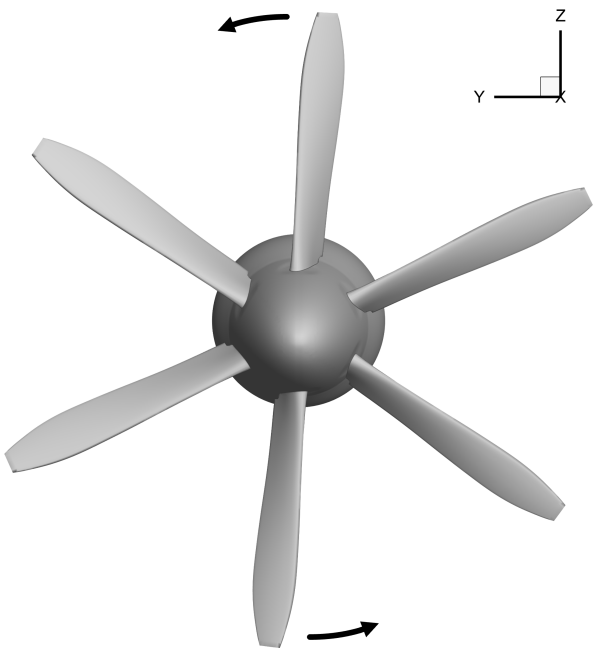

(a) *TUD-XPROP-S propeller and nacelle front-view*

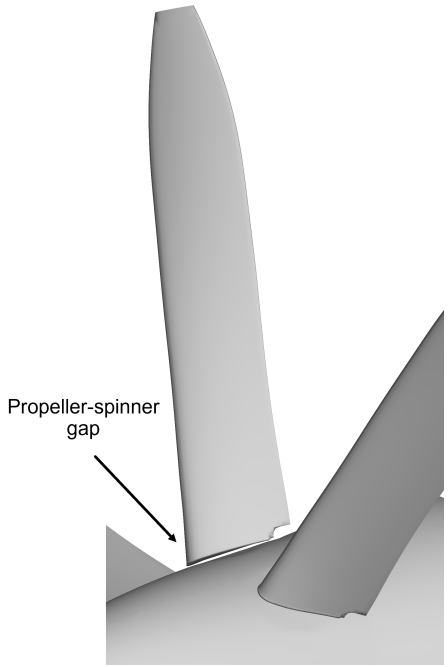

(b) *Propeller blade and nacelle gap*

Figure 3.6: *TUD-XPROP-S propeller figures showing the propeller and nacelle front-view (a) and propeller blade-nacelle gap (b)*

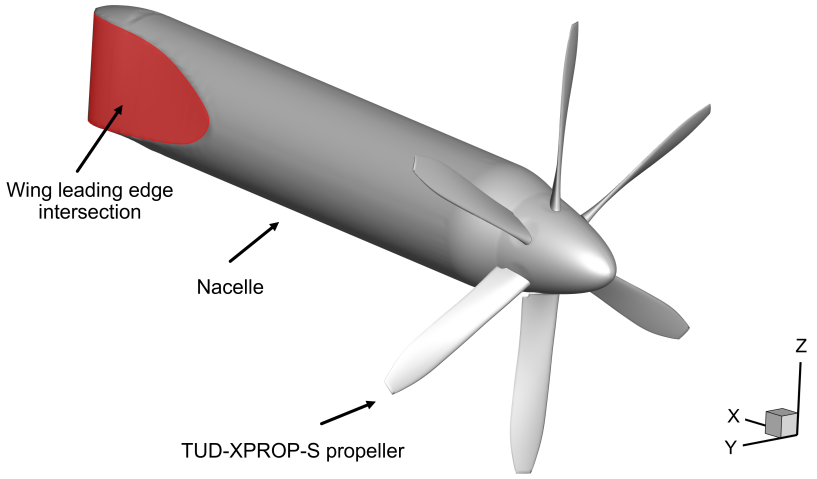

Figure 3.7: *TUD-XPROP-S propeller and nacelle figure with indicated wing leading edge intersection location*

3.1.3. Reference Model Overview

The geometries as described in Subsection 3.1.1 and Subsection 3.1.2 are combined to create the reference model for the aerodynamic analysis of this thesis research. The wing geometry, as discussed earlier, was modified compared to the wing used in the experiment. The change in wing span was performed with the Open Vehicle Sketchpad (OpenVSP) software. This is an open-source parametric geometry program developed by NASA, which allows the user to generate three-dimensional models of aircraft [34]. This was made especially easy with the built-in basic aerodynamic components. The generated wing geometry could be exported and later used in the analysis tool.

The geometries of the propeller, spinner and nacelle were available in the form of .STL files. This made the generation of the reference model more accurate and also simplified the process of implementation. These files required some modifications as the geometries would later need to be combined to ensure solver convergence. The chosen aerodynamic solver for this thesis research will be discussed in Section 3.2, but will already affect the choices made on how the reference model is constructed. Beyne [35] observed in his thesis, for example, that model instabilities were observed when modelling the propeller and spinner as separate geometries. The close proximity of a separate spinner and nacelle caused solver instability issues with a rotating spinner and attached propeller blades. Beyne solved this issue by modelling the spinner and nacelle as one geometry and adding separate propeller blades that slide over the spinner surface. A small gap is present between the spinner and propeller blades to prevent mesh elements from overlapping, which would cause solver divergence. This gap was previously presented in Figure 3.6b and measures 0.001 m. The presence of this gap will have an effect on the final results, which will be considered in the respective chapter.

An overview of the reference model can be seen in Figure 3.8, where the dimensions are given in millimetres. The reference coordinate system as presented in this figure is consistent throughout this entire report and is defined as a right-handed system with the positive x-direction aligned with the free stream velocity. Figure 3.10 shows a schematic figure of the

reference model, in side-view and top-view, with the local coordinate systems. The propeller and reference coordinate systems are denoted by the subscripts p and R. The nacelle and wing coordinate systems are respectively equal to the propeller and the wings coordinate system.

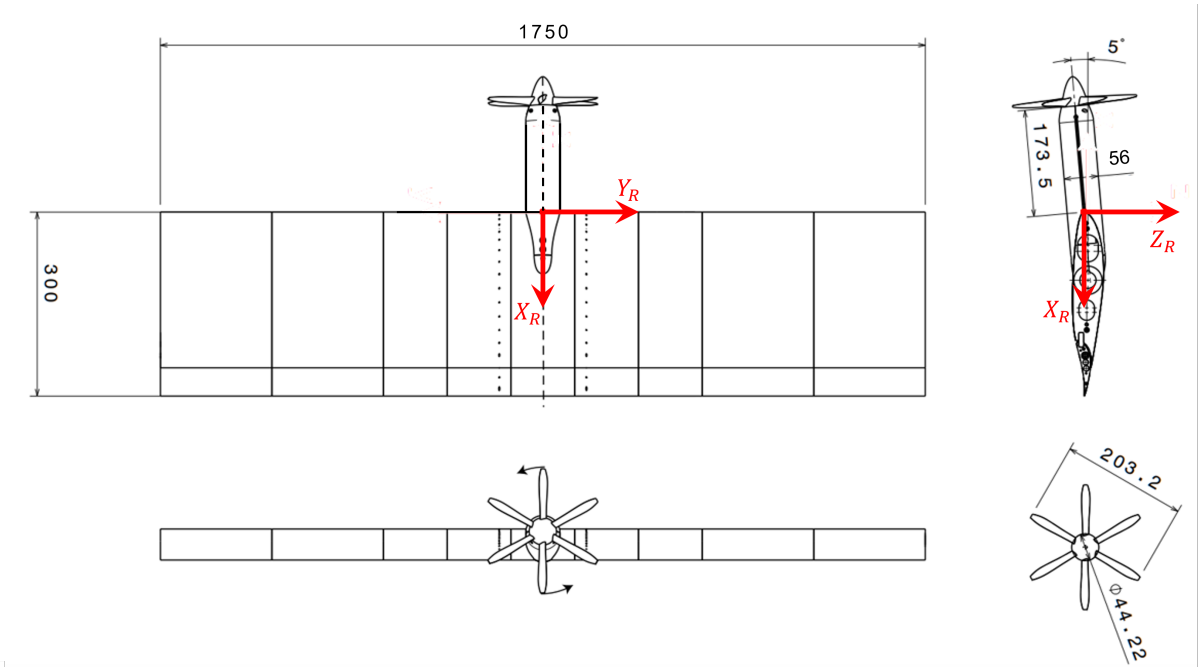

Figure 3.8: *Technical drawing of the reference model with dimensions given in* mm *and reference coordinate system presented in top-, side- and front-view (changed from [28])*

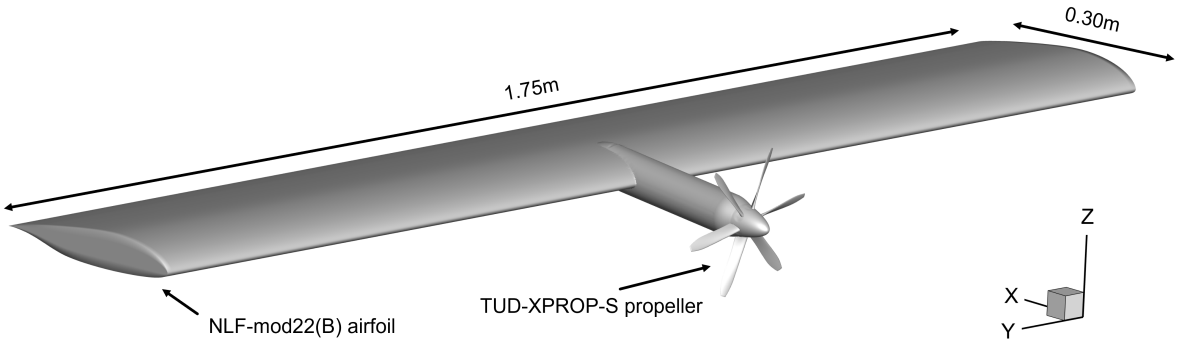

Figure 3.9: *3D reference model overview based on the aerodynamic components, with annotated geometries and dimensions*

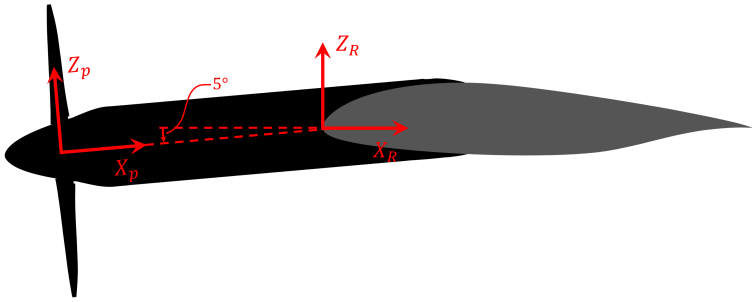

(a) *Local coordinate definitions for the propeller and reference systems in side-view*

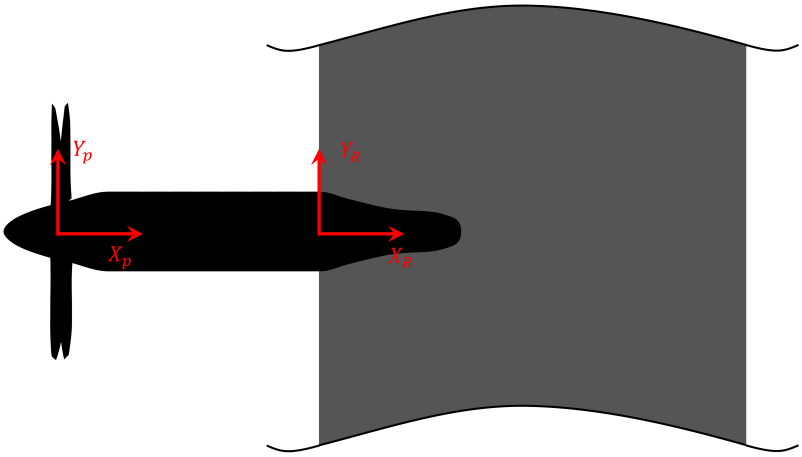

(b) *Local coordinate definitions for the propeller and reference systems in top-view*

Figure 3.10: *Reference model and propeller coordinate systems for aerodynamic surfaces in side-view (a) and top-view (b)*

3.2. Aerodynamic solver

The aerodynamic solver used to conduct this thesis research will be discussed in this section. First, several analysis methods and considerations for determining the solver/analysis tool are described in Subsection 3.2.1. A description of the chosen analysis tool will be discussed in Subsection 3.2.2, after which the solver settings are then discussed in Subsection 3.2.3.

3.2.1. Analysis Method and Justification

The aerodynamic analysis for this research can be performed with several different methods. The main methods are: Reynolds Average Navier Stokes (RANS) Computational Fluid Dynamics (CFD) analysis, writing an aerodynamic analysis tool from scratch or using third-party software. This thesis aims to determine the aerodynamic accuracy of a lower-order aerodynamic analysis tool as stated in the research sub-questions in Section 1.1. The option of a full RANS-CFD analysis is thus not suitable for this research. Creating an aerodynamic solver from scratch was deemed unrealistic for this thesis, as there are many complex flow interactions and corrections required to produce accurate results. Creating and validating a new model would most likely take much longer than the duration of this thesis.

Research papers looking into SRV effectiveness have used self-made lower-order analysis methods such as the Lifting Line Technology (LLT) and Vortex Lattice Method (VLM). Stokkermans [23] used a lifting line method in his thesis to gain insight into the aerodynamic interactions between a propeller slipstream and SRVs. The lifting line theorem by Prandtl states that a wing can be represented by bound horseshoe vortices at the quarter chord of the wing [36]. The lifting line model as used in Stokkermans' thesis is based on the model by Phillips and Snyder [37] but was modified to account for non-uniform inflow.

Ferraro et al. [38] utilised VLM to predict the propeller-wing interaction for early design. In this work, the propeller wake inflow originates from a separate RANS CFD analysis performed with an isolated propeller. These inflow conditions were then used for an initial estimation of the wing lift distribution, and with an iterative process of VLM and 2D-aerodynamic database, converged to a final solution. The VLM method places chordwise lifting lines in addition to the spanwise vortices of the Prandtl lifting theorem to create panels [31]. This allows for the wing sweep to be better captured, as often seen in higher aspect ratio wings.

Both the LLT and VLM are great lower-order aerodynamic methods, but each suits slightly different cases. Sarıgöl [39] discussed the differences between these two methods. It was determined that there were two main differences between LLT and VLM. The first one is that VLM can take into account wing sweep, whereas LLT is only well-suited for wings with higher aspect ratios. Another difference is that a VLM model enforces flow tangency at all points and that the Kutta condition is adhered to, meaning that there is no backflow over the trailing edge of the wing and that the airflow leaves the profile smoothly [31]. It was concluded that the results of a VLM calculation were nearly always favourable, as the accuracy was higher. There is, however, one drawback, as the computational cost is significantly higher for VLM. This is because this method is more complex compared to an LLT approach.

A more advanced analysis method is the panel method. This method allows for the 3D representation of lifting and non-lifting surfaces. Such an approach is computationally more expensive and more difficult to create. There are, fortunately, several open-source and commercial aerodynamic analysis software packages available based on the implementation of set panel methods. There were initially two main aerodynamic analysis tools described within previous research papers on propeller, wing and SRV interactions. These analysis programs were VSPAERO and Flightstream. VSPAERO is an analysis tool in the open-source program OpenVSP developed by NASA, and Flightstream is a commercial software package developed by Altair. Several papers have described either of the two or performed a comparison between the programs, which will be discussed below.

E. Mariën looked in his thesis [34] at how the analysis tool in OpenVSP called VSPAERO performed. OpenVSP allowes for quick and easy model generation with the geometric browser and built-in basic components. There are several analysis tools available in OpenVSP, of which the aerodynamic solver VSPAERO is of interest for this thesis research. VSPAERO was added in 2015 and allows for aerodynamic modelling with either a VLM or panel method. It was found that the OpenVSP panel method was better suited for flow visualisation, but that the solver, in general, had some difficulties with more complex geometries.

P. Zinjarde used OpenVSP in his thesis about strut-braced wings [40]. The VSPAERO analysis results were compared to wind tunnel data, RANS CFD results and the second aerodynamic tool, Flightstream. It was found that the results from VSPAERO, regarding the lift and drag

polars, as well as the lift distribution, were worse compared to Flightstream. It was decided in his work that VSPAERO would not be considered for the aerodynamic analysis of the strut-braced wing. OpenVSP was, however, still a useful tool as it allowed for easy geometric alterations to be made and visualised. This proved to be especially useful as it was possible to create a script in Python/MATLAB or C++ to change the geometry and then export a mesh to Flightstream.

E. Beyne describes in his thesis [35], similarly to P. Zinjarde, how Flightstream was used to analyse a strut-braced wing. Flightstream was compared to an unsteady RANS CFD analysis, which proved to be accurate for the desired analysis of the propeller, wing and strut aerodynamics. The same was found by V. Ahuja [41], who concluded that Flightstream is a useful tool for the initial design phase. This was mainly because of the significantly lower computational cost compared to a RANS CFD analysis. It was, however, observed that the accuracy of Flightstream decreased with higher angles of attack. This was attributed to the fact that Flightstream could not accurately model flow separation. X. Fei [42] concluded the same about the accuracy of Flightstream. This study noted that the mesh refinement had the largest effect on the accuracy. N.J. Blaesser [43] performed research regarding distributed propellers using Flightstream. The model and analysis tool were validated with experimental data, which was matched accurately.

It was decided that Flightstream would be a more accurate analysis software compared to OpenVSP, based on the papers just discussed. This is thus the analysis software of choice for this thesis. A brief introduction on Flightstream and aerodynamic analysis method is follows in Subsection 3.2.2 below.

3.2.2. Flightstream Solver

Flightstream is a surface vorticity potential flow solver, developed by Altair. This analysis software allows for the development of compressible and incompressible sub- and transonic vehicles at a fraction of the computational cost of a full RANS CFD analysis. The computational time would go from taking hours to minutes[2]. The built-in robust meshing algorithm and Computer-Aided Design (CAD) compatible scripting interface allow for rapid analysis and optimisation [42].

Flightstream solves the vorticity around a geometry by dividing the geometry into surface panels of bound vorticity. The vorticity is shed into the wake via the trailing edge, creating circulation and thereby lift. The aerodynamic loads are then determined based on the surface vorticity and induced velocities.

Figure 3.11 shows a flowchart of the general approach used by the Flightstream solver. The first step is to create the geometry, which can be done by importing several types of supported geometry files. A surface mesh is then created from this geometry, on which boundary conditions are imposed. The definition of trailing edges, wake termination nodes, and base regions, are examples of such boundary conditions that can also be found in the Flightstream theory manual[3]. The flight conditions and solver settings should then be set to start the analysis, which will be discussed in the next sub-section. First, a viscous run is performed, after which an inviscid run follows. This inviscid run is only iterated until con-

[2]https://www.darcorp.com/flightstream-aerodynamics-software
[3]https://flightstream-theory.netlify.app/

vergence if the viscous coupling setting is turned on. The induced velocities and surface pressures are finally used to compute the aerodynamic loads, which are shown in the solver environment.

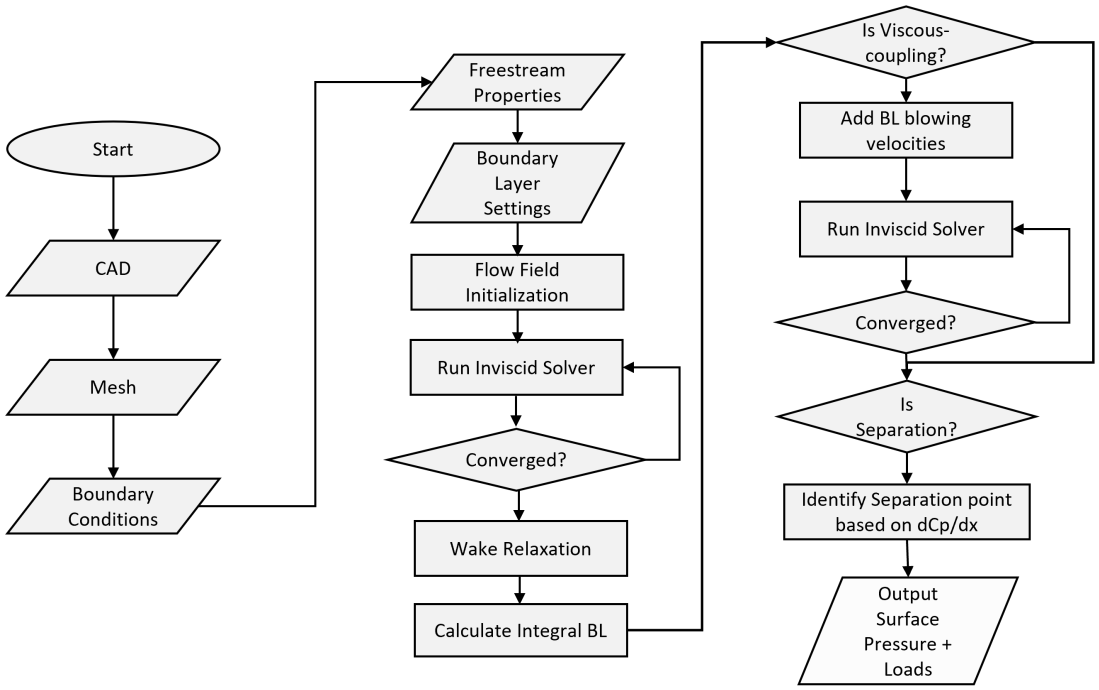

Figure 3.11: *Flightstream flowchart showing the general aerodynamic analysis steps*

3.2.3. Flightstream Settings

There are several options for setting up the solver in Flightstream. These settings relate to the Flightstream analysis settings, solver settings and operational conditions. The following paragraphs will discuss each of these aspects and explain why certain settings have been chosen.

Analysis Settings

The first setting to consider is the type of analysis that is to be performed. Flightstream is able to perform steady as well as unsteady analyses. This research concerns the modelling of a rotating propeller, meaning that the unsteady modelling in small time steps is more appropriate. A steady analysis would be possible to model in Flightstream by using an actuator disc model with constant propeller swirl, but this is not suitable for this thesis research, where the propeller swirl should not be assumed constant.

The main analysis settings used for this thesis research are presented in Table 3.2. The Surface Proximity Avoidance (SPA) setting was determined to be one of the most influential settings for the final results. This setting allows the user to choose if the wake elements in front of the aerodynamic surfaces should be propagated through the model (setting OFF) or if the vortex elements intersecting other surfaces should be removed (setting ON). Both options would not be entirely realistic, which is why both settings have been used for the aerodynamic analyses, as will later be discussed during the validation of the analysis tool in Chapter 4.

The decision to disable the viscous coupling was based on the findings of E. Beyne [35]. He concluded that turning on the viscous coupling had no significant effect on the results of a strut-braced wing interaction and that the extra computational time was thus not worth it. An added strut is essentially the same as adding a vane or small wing, which is why it is assumed that the influence of this setting for this thesis would be similar.

The unsteady timestep of 0.0002 s was based on the best practice timestep for propeller modelling as stated in the Flightstream user manual[4], where the propeller rotation should be between 10 and 15° per timestep. This timestep, combined with the propeller rotational speed of 1159.55 rad/s, would mean a propeller rotation of ≈13.3° per timestep. The rotational speed is based on the advance ratio of the propeller, which will be defined in the operational condition settings that will follow. The number of timesteps required for one complete propeller rotation was determined to be 28. 80 timesteps would be performed before saving data to ensure solver convergence. The propeller wake would be approximately 2.0 c behind the trailing edge of the model after these initial 80 timesteps.

The wake distance and boundary layer type would be left at the default settings of respectively 2.050 m and transitional turbulent. The wake distance location by default is set to the last mesh face location plus the length of the geometry along the direction of the flow. This distance represents the clipping location of the wake to improve the computational time.

Table 3.2: *Flightstream analysis settings used for the aerodynamic analysis during this thesis research*

Setting	**Value**	**Unit**
Surface proximity avoidance	ON/OFF	–
Viscous coupling	Disabled	–
Unsteady timestep	0.0002	s
Number of timesteps	80 + 28	–
Wake distance	2.050	m
Boundary layer model	Transitional turbulent	–

Solver Settings

The solver settings are the second type of settings that the user can specify in Flightstream. These settings specify general aspects of the solver and are presented in Table 3.3. The reference velocity is specified here, which is used to determine the force and moment coefficients. The remaining solver settings were left at their default settings as presented in the table. The parallel processors parameter is important to note, as a typical laptop or computer does not have this many cores. This thesis research was performed on a dedicated server with a remote desktop connection to run the simulations more efficiently.

[4]https://flightstream-theory.netlify.app/

Table 3.3: *Flightstream solver settings used for the aerodynamic analysis during this thesis research*

Setting	Value	Unit
Reference velocity	30.00	m/s
Number of iterations	500	–
Convergence threshold	$1E-05$	–
Parallel processors	48	–

Operational Conditions

The last, and arguably most important, aspect of the setup is defining the operational conditions. The operational conditions are presented in Table 3.4, which are based on the flow conditions used during the experiment and include medium and attitude parameters. The angle of attack and sideslip angle define the model orientation with respect to the free stream velocity, and the last three parameters define the propeller operating conditions. The propeller rotation in rad/s follows from the advance ratio formula as previously stated in Equation 2.1 and the propeller geometry as discussed in Section 3.1.

Table 3.4: *Flightstream operating conditions used for the aerodynamic analyses during this thesis*

Parameter	Symbol	Value	Unit
Free stream velocity	V_∞	30.0	m/s
Mach number	M	0.08816	–
Static pressure	$P_{s,\infty}$	101324.02	Pa
Temperature	T_{temp}	288.17	K
Air density	ρ_∞	1.225	kg/m^3
Angle of attack	α	0.000	deg
Side-slip angle	β_{side}	0.000	deg
Advance ratio	J	0.8	–
Propeller rotation	n	184.55	RPS
Blade pitch	$\beta_{0.7R}$	30	deg

3.3. Aerodynamic and Performance Analysis

The output of the analysis tool consists of positional and velocity data for each of the analysis planes defined, as well as total model forces and moments. The locations of these analysis planes have not been presented yet, but will be discussed in the next chapters. The data from these analysis planes will be averaged for the 28 timesteps required for one propeller rotation, as a single timestep is not representative of the overall performance. This section describes what aerodynamic and performance parameters are used in this research based on the Flightstream output data.

Aerodynamic quantities such as the angle of attack, total pressure and total velocities at each point on the analysis planes are obtained by correcting the output velocity data based on the relative orientation to the model. This data is then used to plot 2D aerodynamic data on the analysis planes. Duivenvoorden et al. [18] introduced a parameter called the total pressure ratio, which will be used to validate the output of Flightstream in the next chapter. The total pressure ratio shows the increase in total pressure in the propeller slipstream. The formula

used to determine this ratio can be seen in Equation 3.1, where P_T is the total pressure, $p_{s,\infty}$ is the static pressure and q_∞ the dynamic pressure of the flow [28].

$$Cp_T = \frac{P_T - P_{s,\infty}}{q_\infty} \tag{3.1}$$

Another important aerodynamic quantity for this thesis research is the Force factor (Ff), which will be introduced in this research. The force factor will indicate where the most thrust generation potential can be found in the propeller slipstream by redefining the sectional lift formula. The formula for sectional lift in Equation 3.2 is first generalised by replacing the C_l term with the linear relation approximation $2\pi\alpha$. The dynamic pressure is non-dimensionalised by dividing by the inflow dynamic pressure. The reference chord length c_{ref}, for the purposes of this research, is dropped as it acts as an unnecessary scalar because of the constant SRV chord, which will be discussed in Chapter 5. The vane thrust potential can be determined by multiplying by the sine of the local angle of attack. The resultant formula for Ff can be seen in Equation 3.3. It should be noted that this force factor is related to the local flow conditions seen by the SRV, meaning that vanes not placed in the reference frame of the wing require an additional correction factor based on the angle relative to the wing's coordinate system.

$$L' = C_l \cdot \frac{1}{2}\rho V^2 c' = C_l q c_{ref} \tag{3.2}$$

$$Ff = 2\pi\alpha \cdot \frac{q}{q_\infty} \cdot sin(\alpha) \tag{3.3}$$

The objective of this thesis research is to determine the optimal SRV position for overall efficiency. The formula for the total axial propulsive efficiency as introduced in Section 2.5 is once again presented in Equation 3.4 below, with the T_x sub-components defined. The individual thrust components are taken in the reference coordinate system's axial direction. Flightstream calculates the forces of each model element, allowing this efficiency in the axial direction to be calculated per element as well as the total axial efficiency. The propeller power in the numerator of the equation is, in all cases, determined in the propeller reference frame.

$$\eta_{x,tot} = \frac{(T_{x,p} + T_{x,n} + T_{x,w} + T_{x,v}) \cdot V_\infty}{P} \tag{3.4}$$

3.4. Methodology Conclusions

This chapter describes the model used for this thesis research and defines the analysis tool that will be used to perform this thesis research. The most important settings for this tool have been discussed, allowing others to replicate this research. Additional analysis parameters have lastly been introduced and described in this chapter, which will later be used to validate the analysis tool and analyse the results.

4

Validation

This chapter describes the validation of the reference model by comparing the experimental data obtained by Duivenvoorden et al. [44] with Flightstream results under the same conditions specified in Chapter 3. The surface proximity avoidance setting was the most influential, as previously mentioned. It is for this reason that the following validation sections will include both SPA settings. Section 4.1 starts with describing the surface proximity avoidance setting in more detail, and the impact on the Flightstream simulations. Section 4.2 compares the velocity ratios at three different analysis planes as sampled during the experiment. The locations of these planes can be seen in Figure 4.1, which were implemented at the same locations during the Flightstream analysis. The specific axial analysis plane positions are presented in Table 4.1, which all have a width and height of twice the propeller diameter. Section 4.3 continues by discussing the total pressure ratio for the same planes and is followed by Section 4.4, where the experimental and Flightstream propeller thrust is compared. The pressure tab data and spanwise lift coefficient will be discussed in Section 4.5, after which a short chapter conclusion is presented in Section 4.6.

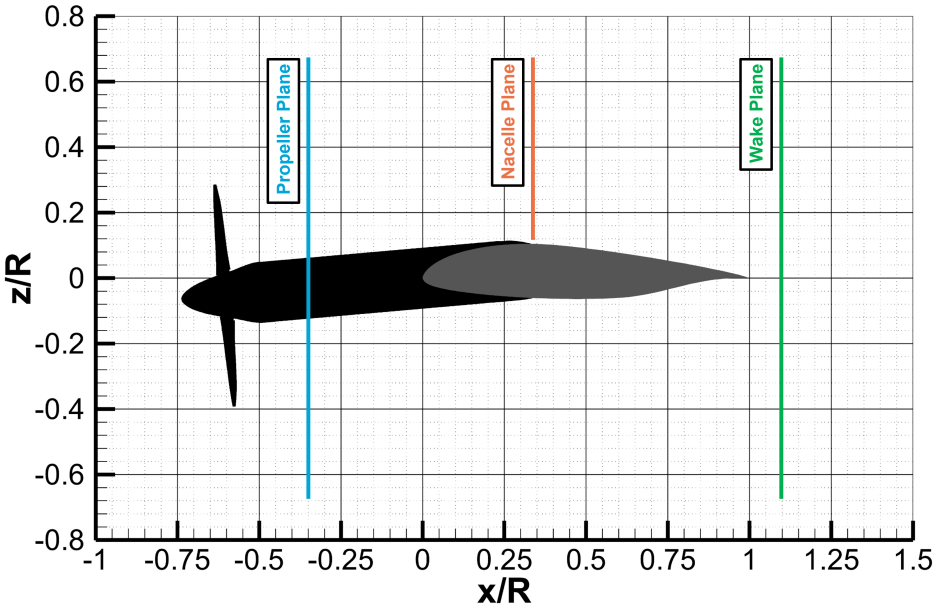

Figure 4.1: *Overview of the analysis plane locations on the reference model geometry as used by Duivenvoorden et al. and Flightstream analysis to validate the results of the aerodynamic solver*

Table 4.1: *Axial locations of the analysis planes on the reference model geometry presented in absolute and relative distances to the leading edge of the wing used for solver validation*

Analysis plane	x [-]	x/c [-]	x/R [-]
Propeller	-0.105	-0.350	-1.033
Nacelle	0.128	0.427	1.26
Wake	0.330	1.100	3.248

4.1. Surface Proximity Avoidance

The surface proximity avoidance (SPA) setting, as previously introduced in Subsection 3.2.3, has a significant impact on the final results. This setting can be turned ON or OFF as stated in the Flightstream manual[1]. The wake elements, which are being shed from the aerodynamic surfaces, are removed if a vortex element crosses another geometry if this setting is turned ON. This prevents the model from overpredicting the induced velocities at the model surface but increases the computational time. The vortex elements are not removed and propagated through the entire model if this setting is turned OFF, which causes the induced velocity at the geometric surfaces to be higher compared to when the setting is ON. The latter is often used for unsteady analysis as it requires less computational time and generally shows a cleaner wake.

The difference between the two settings can be seen in Figure 4.2 below. Figure 4.2a shows the wake with the surface proximity setting ON, where the wake is removed when it is in close proximity to the model geometry. These removed wake elements are not regenerated or continued if the distance between the model and the wake element increases, resulting in the differences, as will be discussed in this chapter. The complete wake, without wake removal, can be seen in Figure 4.2b, which is the case when the setting is turned OFF.

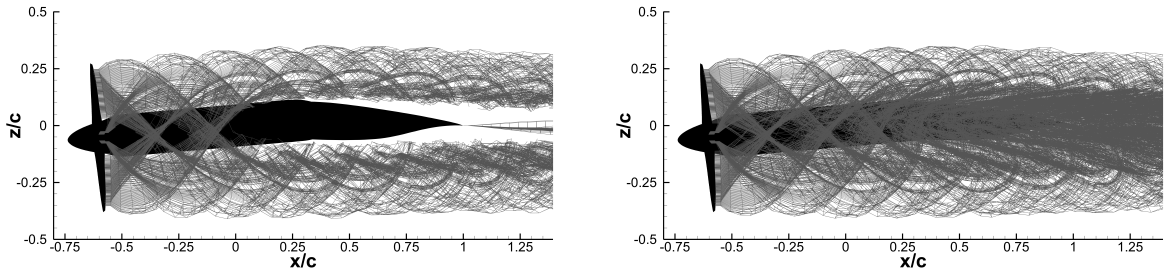

(a) *Helical vortex visualisation over the reference model geometry with surface proximity avoidance setting ON*

(b) *Helical vortex visualisation over the reference model geometry with surface proximity avoidance setting OFF*

Figure 4.2: *Flightstream propeller wake modelling for the surface proximity avoidance setting ON (a) and OFF (b) presented on the reference model geometry from a side-view perspective*

A schematic representation of the SPA setting being turned ON can be seen in Figure 4.3. The vortex elements in this figure originate from the tip of the propeller blade and create a helical vortex, advancing over the model. The SPA setting ON analysis will remove vortex elements if a certain element intersects with the defined model geometry. This can be seen at the indicated location in the figure, where the helical vortex reaches the leading edge of

[1] https://flightstream-theory.netlify.app

the wing. The intersected elements are permanently deleted and marked red in the figure. This causes the empty wake region in the side-view of the SPA setting ON as presented in Figure 4.2a.

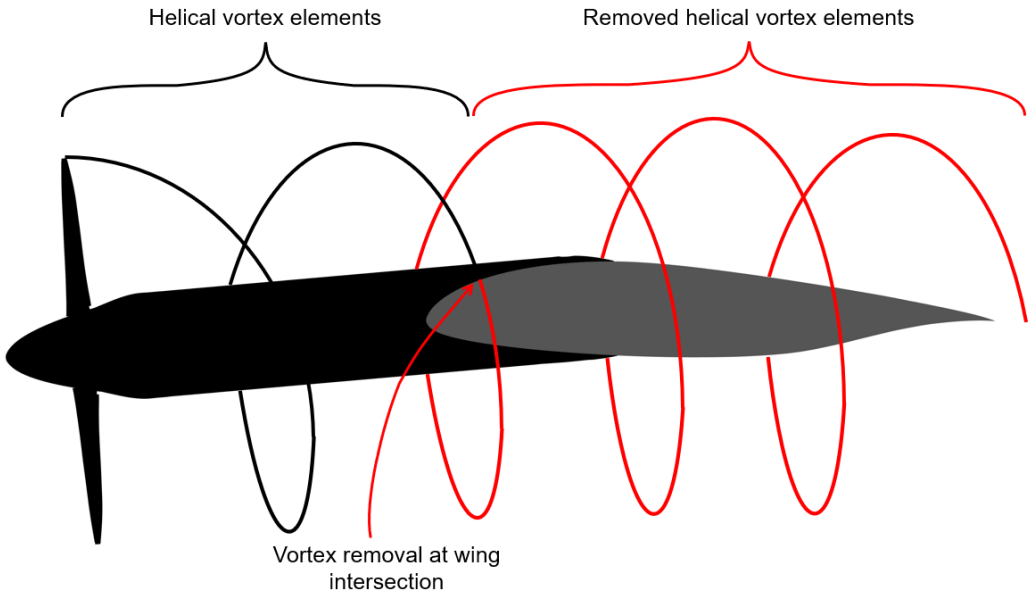

Figure 4.3: *Schematic illustration of the Surface Proximity Avoidance setting with a black helical vortex from the propeller blade tip, point of intersection annotated, and the removed vortex elements marked red*

The SPA setting effects on the pressure distribution can be seen in Figure 4.4. A top- and bottom-view are respectively shown in Figure 4.4a and Figure 4.4b, where a positive value indicates that the surface pressure coefficient for the SPA setting ON is higher. The surface pressure is related to the surface velocity, as an increased surface velocity results in a lower pressure. The figures clearly show that the surface pressures for the SPA setting OFF are lower compared to when the SPA setting is turned ON. This is expected when removing wake elements close to the geometric surface, which are velocity-inducing. The slightly positive regions, as seen in the figure, result from the vortex elements' circulation, inducing a velocity opposite to the free stream velocity and thus a slightly less negative pressure coefficient.

The large differences in the pressure plots in Figure 4.4 indicate that the SPA setting chosen for the analysis will significantly affect the forces. Differences up to a delta C_p of 1.0 can be seen on both the upper and lower surface of the wing in the slipstream, suggesting that the SPA setting does not work well in the slipstream of the propeller.

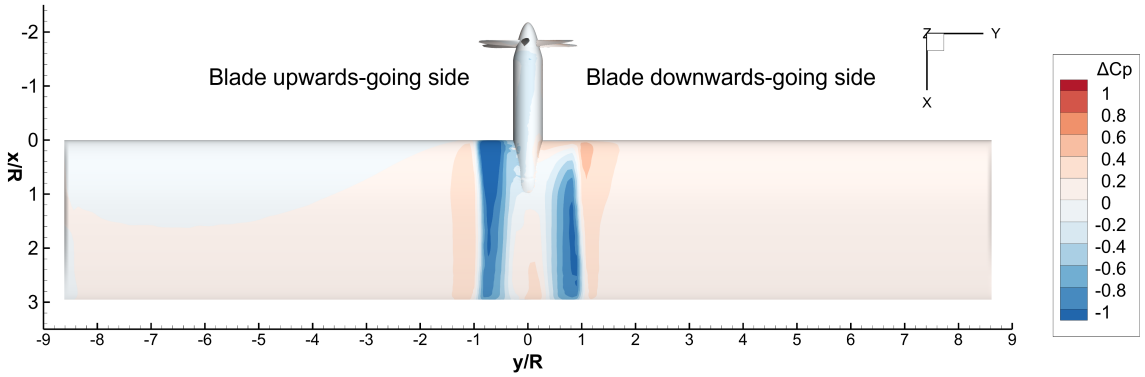

(a) *Top-view of the surface pressure coefficient difference between the SPA settings (OFF - ON)*

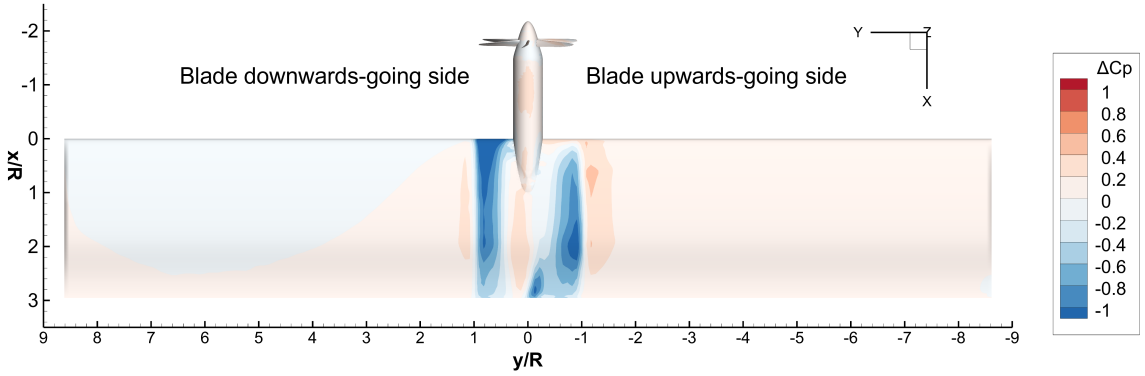

(b) *Bottom-view of the surface pressure coefficient difference SPA setting (OFF - ON)*

Figure 4.4: *Surface pressure coefficient difference plots for surface proximity avoidance settings from a top-view (a) and bottom-view (b) of the reference model at zero angle of attack*

4.2. Induced velocities

This section compares the total velocity ratios measured during the experiment [44] with the results of Flightstream. Experimental data was measured at the three axial locations as previously discussed in Figure 4.1. The comparison of the propeller analysis plane data can be seen in Figure 4.5, where from left to right, the experimental, Flightstream SPA setting ON and Flightstream SPA setting OFF data is presented, with the direction of the propeller rotating shown with the black arrow. The experimental data does not cover the entire domain as this was not possible to measure with the pressure probe arm presented by Duivenvoorden [29]. The contour values in the plots represent the velocity ratio $\frac{V}{V_\infty}$ with the arrows showing the in-plane velocities V_y and V_z. It can be seen that the velocity ratio is smaller for the SPA setting ON and OFF, compared to the experimental data. The SPA setting OFF velocities are slightly higher than for the SPA setting ON, but do not reach the same ratios as measured during the experiment. A possible explanation for this reduced total velocity is the small gap between the propeller blades and spinner, resulting in some airflow that leaks between the blade and spinner, as discussed for a different model in [35].

A 2D plot in the radial direction downwards (negative z-direction), as indicated in the contour plot, is presented in Figure 4.6. This direction was chosen because the experimental data samples in the vertical direction were denser, resulting in a more accurate comparison. The experimental settings, Flightstream SPA ON and Flightstream SPA OFF, are presented in

this figure, showing comparable results for both Flightstream analyses. The experimental velocity ratio is higher for smaller radial distances and returns to a velocity ratio of 1.0 at a lower radial distance from the hub. This indicates that slipstream contraction is captured during the experiment, which is missed by the analysis performed with Flightstream. The overall velocity ratio trend somewhat matched the results from the aerodynamic solver, but it is not completely accurate.

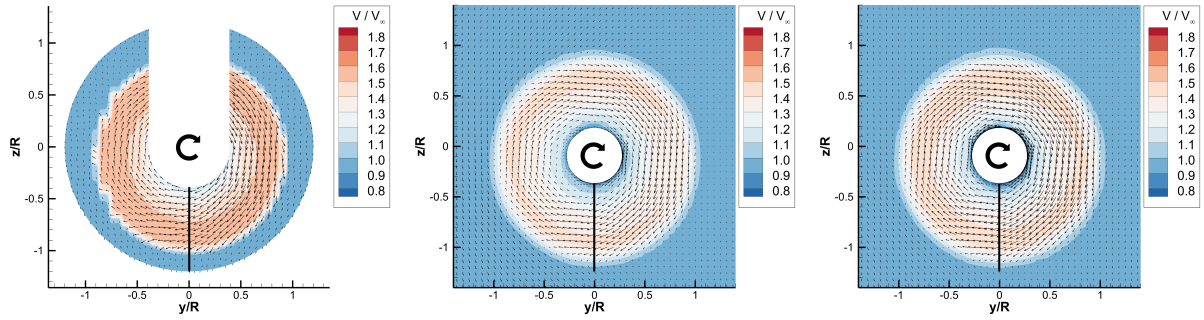

(a) *Velocity ratio plot for the experimental data at the propeller plane*

(b) *Velocity ratio plot for the Flightstream surface proximity setting ON data at the propeller plane*

(c) *Velocity ratio plot for the Flightstream surface proximity setting OFF data at the propeller plane*

Figure 4.5: *Velocity ratio contour plots with in-plane velocity vectors and propeller direction shown with a black arrow for the propeller plane experimental data (a), surface proximity setting ON data (b) and surface proximity setting OFF data (c)*

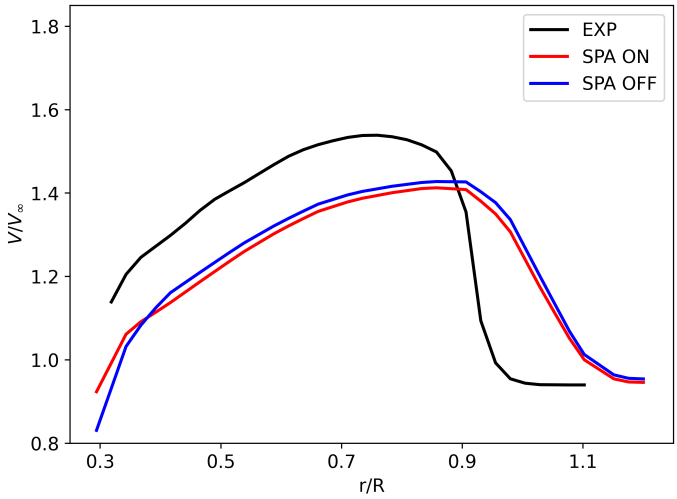

Figure 4.6: *Radial velocity ratio comparison between the experimental data and Flightstream result with SPA setting ON and OFF for the propeller plane at an angle of* 270° *to the positive y-axis as presented in the propeller velocity ratio contour plots*

The velocity ratio data for the nacelle analysis plane, as presented in Figure 4.7. The velocity ratio measured during the experiment is higher, and the SPA setting OFF captures this slightly better than the SPA setting ON. A small difference can also be seen in the deformation of the wake, represented by the red arrow, as the propeller slipstream seems to be

shifted slightly for the experimental data in Figure 4.7a. This deformation is not as visible in the Flightstream results with SPA setting ON or OFF, respectively shown in Figure 4.7b and Figure 4.7c. This indicates that Flightstream is not able to model the propeller slipstream deformation accurately. This is not necessarily an issue as long as the area of interest is relatively close to the propeller, which is the case for this thesis research. Figure 4.8 shows a 2D graph of the radial velocity ratio in the positive z-direction for the different contour plots, as also indicated in the contour plot with a black line. It can be seen that the velocities, determined during the experiment, are higher in this radial direction and that the velocity ratio for this plane also returns to the free stream velocity at a slightly smaller radial distance. This difference will most likely affect the thrust of vanes placed in this region, which will later be discussed when considering a vane location on the wing's surface.

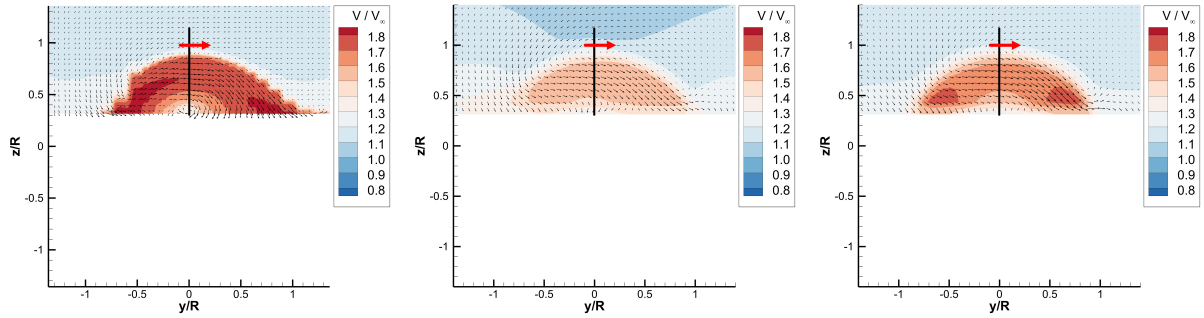

(a) *Velocity ratio plot for the experimental data at the nacelle plane*

(b) *Velocity ratio plot for the Flightstream surface proximity setting ON data at the nacelle plane*

(c) *Velocity ratio plot for the Flightstream surface proximity setting OFF data at the nacelle plane*

Figure 4.7: *Velocity ratio contour plots with in-plane velocity vectors and slipstream deformation shown with a red arrow for the nacelle plane experimental data (a), surface proximity setting ON data (b) and surface proximity setting OFF data (c)*

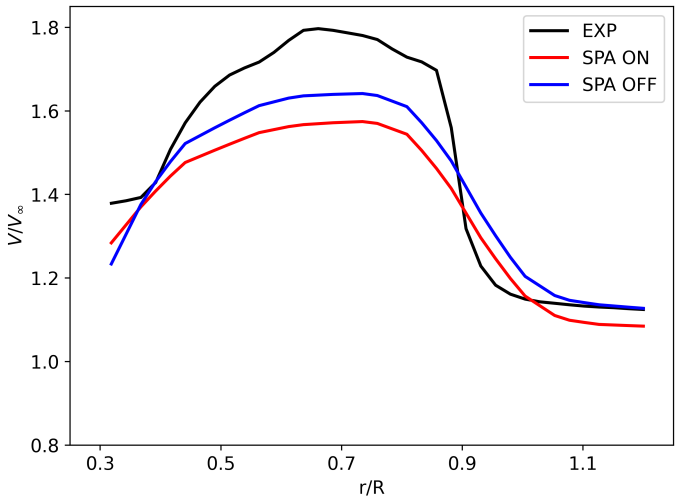

Figure 4.8: *Radial velocity ratio comparison between the experimental data and Flightstream result with SPA setting ON and OFF for the nacelle plane at an angle of* 90° *to the positive y-axis as presented in the nacelle velocity ratio contour plots*

The final velocity ratio comparison for the wake analysis plane is presented in Figure 4.9. This comparison shows that the experimental wake deformation is significantly greater compared to the Flightstream data. The general observation of lower velocity ratios is also true for the data comparison in this plane, with slightly better ratios for the SPA setting OFF. Another more noticeable difference is the more or less horizontal line present in the experimental data. This line is a result of the wake of the wing, which has a larger effect on the wake compared to what is shown in the Flightstream results. The velocity ratio comparison graph for the direction specified in the wake contour plots is presented in Figure 4.10. The velocity ratio matches for this plane better near the propeller tip ($r/R = 1.0$), but the experimental velocity ratio data is generally higher compared to the Flightstream data.

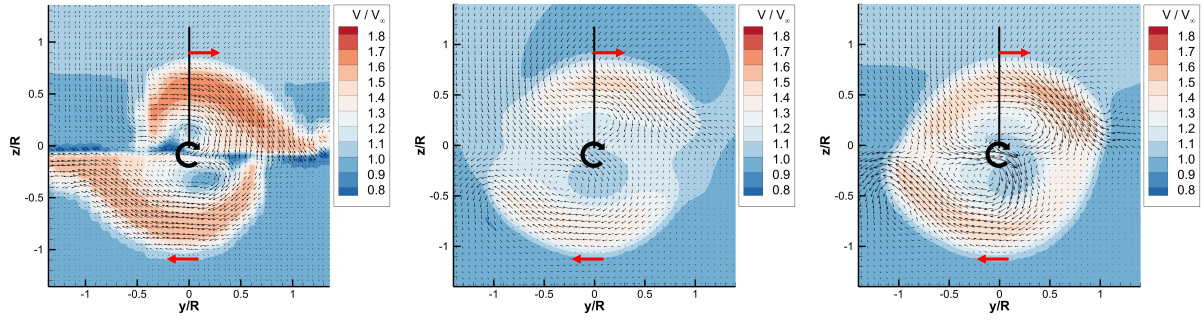

(a) *Velocity ratio plot for the experimental data at the wake plane*

(b) *Velocity ratio plot for the Flightstream surface proximity setting ON data at the wake plane*

(c) *Velocity ratio plot for the Flightstream surface proximity setting OFF data at the wake plane*

Figure 4.9: *Velocity ratio contour plots with in-plane velocity vectors, with the propeller rotation represented with a black arrow and the slipstream deformation shown with a red arrow for the wake plane experimental data (a), surface proximity setting ON data (b) and surface proximity setting OFF data (c)*

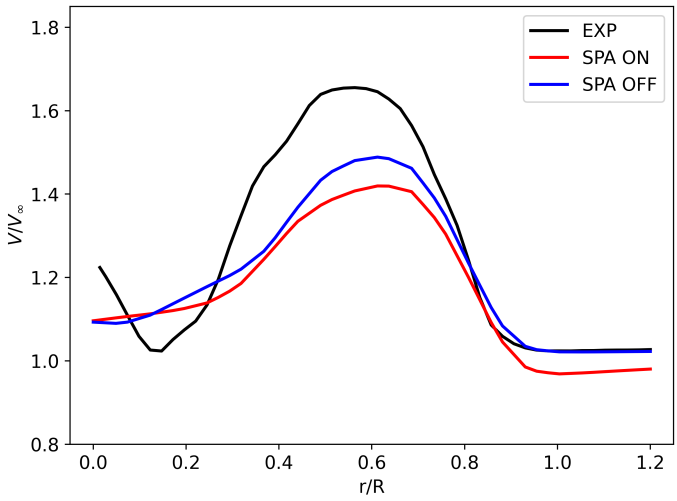

Figure 4.10: *Radial velocity ratio comparison between the experimental data and Flightstream result with SPA setting ON and OFF for the wake plane at an angle of* 90° *to the positive y-axis as presented in the wake velocity ratio contour plots*

The velocity ratio comparison with in-plane velocity vectors and 2D radial plots shows that the Flightstream results for both SPA settings capture an increase in the total velocity in the propeller slipstream. This increase is less compared to the experimental data, which is possibly a result of the gap between the propeller and spinner, where air can leak through [35]. The velocity vectors show that the wake deformation is not captured well when the flow is measured further from the propeller. This is expected with a low-mid-fidelity analysis method and should be taken into account when looking at the propeller slipstream behind a model.

4.3. Total pressure coefficient

This section will discuss the total pressure coefficient of the experimental and Flightstream data. The formula used by Duivenvoorden [29] for the total pressure coefficient of the experimental data is presented in Equation 4.1. The total pressure ratio is not a direct output variable of Flightstream, so this parameter had to be calculated separately. An important output variable of Flightstream for this was the static pressure ratio $\frac{p_{s,tot}}{p_{s,\infty}}$. The total pressure coefficient for the Flightstream data was calculated with Equation 4.2 as shown below. This formula is essentially the same as Equation 4.1 but with a rewritten numerator based on the available Flightstream data. The total pressure increase, as a result of the propeller, is purely based on the induced velocities and does not account for losses such as viscous effects, causing the pressure ratio to be overpredicted. The results of this chapter should therefore only be considered to be an approximation of the real total pressure ratio.

$$Cp_{T,EXP} = \frac{P_T - P_{s,\infty}}{q_\infty} \tag{4.1}$$

$$Cp_{T,FS} = \frac{\left(\frac{p_{s,tot}}{p_{s,\infty}} - 1\right) p_{s,\infty} + q}{q_\infty} \tag{4.2}$$

The total pressure ratio contour plots for the propeller plane are presented in Figure 4.11 below. The experimental data, once again, does not cover the entire domain for the reason stated earlier. It can be seen that the total pressure ratio of the Flightstream data for the SPA setting ON and OFF is a close match. The total pressure coefficient of the experimental data is lower compared to both Flightstream settings, as can be seen in Figure 4.12 for the radial direction in negative z-direction shown as a black line in the contour plots. The same slipstream contraction as discussed in the previous section can also be observed in the plot for the total pressure coefficient. The higher total pressure coefficients for the Flightstream data are most likely the result of viscous effects and more complex flow mixing, which reduced the total pressure coefficient of the experimental data. The slightly higher total pressure ratio in Figure 4.11c is the result of the plotting ranges being set equal for all planes. The total pressure ratio in the small region in the upper left is similar to the values determined for the SPA setting on in Figure 4.11b.

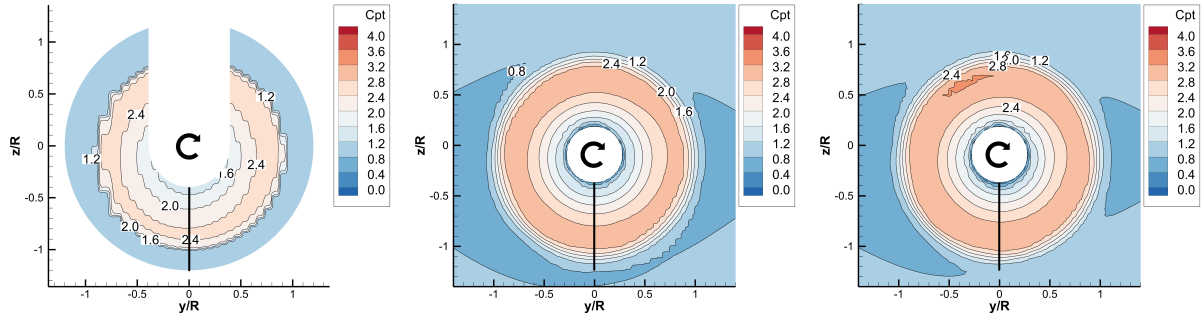

(a) *Total pressure coefficient plot for experimental data at propeller plane*

(b) *Total pressure coefficient plot Flightstream surface proximity ON data at the propeller plane*

(c) *Total pressure coefficient plot Flightstream surface proximity OFF data at the propeller plane*

Figure 4.11: *Total pressure coefficient contour plots with in-plane velocity vectors and propeller direction shown with a black arrow for the propeller plane experimental data (a), surface proximity setting ON data (b) and surface proximity setting OFF data (c)*

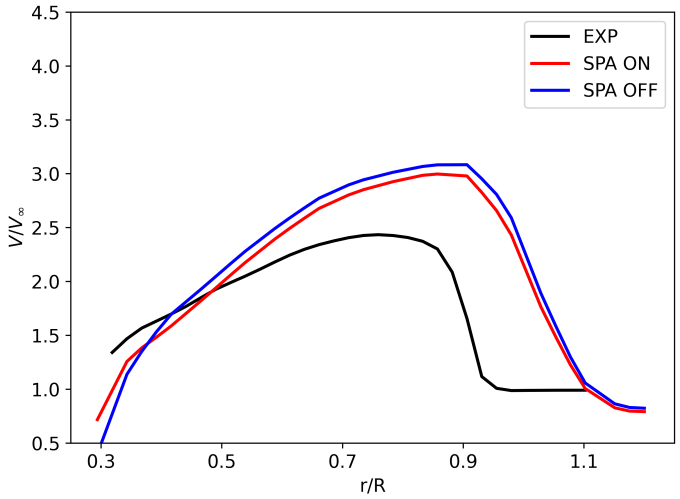

Figure 4.12: *Radial total pressure coefficient comparison between the experimental data and Flightstream result with SPA setting ON and OFF for the propeller plane at an angle of* 270° *to the positive y-axis as presented in the propeller velocity ratio contour plots*

The total pressure coefficients for the nacelle plane as presented in Figure 4.13 differ more from one another. The total pressure ratio ranges are the same for all plots, showing significantly higher values for the Flightstream plots. The reason for these higher values is the increased flow velocity over the upper surface of the wing, where this analysis plane is located. This difference between the experimental data and Flightstream results could also be attributed to the lack of viscous effects modelling in Flightstream, as stated for the propeller plane. This difference can also be seen in Figure 4.14, where the radial total pressure coefficients in the positive z-direction are compared. The lower total pressure coefficient lines are similar but differ in magnitude. This means that the relative positional aspects of interest for this thesis research are still captured, but the absolute values does not match the experimental data. Another observation is that a similar degree of slipstream deformation is visible as was discussed in Section 4.2.

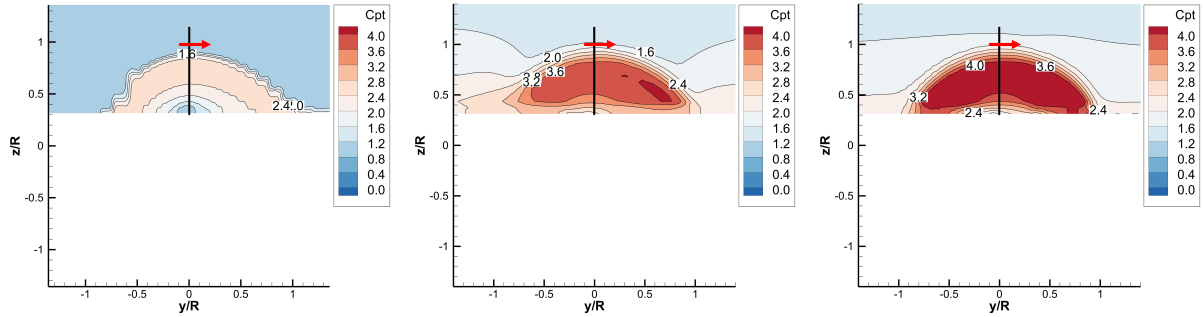

(a) *Total pressure coefficient plot for the experimental data at the nacelle plane*

(b) *Total pressure coefficient plot for the Flightstream surface proximity setting ON data at the nacelle plane*

(c) *Total pressure coefficient plot for the Flightstream surface proximity setting OFF data at the nacelle plane*

Figure 4.13: *Total pressure coefficient contour plots with in-plane velocity vectors and slipstream deformation shown with a red arrow for the nacelle plane experimental data (a), surface proximity setting ON data (b) and surface proximity setting OFF data (c)*

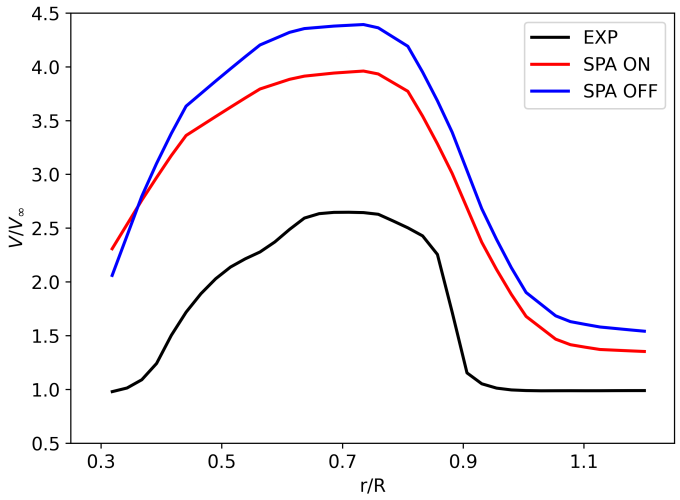

Figure 4.14: *Radial total pressure coefficient comparison between the experimental data and Flightstream result with SPA setting ON and OFF for the nacelle plane at an angle of* 90° *to the positive y-axis as presented in the nacelle velocity ratio contour plots*

The total pressure coefficient ratio of the wake plane and radial comparison in positive z-direction can be seen in Figure 4.15 and Figure 4.16. The wake is also, for this plane, less deformed in the Flightstream data. Some deformation is visible in the Flightstream results for the SPA setting ON and OFF (respectively Figure 4.15b and Figure 4.15c), but no horizontal wing wake line is captured. This is especially true in Figure 4.15b, where the wake elements are removed as a result of the SPA setting used. The radial total pressure coefficient data show that the experimental total pressure coefficients are lower compared to the Flightstream data, but match better compared to the propeller and nacelle plane, as discussed above.

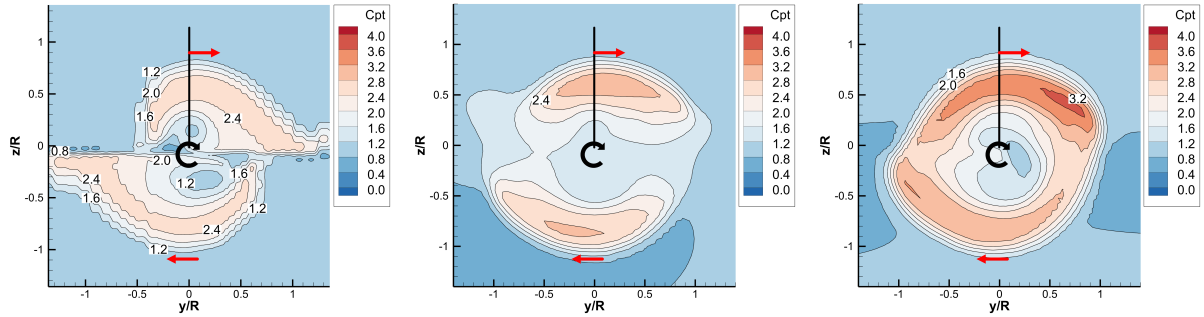

(a) *Total pressure coefficient plot for the experimental data at the wake plane*

(b) *Total pressure coefficient plot for the Flightstream surface proximity setting ON data at the wake plane*

(c) *Total pressure coefficient plot for the Flightstream surface proximity setting OFF data at the wake plane*

Figure 4.15: *Total pressure coefficient plots with in-plane velocity vectors, with the propeller rotation represented with a black arrow and the slipstream deformation shown with a red arrow for the wake plane experimental data (a), surface proximity setting ON data (b) and surface proximity setting OFF data (c)*

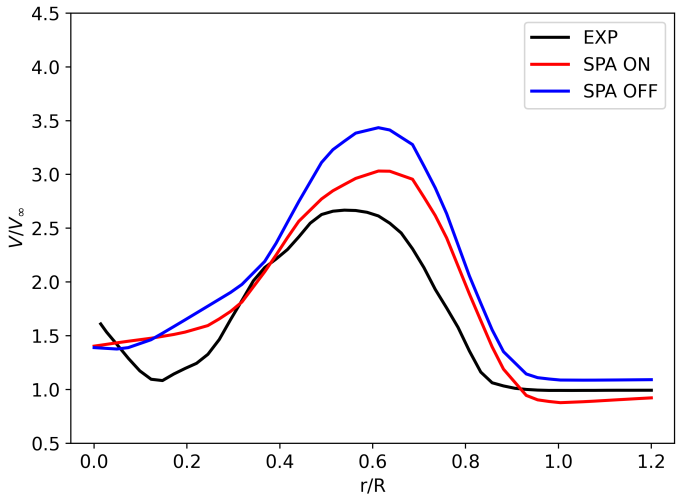

Figure 4.16: *Radial total pressure coefficient comparison between the experimental data and Flightstream result with SPA setting ON and OFF for the wake plane at an angle of* 90° *to the positive y-axis as presented in the wake velocity ratio contour plots*

The total pressure coefficient ratio plots for the propeller, nacelle and wake plane show that the total pressure coefficients are overestimated compared to the experimental data. This is because of the viscous and other more complex flow phenomena reducing the total pressure in the experimental data, which are not captured in Flightstream. The wake deformation is also less pronounced in the Flightstream data, as is expected with a low-mid fidelity aerodynamic solver. This thesis research focuses on the SRV total positional effectiveness, which is mainly a result of the local flow and not necessarily the total pressure ratio as presented in this section.

4.4. Propeller Thrust

The thrust coefficient of the isolated TUD-XPROP-S propeller at an angle of attack of 0° and advance ratio of 0.8 is equal to 0.412, as documented by Duivenvoorden [29]. This thrust coefficient was used as a reference for the different configurations tested in his work, which was determined to be adequate. This thesis research will take this same thrust coefficient as a reference value to compare with the thrust determined by Flightstream.

First, the propeller thrust, based on the reference thrust coefficient, is determined with Equation 4.3, as previously explained in Section 2.5. The variables in this equation, discussed in Chapter 3, result in a propeller thrust of 18.76 N. The propeller thrust is compared to the reference model results determined with both the SPA setting ON and OFF. The Flightstream propeller thrust forces for both settings are presented in Table 4.2, together with the just determined experimental thrust force.

$$T_C = \frac{T_p}{\rho_\infty V_\infty^2 D^2} \rightarrow T_p = T_C \rho_\infty V_\infty^2 D^2 = 0.412 \cdot 1.225 \cdot 30^2 \cdot 0.2032^2 = 18.76N \tag{4.3}$$

Table 4.2: *Propeller thrust force comparison for experimental isolated propeller at an angle of attack of* 0° *and Flightstream reference model results for SPA setting ON and OFF*

	Propeller Thrust [N]
Experiment	18.76
Flightstream SPA ON	25.29
Flightstream SPA OFF	24.94

It can be seen from the propeller thrust values presented in Table 4.2 that the experimental propeller thrust is significantly lower compared to the values determined by Flightstream. This difference is expected based on the differences in total pressure coefficient, discussed in Section 4.3, where the total pressure coefficient values of the Flightstream results are over-predicted.

4.5. Chordwise Pressure and Spanwise Lift distributions

This section describes the experimental pressure distribution data available for the reference model. These pressure data originated from the model's pressure tabs located at ±0.7 y/R. This allowed for a chordwise comparison of the pressure distributions at these spanwise locations, which will be discussed in Subsection 4.5.1. Flightstream also generates spanwise lift coefficient plots. The integrated chordwise and spanwise lift coefficient will be compared in Subsection 4.5.2.

4.5.1. Chordwise Pressure Distribution

An important difference was observed when evaluating the pressure distribution of the different SPA settings. The discussed reference model geometry in Section 3.1 mentioned the spanwise locations of two sets of surface pressure measurements performed during the experiment. These spanwise locations are ±0.7 y/R of which the results are shown in Figure 4.17. Figure 4.17a shows the pressure distribution for the blade upwards-going side (–0.7 y/R) and Figure 4.18b for the downwards-going side of the propeller (0.7 y/R).

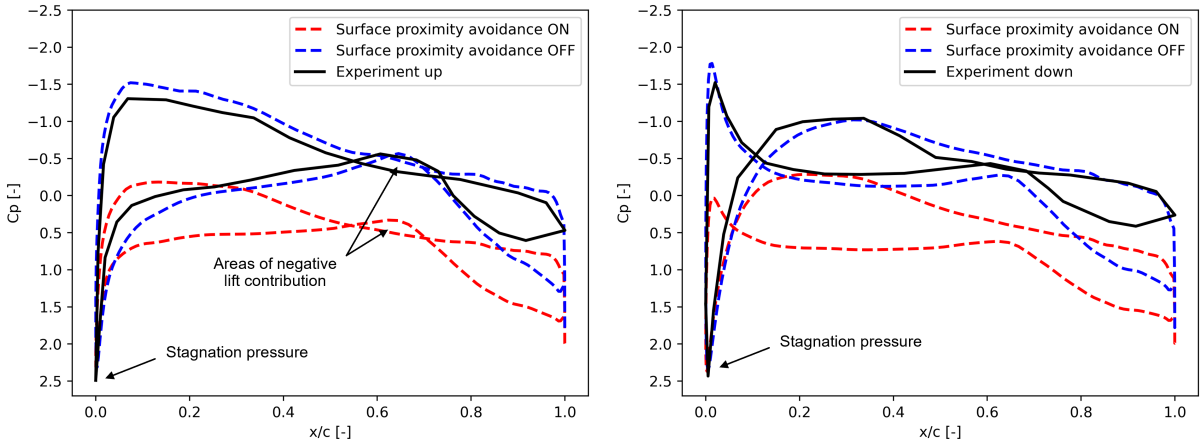

(a) *Pressure coefficient comparison between the experimental data and Flightstream data at* –0.7 y/R *(propeller upwards-going side)*

(b) *Pressure coefficient comparison between the experimental data and Flightstream data at* 0.7 y/R *(propeller downwards-going side)*

Figure 4.17: *Flightstream reference model pressure coefficient comparison plots with experimental data for propeller upwards-going (a) and downwards-going side (b)*

The pressure distribution in Flightstream is determined with the formula as presented in Equation 4.4, meaning that the pressure coefficient can not exceed 1.0. The increased dynamic pressure in the propeller slipstream is not included in the raw pressure coefficient data of Flightstream. This issue was addressed in a research paper from the University of Berlin [45]. The paper proposed and applied a correction factor as presented in Equation 4.5, where the q_{AD} is a 0th-order approximation of the additional dynamic pressure in the slipstream. This correction had the desired effect of improving the pressure distribution.

$$C_p = 1 - \frac{V^2}{{V_\infty}^2} \tag{4.4}$$

$$C_p = \frac{P_x - P_\infty}{q_\infty} + \frac{q_{AD}}{q_\infty} \quad \text{where,} \quad \frac{q_{AD}}{q_\infty} = \frac{T}{A_D q_\infty} \tag{4.5}$$

The figures presented in Figure 4.17 and Figure 4.18 have been corrected with this 0th-order correction and were respectively for the SPA setting ON and OFF 1.41 and 1.39 based on a propeller thrust for each setting. A first observation is that the pressure distribution of the surface proximity avoidance setting OFF matches the experimental data in both spanwise positions better compared to when this setting is turned ON. Figure 4.18 shows the pressure coefficient difference between the upper and lower surfaces for the Flightstream and experimental data. The data for the blade up- and downwards-going sides are respectively presented in Figure 4.18a and Figure 4.18b. Figure 4.18a shows that the surface proximity avoidance setting ON underpredicts the pressure distribution difference closer to the leading edge of the wing for the blade upwards-going side. This changes on the aft part of the airfoil, where the pressure distribution difference is overpredicted. The surface proximity setting OFF for the same spanwise position overpredicts the pressure distribution along the entire wing chord. The same analysis can be performed for the blade downwards-going side

as presented in Figure 4.18b. In this case, both pressure distributions follow the experimental data better, but both overpredict the pressure coefficient. This overprediction results in a higher spanwise lift coefficient, as will be discussed in the next subsection.

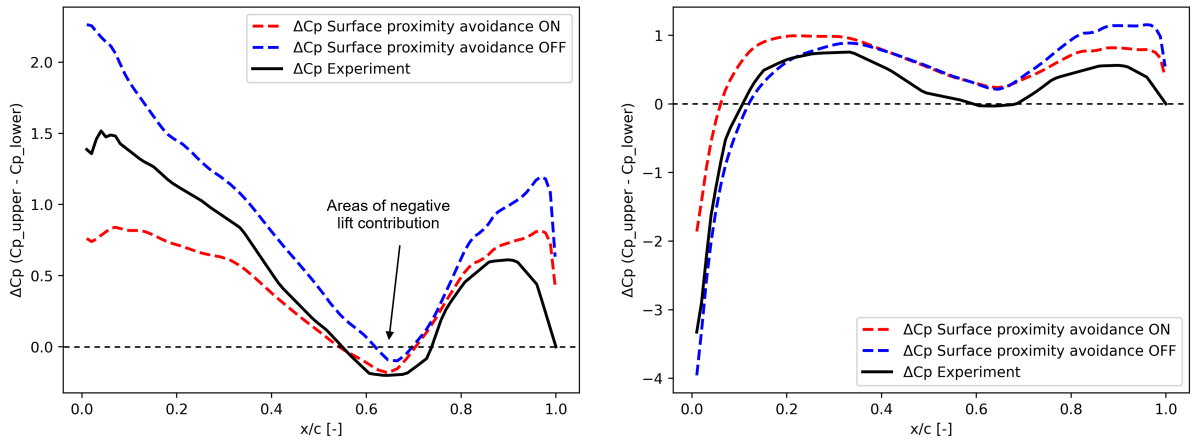

(a) *Pressure coefficient difference comparison between the experimental data and Flightstream data at* –0.7 y/R *(propeller upwards-going side)*

(b) *Pressure coefficient difference comparison between the experimental data and Flightstream data at* 0.7 y/R *(propeller downwards-going side)*

Figure 4.18: *Flightstream reference model pressure coefficient difference comparison plots with experimental data for propeller upwards-going (a) and downwards-going side (b)*

4.5.2. Spanwise Lift Distribution

The spanwise lift distribution as determined by Flightstream is presented in Figure 4.19. This figure shows the spanwise lift distribution for both the surface proximity setting ON and OFF, as well as the integrated values of the chordwise pressure distributions from Subsection 4.5.1. The values corresponding to these integrated lift coefficients are presented in Table 4.3.

It can be seen that both surface proximity settings capture an increase in lift on the blade upwards going side (negative y/b) and a decrease in lift on the blade downwards going side (positive y/b). The SPA setting ON distribution is smoother compared to the SPA setting OFF due to the elimination of the wake elements close/intersecting with the model geometry. The SPA setting OFF is more spiky and can be seen to have a jump on the blade's downwards-going side. This is most likely due to unrealistic wake interactions with the wing.

The integrated values, as shown in the figure, match the spanwise lift distribution on the blade upwards-going side but are less accurate on the blade downwards-going side. This is especially true when the SPA setting is OFF, where the integrated value is almost the same as for the SPA setting ON case. This is strange considering that the spanwise lift distribution for this setting is much lower at the same spanwise position. The difference can be explained by considering the methods used to determine both values.

First, the integrated pressure distribution values as presented in Table 4.3 are considered. These values are based on the C_p integral of the surface pressure distributions given in Figure 4.17. The experimental data in these figures were obtained from the experiment, and

the Flightstream data is the result of the formula for C_p (Equation 4.4) with the correction factor applied. The main takeaway from this is that the formula for C_p only uses the local velocity to determine the surface pressures. The location of the pressure tabs and chordwise pressure distribution is within the propeller slipstream, where the swirl velocity greatly affects the airflow. This can also be seen in Figure 4.7, where the velocity and swirl are higher near the surface of the wing. This increased velocity overestimates the underpressure on the upper surface on the downwards-going side, which results in the lift coefficients being larger than in reality.

The spanwise lift distribution is not based on the same pressure distribution integral and is therefore different. The spanwise lift distribution, in Flightstream, is based on the method of integrated circulation as described by Ahuja et al. [46]. This method evaluates the vorticity along a series of two-dimensional cross sections aligned with the free stream velocity. The vorticity is determined for each of these cross sections based on the generalised formula for circulation Equation 4.6, which is then used to calculate the section lift with Equation 4.7 [31], as also stated in the Flightstream documentation. The sectional lift coefficient can then be calculated with Equation 4.8. This method of integrated circulation is less sensitive to the tangential velocities in the propeller slipstream and finds different values for the lift coefficients at the spanwise pressure tab locations.

Figure 4.19 shows this difference in lift coefficient, where the red and blue lines are the Flightstream output data for the SPA setting ON and OFF. These are based on the method of integrated circulation, whereas the data points in this plot have been determined by integrating the chordwise pressure distribution. It can be seen that the lift coefficient on the blade upwards-going side, determined with the SPA setting ON, matches the experimental data. The SPA setting OFF overestimates the lift coefficient as a result of the higher induced velocities near the surface of the wing. Something different can be seen on the blade's downwards-going side, where the integrated pressure data of the SPA setting OFF does not match the method of integrated circulation for the same setting. The method of integrated circulation approaches the lower experimental lift coefficient, but shows some unrealistic behaviour in the form of a lift coefficient jump.

$$\Gamma = \oint_A \vec{V} ds \qquad (4.6) \qquad L' = \rho_\infty V_\infty \Gamma \qquad (4.7) \qquad C_l = \frac{L'}{q_\infty c_{ref}} \qquad (4.8)$$

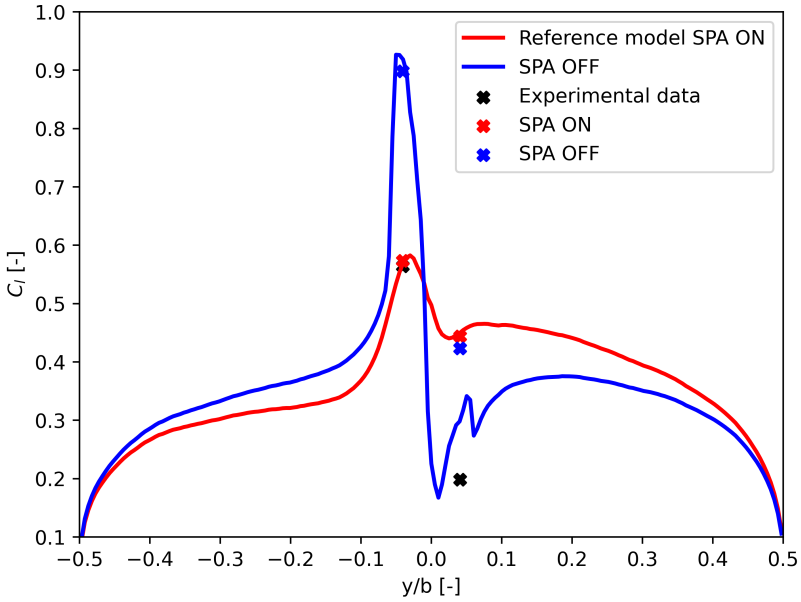

Figure 4.19: *Spanwise lift distribution comparison for the reference model between experimental data and Flightstream results for the SPA setting ON and OFF with integrated pressure coefficient data points from experimental and pressure distribution Flightstream data added for each setting*

Table 4.3: *Lift coefficient values for experimental data and Flightstream results, where ON and OFF represent the surface proximity avoidance setting used*

	Blade upwards-going side	**Blade downwards-going side**
Experiment	0.5639	0.1984
Flightstream SPA ON	0.5736	0.4440
Flightstream SPA OFF	0.8984	0.4233

4.6. Validation Conclusions

The validation for this thesis research is based on the experimental wind tunnel data of the reference model collected by Duivenvoorden et al. [44]. This dataset includes velocity and total pressure data at several axial positions, which are compared to the Flightstream results with SPA setting ON and OFF. The velocity ratio comparison with the in-plane velocity vectors shows that Flightstream captures an increase in total velocity, but that these total velocities are underpredicted compared to the experimental data. Part of this observation is attributed to the small gap present between the propeller blades and spinner to prevent solver divergence, as also noted by Beyne [35], discussed in Chapter 3. It was noticed that the total axial and planar velocities of the SPA setting OFF were larger, as the velocity-inducing wake elements were not removed near the model geometry. The overall wake deformation was found to be somewhat captured accurately near the propeller but degraded when the distance from the propeller increased.

The total pressure coefficient comparison, similar to the velocity data, showed that the wake deformation was less accurate for the wake plane. The total pressure coefficient was, for both SPA settings, higher than the experimental data, which is attributed to the fact that viscous and complex flow effects, which reduce the total pressure in real-life conditions, and are not captured by Flightstream. A potential flow solver does not directly determine the total pressure in the propeller slipstream, meaning that the values, as determined with the Flightstream data, are only a representation of the increased total pressure. The main focus of this thesis research is the placement of SRVs, which is mainly dependent on the induced flow velocities and is less affected by the total pressure ratio. This means that this over-estimation of the total pressure ratio is less important for the relative vane performance.

The just-mentioned velocity and total pressure coefficient relate to the propeller thrust. It was found, based on the experimental thrust coefficient, that Flightstream overpredicts the propeller thrust. This is in line with the higher total pressure coefficients behind the propeller presented in the respective contour plots.

The chordwise pressure and spanwise lift distribution show that the method of determining the C_p and spanwise lift has a significant effect on the results within the propeller slipstream. The manually performed pressure distribution integral is based on the velocity ratio, which includes propeller swirl velocity components. This affects the lift coefficients and is different from the spanwise lift distribution in Flightstream, which is based on the method of integrated circulation. This, combined with the SPA setting ON and OFF effects, made the comparison with the available experimental data difficult.

The overall conclusion of this validation chapter is that Flightstream is not able to accurately model the aerodynamic propeller slipstream properties as measured during an experiment. Flightstream underpredicts the flow velocity and overestimates the total pressure coefficient at the measured axial locations, resulting in overestimated propeller thrust values. The slipstream deformation and contraction are less pronounced for both SPA settings used in the Flightstream analyses. The available chordwise pressure and spanwise lift distribution were difficult to compare, as the chordwise pressure was based on total velocities, which would be different in the propeller slipstream.

The aerodynamic solver Flightstream will, despite these shortcomings, be used for the further analysis of the modified model configurations, as a relative performance comparison is still valid. The final results will thus be able to state which of the tested model configurations performs best, but does not represent absolute performance values.

5

Model Modifications

This chapter describes the model modifications of the reference model to determine the effectiveness of placing SRVs on the model geometry. There are two main aspects to consider for the model modifications. These are the individual SRV design and the placement of these SRVs, which will be discussed in respectively, Section 5.1 and Section 5.2 below. Section 5.3 discusses the different design configurations for this thesis research and is followed by Section 5.5, where a short chapter conclusion is presented with the most important aspects discussed in this chapter.

5.1. SRV Design

It is important to consider the design aspects of an SRV before placing a vane on the model, as this will significantly impact the vane's overall performance. The SRV, as used in this thesis research, is described in this section. First, the vane airfoil profile is discussed in Subsection 5.1.1, after which Subsection 5.1.2 discusses the general planform characteristics of the vane.

5.1.1. SRV airfoil Profile

The first thing to consider for the SRV design is the airfoil profile that will be used. A sensitivity study was performed on the influence of different airfoil profiles to prevent unnecessarily complicated design procedures without significant effects. This sensitivity study was performed with a self-made blade element-like sectional lift method analysis code. This code is based on known inflow conditions and determines spanwise forces based on 2D lift polars from XFOIL[1]. The general setup of this code can be found in Appendix B. This sensitivity study is based on the axial and tangential inflow conditions a presented in Figure 5.1, which were taken from Li et al. [47]. Li et al. used these inflow conditions for a lifting line optimisation model to optimise for vane thrust, which was validated with a RANS CFD analysis and an experiment.

[1]XFOIL Subsonic Airfoil Development System by M. Drela, H. Youngren, version 6.99 (2000).

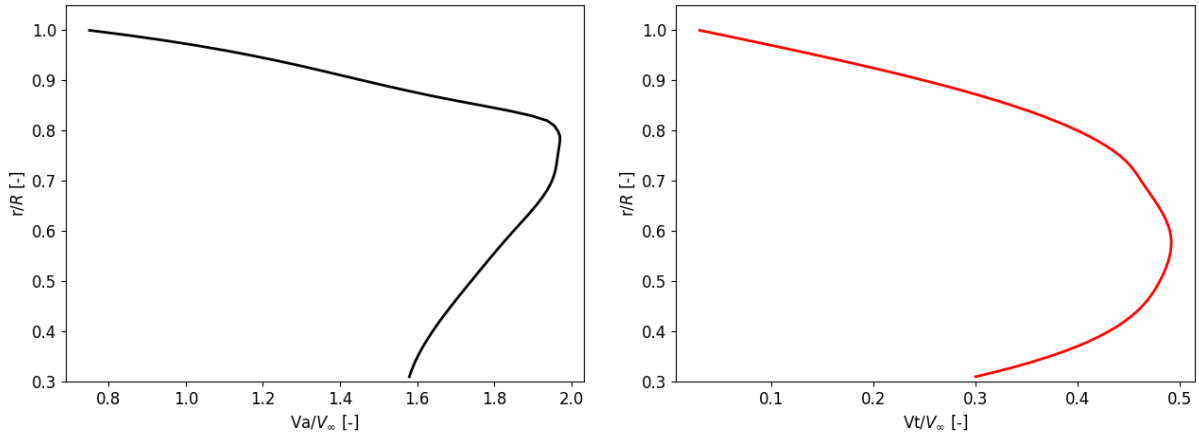

(a) *Radial axial inflow condition used for sensitivity analysis* **(b)** *Radial tangential inflow condition used for sensitivity analysis*

Figure 5.1: *Axial and tangential SRV inflow conditions used by Li et al. [47] to determine the optimal SRV design*

The optimised SRV design for the shown inflow conditions, found by Li et al. [47], can be seen in Figure 5.2. Figure 5.2a shows the SRV planform with root and tip chord dimensions given in millimetres, Figure 5.2b shows the radial blade pitch distribution denoted by β and optimal circulation distribution $\Gamma/(2\pi RV_\infty)$, and Figure 5.2c presents the optimised blade form curves. The blade curve ratios in this figure are: maximum thickness (t/c), maximum thickness position (t_p/c), maximum camber (h/c), maximum camber position (h_p/c) and chord length (c/R_{SRV}). The conditions for which these SRV optimised parameters were found can be seen in Table 5.1, where the used propeller is a six-bladed propeller with a diameter of 0.406 m and blade pitch angle of 30° at 0.70 r/R. The additional thrust for four vanes with this optimised vane was determined to be 3.4 % of the propeller thrust with a lifting line model and 2.6 % based on a performed experiment. This lower experimental thrust was attributed to the fact that additional drag was added to the vanes during the experiment in the form of transition strips.

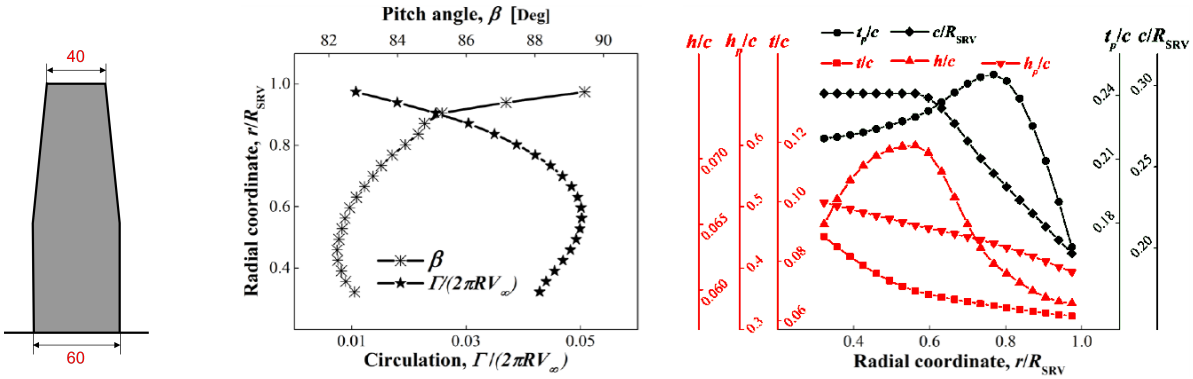

(a) *Optimised SRV platform illustration* **(b)** *Radial pitch angle and circulation distribution for optimised SRV* **(c)** *Blade thickness, chord and camber curves for optimised SRV*

Figure 5.2: *Optimised SRV vane design based on the findings of Li et al. [47], where the general SRV platform (a), radial pitch and circulation distribution (b) and blade form curves (c) are presented*

Table 5.1: *SRV optimisation conditions used by Li et al. [47]*

Parameter	Symbol	Value	Unit
Propeller thrust coefficient	C_{PT}	0.322	–
Free stream velocity	V_∞	29.0	m/s
Reynolds number	Re	$2.625x10^5$	–
Advance ratio	J	0.6	–
Propeller diameter	D	0.406	m

The created blade element-like code would use straight NACA 4-series profiles to determine if an optimised vane would be significantly better. The vanes for this analysis all have a span equal to the propeller radius and a chord of 0.05 m. This planform is similar to the optimised vane found by Li et al. [47]. The SRV incidence angle was set to –7° as this is approximately the average blade pitch of the optimised wing presented in Figure 5.2b. Four different NACA 4-series airfoils were tested to determine the effect of camber as well as thickness. NACA 4-series airfoils are defined by three shape parameters: maximum camber, location of maximum thickness and maximum thickness. An example would be a NACA2412 airfoil, which, according to this system, would have a maximum camber of 2 % of the chord, which would be placed at 40 % of the chord length. The last two digits represent the maximum thickness, which would thus be 12 % of the chord [48]. The four airfoils chosen for this test are: NACA 0012, NACA 0015, NACA 2412 and NACA 2415. These particular profiles were chosen because the parameters of interest for this analysis study (blade thickness and camber) are well represented and documented.

The results of this analysis, compared to the optimised vane lifting line model design, can be seen in Table 5.2. The vane thrust in this table is presented as an absolute thrust value in newtons and a percentage of the propeller thrust found by Li et al. [47]. It can be seen that the airfoil camber has a more significant effect on the vane thrust compared to a thicker airfoil. This is because a cambered airfoil produces positive lift at zero angle of attack [31]. The drawback of camber is that the stall angle will be lower as the adverse pressure gradient is larger. Another observation is that the vane thrust of the optimised lifting line code is lower compared to the results of the self-performed analysis. This is because the code does not consider a finite wing but purely 2D aerodynamics and forces. These forces are based on the inflow conditions and will overpredict the forces, especially near the blade tip.

Table 5.2: *blade element-like analysis vane thrust results in absolute and percentage performance values compared to the findings of Li et al. [47]*

Profile	Vane thrust [N]	Vane thrust [%T_p]
Li et al. [47]	5.49	3.40
NACA 0012	6.79	4.45
NACA 0015	7.14	4.68
NACA 2412	8.80	5.77
NACA 2415	9.04	5.92

It was decided, based on the similar performance of the various analyses performed, that an SRV with a uniform symmetric airfoil profile would be an appropriate design choice. The performance differences of vanes placed at different locations on the model would be representative, even if the overall performance of an optimised vane could potentially improve the efficiency further. A second reason for choosing a symmetric profile is that a symmetric airfoil would allow for a fair comparison between all different locations. The thickness ratio was determined by looking at the average thickness of the optimised airfoil, which was $\approx$0.07 t/c. This vane was designed for a propeller twice as large compared to what will be used in this thesis research. A NACA 0012 profile was therefore chosen to allow for a vane to be fabricated for a possible later experiment.

5.1.2. SRV Planform

It is important to keep the SRV platform relatively simple to perform a fair comparison. The main parameters to be determined were the SRV chord length and span. The optimised vane design by Li et al. [47] was used as a reference to determine the platform parameters for this thesis research. A previous research by Avallone et al. [27] used the same optimised vane to determine the effect of SRV length on the performance as previously discussed in Section 2.4. This paper aimed to reduce the noise production of the propeller and vane combination by preventing the propeller tip vortices from impinging on the SRV. Shorter vanes were observed to have a reduced vane thrust, while there was no reduction in far-field noise measured. Based on these findings, it was determined that the vanes would, for the purpose of this thesis, have a span equal to the propeller blade radius.

The chord length for this research is based on the averaged chord of the optimised vane by Li et al. [47]. The average chord length for the optimised vane was found to be 0.05 m, which would be used for this research, but scaled with a factor of 0.5 to account for the smaller TUD-XPROP-S propeller.

5.2. SRV positioning

The next step is to decide where to position the just-defined SRVs. Subsection 5.2.1 will start by considering the axial and radial positioning of the SRVs. Subsection 5.2.2 will then discuss the incidence angle at which the SRVs are placed on the reference model.

5.2.1. SRV Axial and Radial Positioning

This thesis research aims to determine the optimal SRV location as stated in the research sub-questions. Three different axial locations have been chosen based on distinct relative propeller positions. The axial positions are presented and coloured in Figure 5.3 below. Both the red and green vanes are located on the nacelle and are placed respectively at a location of –0.75 D and –0.25 D with respect to the leading edge of the wing. These vanes aim to determine if a vane close to the propeller (red) performs better than a vane placed further away (green). The blue vane is placed on the wing at a distance of 0.50 D on the upper surface of the wing to look into the effect of the wing on the vane performance.

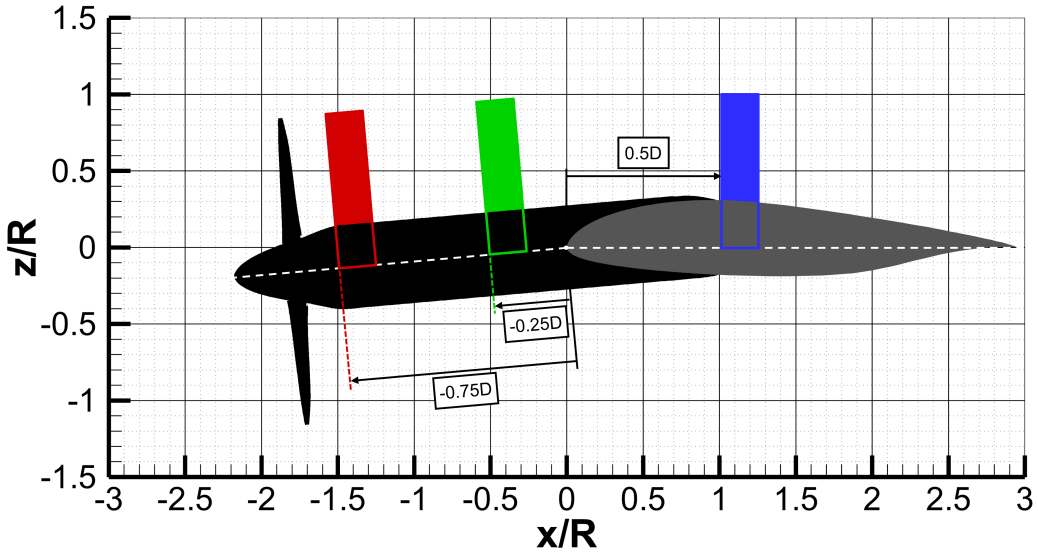

Figure 5.3: *SRV axial placement overview on reference model geometry showing three different axial positions considered in this research*

Two positions will be tested for each axial position based on an initial and optimal vane location. The initial SRV would be placed vertically in the positive z-direction. This vane orientation was chosen to allow all initial vanes to be placed at the same orientation to the model without affecting the flow near the surface of the wing. The limiting case for this is the vane on the upper surface of the wing, where an angled vane would introduce super velocities near the intersection of the vane and the wing's surface. A second vane would represent the optimal placement for maximum vane thrust generation. The locations of these optimal positions per axial location were determined by analysing the flow conditions at –0.75, –0.25 and 0.50 D. At these locations, an analysis plane was added with a height and width of twice the propeller diameter. The analysis planes and corresponding positional parameters are presented in Figure 5.4 and Table 5.3. It should be noted that these planes have the same orientation as the reference coordinate system for all planes. This was done to allow for easy data manipulation and to keep the orientation similar to the planes used in the validation. Angling the plane with 5° to correct for the local flow velocities at the –0.75 and –0.25 D vanes was determined not to be necessary, as the velocity data would be practically identical.

Table 5.3: *Analysis plane locations along the x-axis compared to the wing leading edge for SRV placement*

Analysis plane	**x [m]**	**x/c [-]**	**x/R [-]**
–0.75 D	-0.152	-0.507	-1.496
–0.25 D	-0.051	-0.170	-0.502
0.50 D	0.102	0.340	1.004

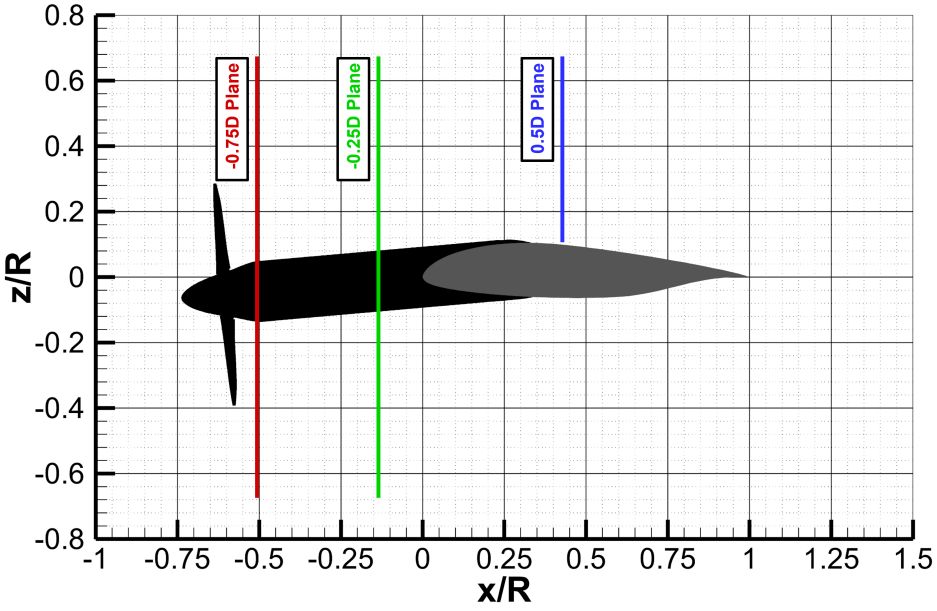

Figure 5.4: *Analysis plane placement overview on the reference model geometry for SRV positioning analysis*

The force factor, as described in Section 3.3, was used to determine the optimal SRV positioning for vane thrust generation. The averaged data of the analysis planes were used to create force factor contour plots for each axial position. Three force factor contour plots can be seen in Figure 5.5, where the –0.75, –0.25 and 0.50 D analysis planes are presented in respectively Figure 5.5a, Figure 5.5b and Figure 5.5c. These contour plots are for the SPA setting ON case and present datum reference lines for the relative positioning of the initial and optimal SRV locations. The force factors for the radial angles theta are integrated for the –0.75 and –0.25 D planes to determine the optimal radial location of the vane. The analysis plane on the wing changed in spanwise direction (y/R). This was done to keep the wetted area of the vanes equal for all positions and prevent complex flow phenomena at a relatively small angle with the wing's upper surface. The integrated force factor values for each of the radial and spanwise locations are presented in Figure 5.6. Both surface proximity avoidance settings are presented in this figure per axial position, and the locations for maximum values are marked. The optimal SRV locations based on these plots for the SPA setting ON and OFF, as well as the average values, can be found in Table 5.4.

The optimal radial positions for both the –0.75 and –0.25 D analysis planes are located close to the datum line (0°). This means that the optimal position is near horizontal on the blade's downward-going side of the propeller. The blue box in Figure 5.6b marks an interesting region of the plot as the force factor seems to locally increase just above the wing on the blade upwards-going side. This can be explained by considering that the –0.25 D analysis plane is located just in front of the wing, where the flow is affected by the upwash of the wing. This upwash increases the local angle of attack, which in turn increases the lift and thrust potential of the vane. Figure 5.6c differs from the other plots in the figure as the position is different. The optimal SRV placement is, according to this figure, located at a slightly negative y/R location, which is on the blade upwards-going side.

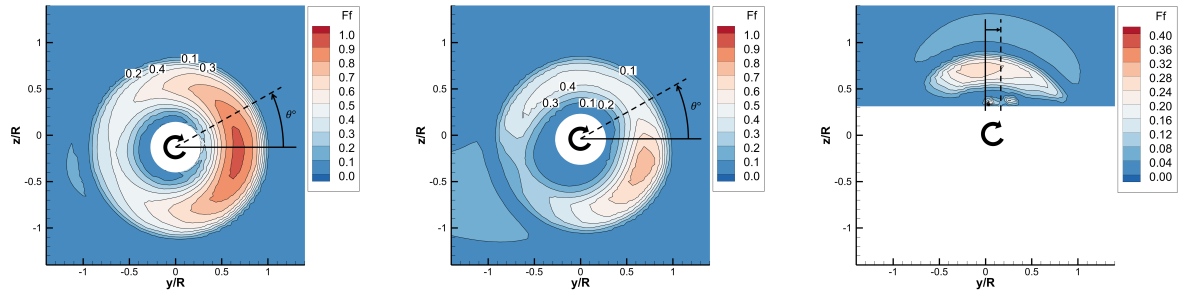

(a) *Force factor contour plot for the* –0.75 D *analysis plane (rear-view)*

(b) *Force factor contour plot for the* –0.25 D *analysis plane (rear-view)*

(c) *Force factor contour plot for the* 0.50 D *analysis plane (rear-view)*

Figure 5.5: *Force factor plots with datum line annotation for* –0.75 D *(a),* –0.25 D *(b) and* 0.50 D *(c) analysis plane with surface proximity avoidance setting ON and propeller rotation shown with a black arrow*

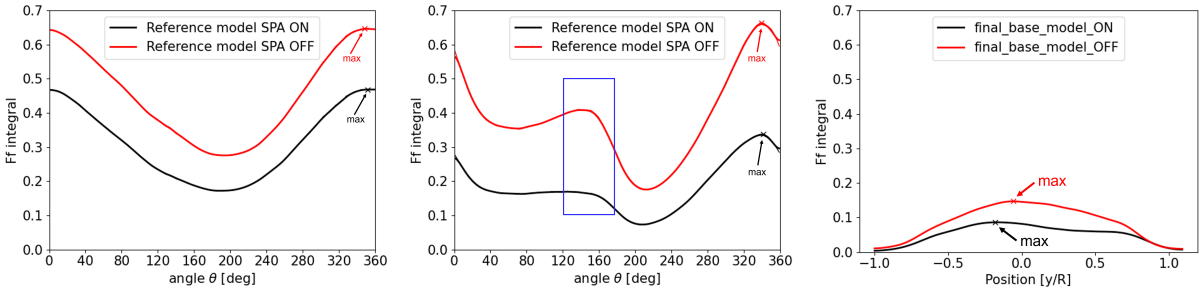

(a) *Force factor integral values for radial* –0.75 D *plane with both SPA settings and locations of maximum values indicated*

(b) *Force factor integral values for radial* –0.25 D *analysis plane with both SPA settings and locations of maximum values indicated and an area of increased Ff marked with a blue box*

(c) *Force factor integral values for spanwise* 0.50 D *analysis plane with both SPA settings and locations of maximum values indicated*

Figure 5.6: *Analysis plane Force factor radial integral values for analysis planes*–0.75 D *(a),* –0.25 D *(b) and* 0.50 D *(c)*

Table 5.4: *Optimal SRV positioning according to force factor integral values for each analysis plane and SPA setting*

	–0.75 D	–0.25 D	0.50 D
Optimal positioning SPA ON	352 [deg]	341 [deg]	-0.18 [y/R]
Optimal positioning SPA OFF	348 [deg]	339 [deg]	-0.06 [y/R]
Averaged optimal positioning	350 [deg]	340 [deg]	-0.12 [y/R]

The final SRV positions for each of the previously discussed initial and optimal vane locations can be seen in Figure 5.6. The illustrations in this figure show a vertical (initial) and optimal SRV location for the analysis planes.

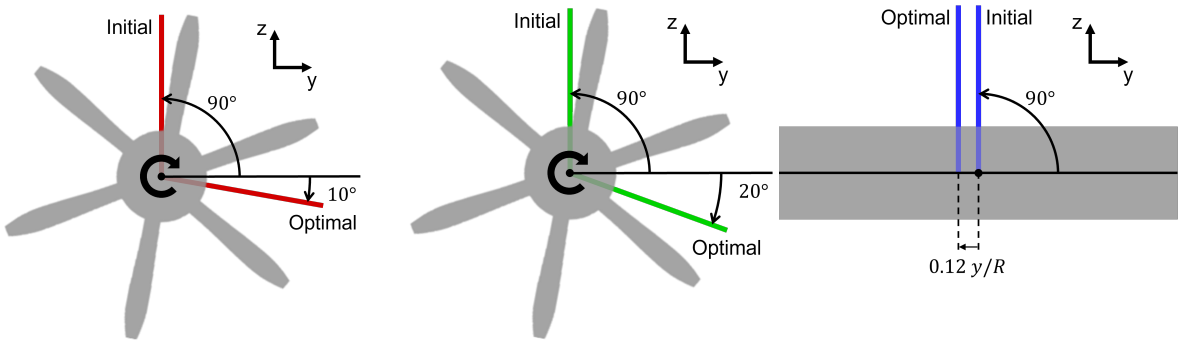

(a) *SRV initial and optimal placement* –0.75 D *(rear-view)*

(b) *SRV initial and optimal placement* –0.25 D *(rear-view)*

(c) *SRV initial placement* 0.50 D *(rear-view)*

Figure 5.7: *SRV positions relative to the positive y-axis for* –0.75 D *(a),* –0.25 D *(b) and* 0.50 D *(c), where the initial and optimal placement based on the force factor integral are presented as well as the propeller rotation direction*

5.2.2. SRV incidence angle

The SRVs, as just described, have to be placed on the reference model to determine the axial propulsive efficiency. The local angle of attack will have a significant effect on the vane performance, which is why an incidence angle is considered for all vanes that are to be placed on the model. This will be done to prevent vanes from stalling, resulting in an unfair comparison of the overall performance. The local experimental angle of attack values, presented in a contour plot and radial angle of attack distribution, for the propeller plane are presented in Figure 5.8 below. The propeller plane, from the experimental data, was chosen as this is the most accurate representation of the flow for the different vane locations.

The local angle of attack values shown are the average values of the performed experiment and show an area with a local maximum angle of attack of approximately 15°. This local maximum is located on the blade downwards-going side just below the horizontal y-axis. It should be noted that this average value does not represent the absolute maximum local angle of attack, which could be slightly higher for a particular timestep. This unsteady effect will later be considered in Section 6.1, where relatively small differences between the different timesteps are observed.

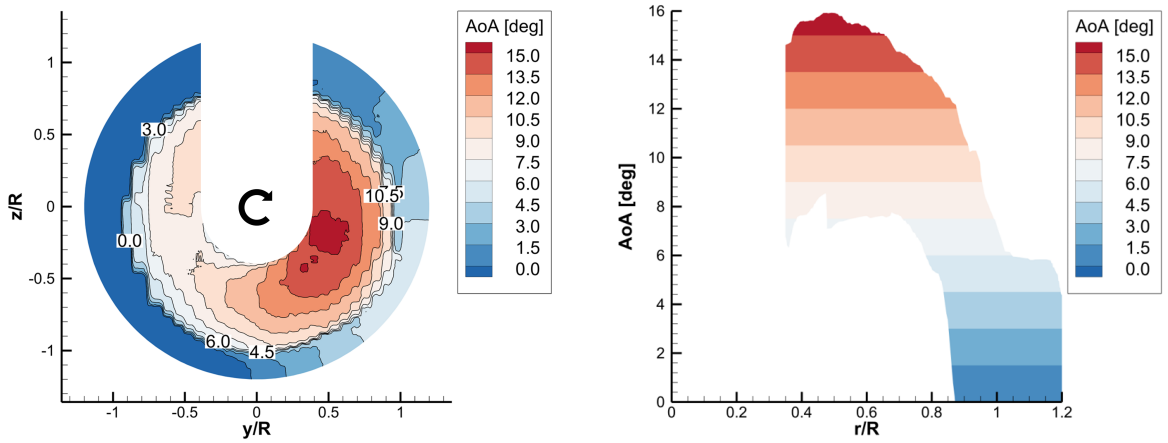

(a) *Experimental angle of attack contour plot for the propeller plane with indicated propeller rotation direction*

(b) *Radial angle of attack plot for experimental propeller plane*

Figure 5.8: *Experimental local AoA contour (a) and radial distribution (b) plot showing the average AoA for the propeller plane*

The incidence angle for the vanes will be based on this found maximum of 15°, and the polar plot for the NACA 0012 airfoil profile. The polar plot for the NACA 0012 airfoil is presented in Figure 5.9. This polar is obtained with XFOIL[2] and is based on the local average inflow conditions of the vane in the propeller slipstream. A maximum C_l value of 0.95 is obtained at an angle of attack of 10.2°, which is approximately 5° lower than the local maximum angle of attack observed in Figure 5.8a. A lift coefficient of 0.95 initially seems low for a NACA 0012 airfoil until the relatively low Reynolds number of the vane is considered. Equation 5.1 shows the formula to calculate the Reynolds number, where the air density (ρ), local flow velocity (V), characteristic length (d) and dynamic viscosity (μ) at the vane location are used. This results in a local Reynolds number of 7.75×10^4. [31]

$$Re = \frac{\rho V d}{\mu} \tag{5.1}$$

It was decided, based on contour and polar plot, to set all vanes at an incidence angle of 5° with respect to the local Z-axis. The definition of the incidence angle is presented in Figure 5.10 and will prevent any vane from experiencing stall. The vane performance as a result of this vane placement will be indicative of where the most propeller swirl can be found and thus indicate what the optimal vane position is when interactions are accounted for.

The unsteady effects will, in this analysis, not cause problems as the solver is an inviscid solver, which assumes a linear relationship between the angle of attack and lift coefficient, even if a real vane would start to experience stall. The performance can therefore still be compared.

[2]XFOIL Subsonic Airfoil Development System by M. Drela, H. Youngren, version 6.99 (2000).

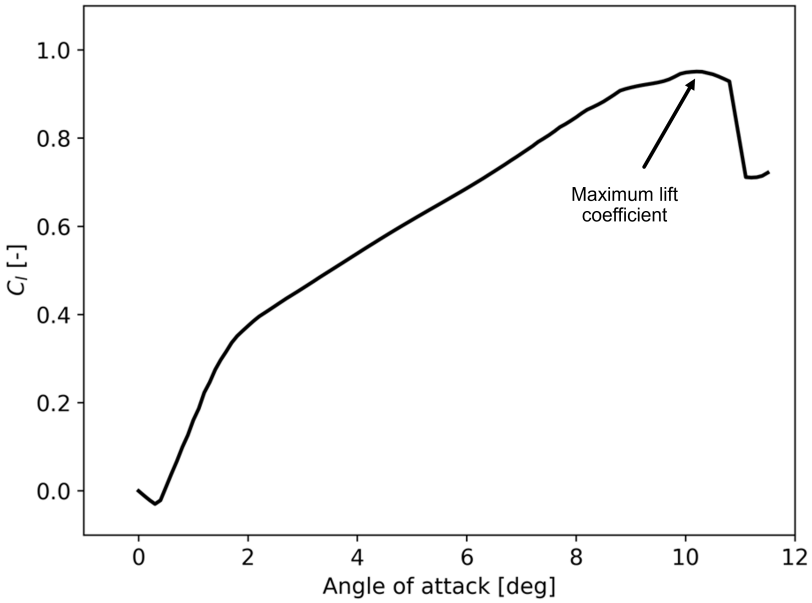

Figure 5.9: *XFOIL NACA 0012 airfoil profile polar plot for angles of attack between* 0 *and* 12° *with* $Re = 7.75 \times 10^4$

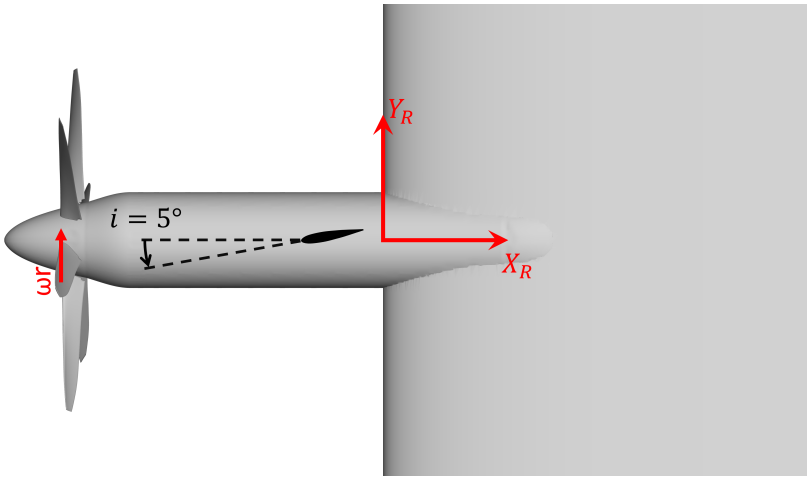

Figure 5.10: *Incidence angle definition on the reference model for SRV placement in top-view*

5.3. Design configurations

The SRV design considerations and incidence angle, as discussed above, result in several design configurations. The configurations that are considered in this thesis research are described in this subsection. There are three main configurations, which are: –0.75 D, –0.25 D and 0.50 D, where the names represent the axial location of the SRVs as discussed in Subsection 5.2.1. The same subsection also discusses the optimal placement based on the force factor integral, which doubles the design configurations from three to six. The surface proximity avoidance setting, as discussed in Section 4.1, is important to compare for each configuration, increasing the number of configurations to analyse to 12. Another configuration that will be considered is the RISE configuration. This configuration is based on the real

RISE engine, which has 12 propeller blades and 10 stationary vanes. For this configuration, five vanes would be placed at the same axial position as the –0.75 D configuration at equiradial positions to represent the same blade-to-vane ratio. A schematic representation of the RISE configuration is presented in Figure 5.11 with indicated vane numbers. This configuration will help gain insight into the additional vane thrust that can be obtained with multiple vanes and possibly show that adding individual vane thrust contributions is a reasonable first estimate approach to determine the overall performance of a multi-vane configuration. The configurations can be seen in Figure 5.12 below, where the SRVs are presented per configuration and, if applicable, optimal placements. The analysis of these initial and optimal SRV placements will be performed individually to compare the differences, but they are presented in the same figure.

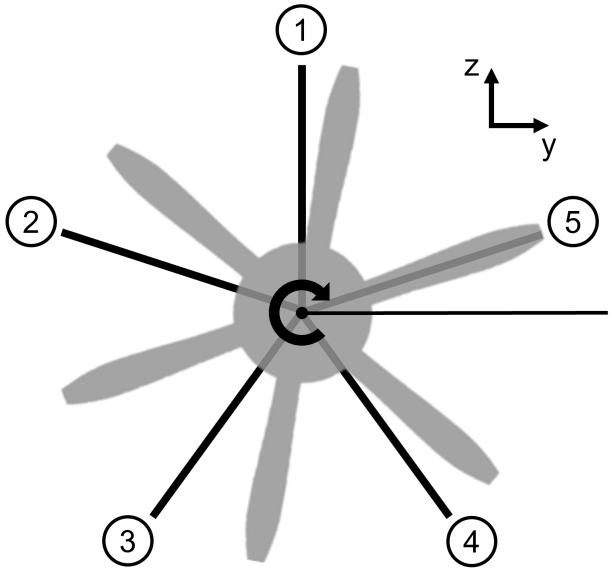

Figure 5.11: *SRV positions for the RISE configuration with vane numbers indicated (rear-view)*

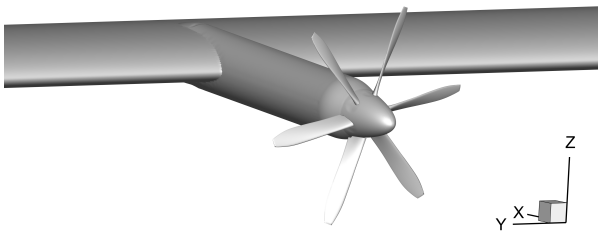

(a) *Reference model geometry for the design configurations*

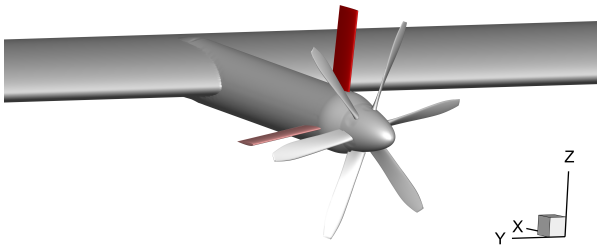

(b) –0.75 D *design configuration with initial (red) and optimal SRV placement (pink) indicated*

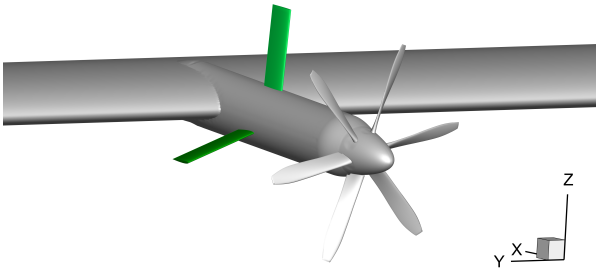

(c) –0.25 D *design configuration with initial SRV placement (green) and optimal SRV placement (dark green) indicated*

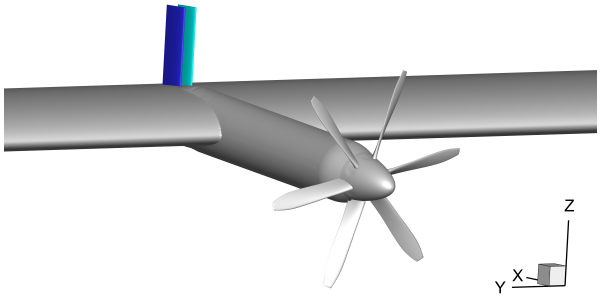

(d) 0.50 D *design configuration with initial SRV placement (blue) and optimal SRV placement (turquoise) indicated*

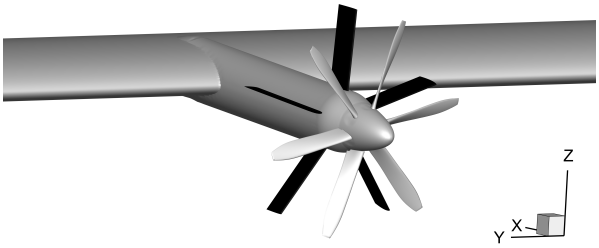

(e) *RISE design configurations with SRVs locations represented with black vanes*

Figure 5.12: *Overview of the design configurations for the initial and optimal SRV placements where applicable for the reference model (a),* –0.75 D *model (b),* –0.25 D *model (c),* 0.50 D *model (d), RISE model (e) configuration*

5.4. Angle of Attack Correction

It is important to consider that the lift coefficient will differ for each design configuration because of the additional vane and interactions with other aerodynamic components. This section discusses the differences in lift coefficient and how this will be taken into account. The total lift coefficients for all previously discussed design configurations are presented in Table 5.5 below. This data allows for a delta C_L to be determined with respect to the reference model for the SPA settings ON and OFF, as seen in the second column in the table. The last column represents the (rounded) angle of attack changes required for constant C_L. These values are based on the lift coefficient slope for the reference model. Separate Flightstream runs were performed for the reference model at an angle of attack of –2 and 2° in addition to the case of zero angle of attack, used for all other analyses. The corresponding lift coefficients

for the different SPA settings can be seen in Figure 5.13, where a linear approximation and corresponding formula are presented. The slopes of these functions were used to determine the required change in angle of attack.

It can be seen in Table 5.5 that the required change in angle of attack is very small based on this first correction estimation. The maximum angle of attack required change would be for the RISE configuration with –0.329°. These corrections are considered to be sufficiently small to neglect an angle of attack correction for the final efficiency comparison.

Table 5.5: *Lift coefficient per configuration and surface proximity avoidance setting with coefficient differences compared to the reference model and corresponding required angle of attack corrections (rounded values)*

Configuration	**SPA**	$\mathbf{C_L}$ [-]	$\Delta\mathbf{C_L}$ [-]	Δ **AoA** [-]
Base model	ON	0.346	-	-
	OFF	0.335	-	-
-0.75D	ON	0.357	0.011	0.145
	OFF	0.335	0.000	0.003
-0.75D opt	ON	0.343	-0.003	-0.036
	OFF	0.335	0.000	0.004
-0.25D	ON	0.355	0.009	0.121
	OFF	0.337	0.002	0.025
-0.25D opt	ON	0.346	0.000	0.002
	OFF	0.335	0.000	-0.001
0.50D	ON	0.363	0.017	0.218
	OFF	0.337	0.002	0.024
0.50D opt	ON	0.363	0.017	0.216
	OFF	0.339	0.004	0.041
RISE	ON	0.320	-0.026	-0.329
	OFF	0.336	0.000	0.005

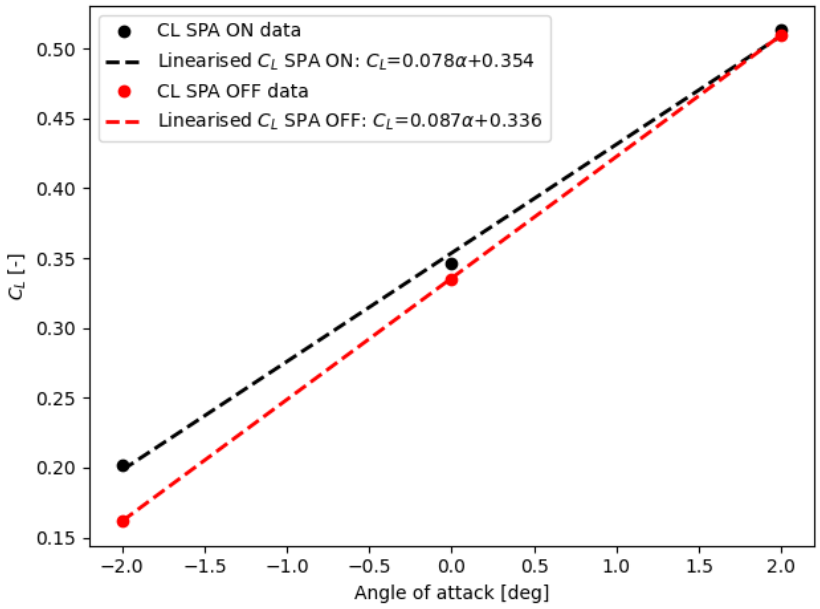

Figure 5.13: *Lift coefficient versus angle of attack graph for the SPA setting ON and OFF with linear regression lines and functions between –2 and 2°*

5.5. Model Modification Conclusions

This section discussed the model modifications made to the reference model of [29]. Three axial vane positions were considered, which all had a defined vertical initial vane and an optimised SRV for vane thrust generation. The latter was based on a newly introduced force factor, which is representative of the thrust generation potential. A fourth design configuration would represent the current RISE engine implementation as given the same name in this thesis research. The vanes are installed at an incidence angle of 5° to prevent vane stall in any particular timestep of the unsteady analysis. This reduces the thrust generation of the blades but allows a positional comparison to be performed. The different design configurations were discussed and presented to indicate the main Flightstream analysis performed. Lastly, the necessity for an angle of attack correction was discussed to keep the model's lift coefficient constant. This correction was concluded not to be necessary as the changes, based on the linear lift slopes of the SPA setting ON and OFF, were very small.

6

Results

This chapter describes the results of the aerodynamic analyses performed during this thesis research. The flow conditions for each SRV and corresponding location are discussed in Section 6.1. The SRV surface pressures and vane thrust contributions are discussed in Section 6.2 and Section 6.3, after which the individual and total propulsive efficiency is discussed in Section 6.4. The limited application of the results is discussed in Section 6.5, followed by a summary of the key findings in Section 6.6.

6.1. SRV Flow Conditions

A first set of valuable information can be found in the SRV inflow conditions. This section describes set inflow conditions for each of the configurations, which will help understand the later thrust and efficiency contributions to the overall model performance. It is important to consider that most of the data presented thus far is based on time-averaged data of one propeller rotation. There are also unsteady effects at play, as shortly discussed in Subsection 5.2.2. It is the unsteady aspect of the simulations that is first elaborated upon in this section. Figure 6.1 shows the timewise variation in angle of attack during one propeller rotation for each of the SRV configurations and SPA setting. This data represents the local angle of attack at a vertical position of 0.7 z/R above the centre of the nacelle for the axial positions of the main configurations. This position was chosen as it allows for a clear comparison between all initial vane locations and would be at the approximate location of maximum tangential velocity, as will be discussed in the remainder of this section.

It can be seen that the average angle of attack, at the selected locations, decreases when moving further away from the propeller. The average local AoA values are highest at –0.75 D for the SPA setting ON and OFF, with maximum values of respectively 13 and 15°. These values reduce to about 7 and 9° at 0.50 D. This is the result of the presence of the wing, which will be discussed in more detail below when considering the average inflow conditions. It can also be observed that the local angles are higher for the SPA setting OFF, which supports the previously made statement in Section 4.1 that the induced velocities are, for this setting. overestimated. These higher velocities cause, in this case, larger tangential velocities and thus a higher local angle of attack.

The periodic behaviour of the angle of attack consists, for both SPA settings, of six blade passages, which is consistent with the total number of blades. The angle of attack variation is more spiky for the SPA setting ON, as the wake in this setting is at several time-steps removed if close to or intersecting with the model. This is not the case for the SPA setting OFF, which displays more consistent variations in the local angle of attack over time.

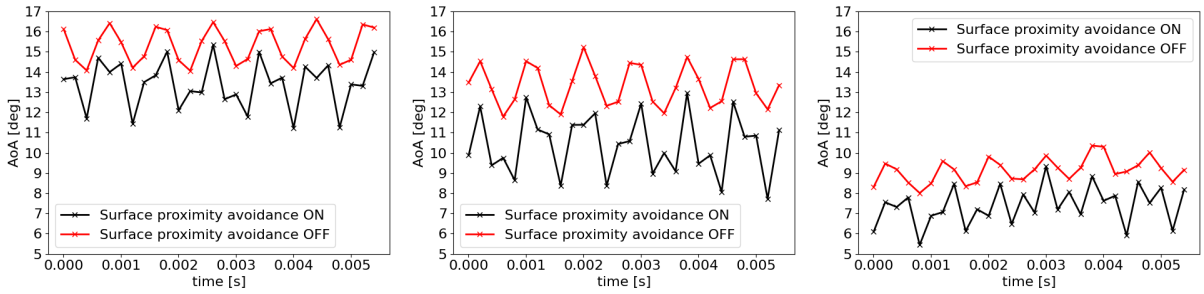

(a) *Angle of attack variation over one propeller rotation located at* 0.7 z/R *on* –0.75 D *analysis plane for SPA setting ON and OFF*

(b) *Angle of attack variation over one propeller rotation located at* 0.7 z/R *on* –0.25 D *analysis plane for SPA setting ON and OFF*

(c) *Angle of attack variation over one propeller rotation located at* 0.7 z/R *on* 0.50 D *analysis plane for SPA setting ON and OFF*

Figure 6.1: *Angle of attack variation for SPA setting ON and OFF for* –0.75 D *(a),* –0.25 D *(b) and* 0.50 D *(c) analysis plane determined at a vertical location of* 0.7 z/R

It was possible to extract the average SRV local axial and tangential inflow conditions for the initial and optimal vane locations based on the analysis plane output files from Flightstream. This data is described below, starting with the axial and tangential inflow conditions at the –0.75 D plane for the initial and optimal SRV placement in Figure 6.2. Figure 6.2a shows the axial velocity data for the initial and optimal SRV positions and both SPA settings. It can be seen that the axial velocity is practically identical for both SPA settings, but that the SRV at the optimal position for thrust experiences a slightly lower axial inflow. This seems counter-intuitive but can be explained by considering the location and tangential inflow conditions as presented in Figure 6.2b. This figure shows that the tangential velocities are higher for the optimal SRV placement cases, meaning that the vane thrust is higher even with a slightly lower axial local inflow velocity. The highest tangential flow velocities for the initial vane location are found at a radial position of ≈0.7 r/R, which is the reason for the chosen time-dependent angle of attack analysis point position as discussed above.

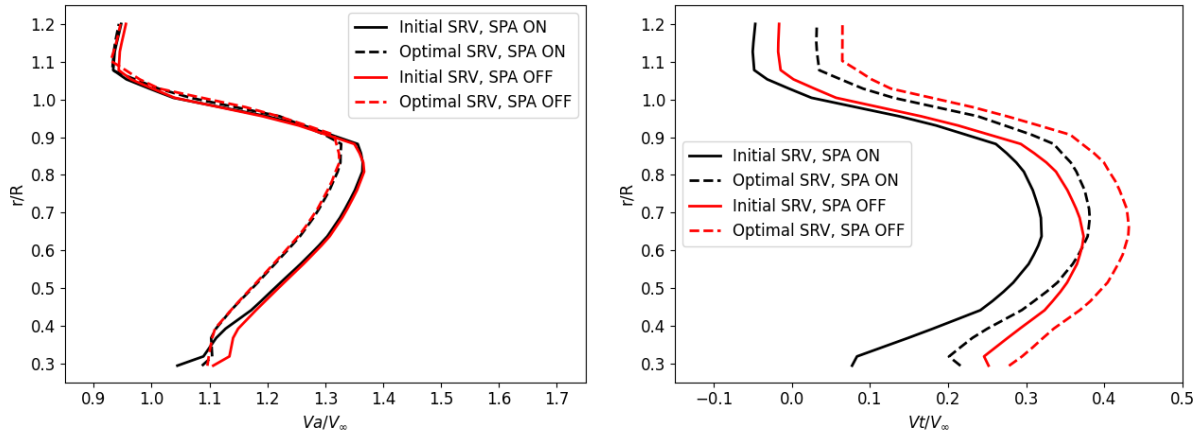

(a) *Axial inflow conditions* –0.75 D *SRV configuration*

(b) *Tangential inflow conditions* –0.75 D *SRV configuration*

Figure 6.2: *Axial (a) and tangential (b) SRV inflow condition comparison for the initial and optimal vane positions at the* –0.75 D *analysis plane for both SPA settings*

The axial and tangential velocity data for the vanes positioned at –0.25 D are presented in Figure 6.3 below. The general trend of the data is the same as for the vanes located at –0.75 D, but a larger difference is observed between the axial velocities. The velocities of the initial vane are affected by the wing, resulting in slightly higher axial velocities due to the upwash of the wing, aligning the flow with the vane orientation. The vane at the optimal position is located on the blade downward-going side, which experiences a lower local axial velocity compared to the initial vane placement. This is because the vane is positioned on the nacelle at an angle of –5° to the free stream velocity, which reduces the axial flow aligned with the vane. The tangential velocity for this plane is higher, meaning that the overall thrust potential, based on the force factor parameter, is higher for this vane location.

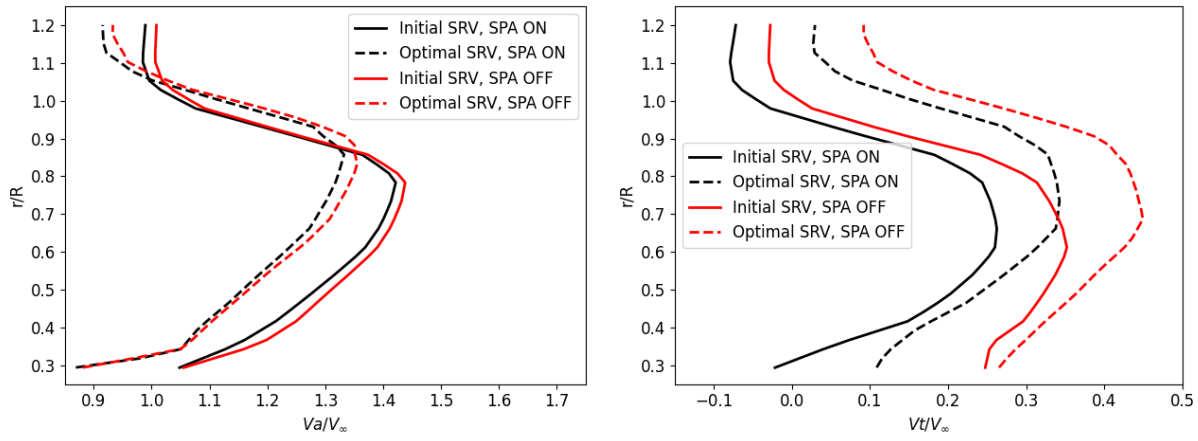

(a) *Axial inflow conditions* –0.25 D *SRV configuration*

(b) *Tangential inflow conditions* –0.25 D *SRV configuration*

Figure 6.3: *Axial (a) and tangential (b) SRV inflow condition comparison for the initial and optimal vane positions at the* –0.25 D *analysis plane for both SPA settings*

The last SRV analysis plane is located on the wing at 0.50 D, of which the axial and tangential data plots are presented in Figure 6.4. The axial velocity is higher for this location than for the previous two positions, as the flow over the wing's upper surface is accelerated. The tangential velocities can be seen to be lower, which suggests that the vane thrust potential at this location is limited. The small variation in axial and tangential velocities also indicates that the initially chosen vane location performs fairly similarly to the optimal vane location.

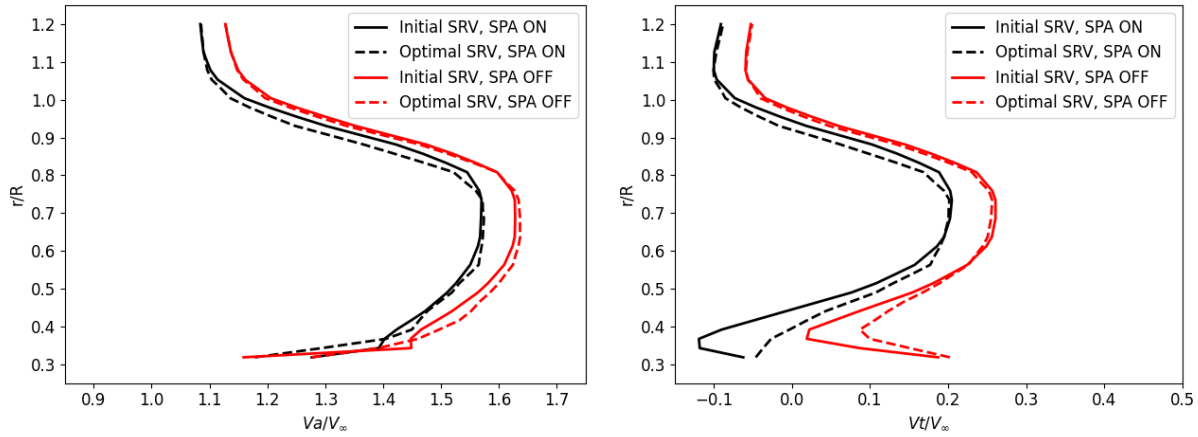

(a) *Axial inflow conditions* 0.50 D *SRV configuration*

(b) *Tangential inflow conditions* 0.50 D *SRV configuration*

Figure 6.4: *Axial (a) and tangential (b) SRV inflow condition comparison for the initial and optimal vane positions at the* 0.50 D *analysis plane for both SPA settings*

6.2. Vane Surface Pressure Coefficients

The inflow conditions, as presented in the previous section, result in different surface pressure distributions on the vane's surface. This section describes the pressure distributions of the different vanes at the time instance after the convergence iterations. The data is thus only valid for this particular time instance where the pressure data was recorded. It should also be noted that the surface pressure is a result of the local velocity, which is affected by the propeller swirl and the presence of aerodynamic surfaces.

Figure 6.5 shows the surface pressure data for the SPA setting ON for both the pressure and suction side of the vane. It can be seen that the pressures on the pressure side of the −0.75 and −0.25 D vanes (Figure 6.5a) are less negative compared to the pressures on the suction side of the vane (Figure 6.5b). This pressure difference, combined with the inflow and incidence angle as defined in Figure 5.10, would result in a positive vane thrust for these vanes.

The surface pressures of the vane located on the wing (0.50 D) are more negative than what would be expected on the pressure side of the vane. Several reasons, related to the inflow conditions and vane placement, could cause this observed lower pressure. Firstly, the presence of the wing causes higher velocities on the upper surface of the wing. A similar local swirl velocity with a higher axial velocity component results in a higher dynamic pressure but at a lower angle of attack. This effect can also be seen in Figure 6.4, where V_a is higher and V_t is lower compared to the other configurations. The vane positioning at an incidence angle of 5° reduces the local angle of attack of the vane, resulting in an even lower angle of attack. This explains the lower pressure on the pressure side of the vane. It could be considered to select a different incidence angle for this particular vane to ensure a positive vane thrust contribution, but this would result in an unfair comparison. The pressure difference and resultant vane thrust will speak to the swirl recovery potential of a vane positioned on the wing, which is what this thesis research aims to determine. It is expected that, based on the pressure plots, both vanes on the nacelle will generate a positive and the vane positioned on the wing a negative thrust component, which will be discussed in the next section.

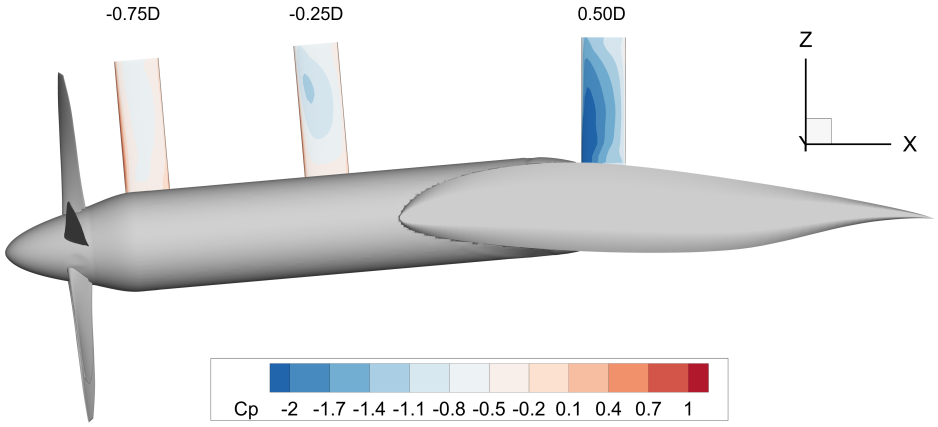

(a) *Initial vane pressure coefficients contours for SPA setting ON, on the vane's pressure side*

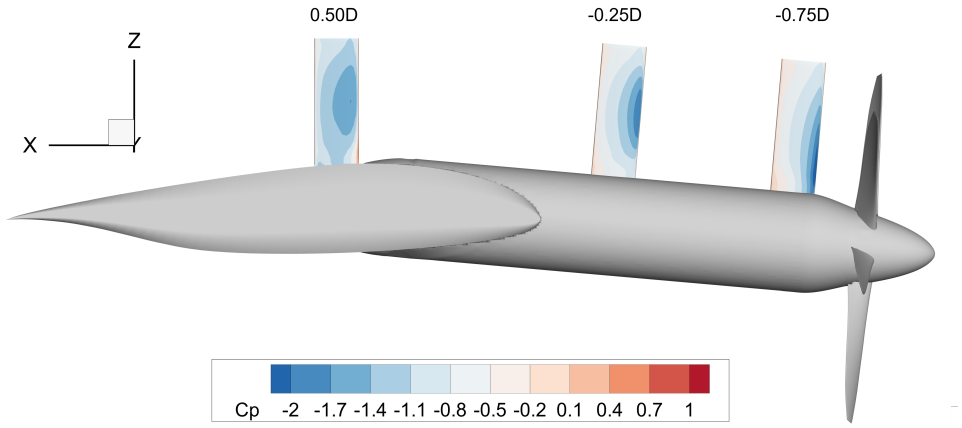

(b) *Initial vane pressure coefficients contours for SPA setting ON, on the vane's suction side*

Figure 6.5: *Surface pressure coefficient for all initial vanes with SPA setting ON after model convergence for pressure (a) and suction side (b)*

Figure 6.6 shows the surface pressure distributions for the analysis runs with the SPA setting OFF. The surface pressures follow the same trend as seen in the analysis performed with the SPA setting ON, but with more negative pressures. This is because of the differences as discussed in Section 4.1, where the induced velocities for the SPA setting OFF analysis are higher. Higher total velocities result in lower pressures with the formula for C_p as used in Flightstream, which was discussed in Subsection 4.5.1.

The instantaneous data after the model convergence iterations also clearly show the effect of not removing the propeller wake when intersecting with the vane. The –0.75 D vane location has a low-pressure region near the vane tip, which is the result of the wake going through the vane. This is not the case when the SPA setting is turned ON, as confirmed by the lack of this lower pressure region in the previous figures. The SPA setting OFF thus creates unrealistic flow behaviour at individual timesteps.

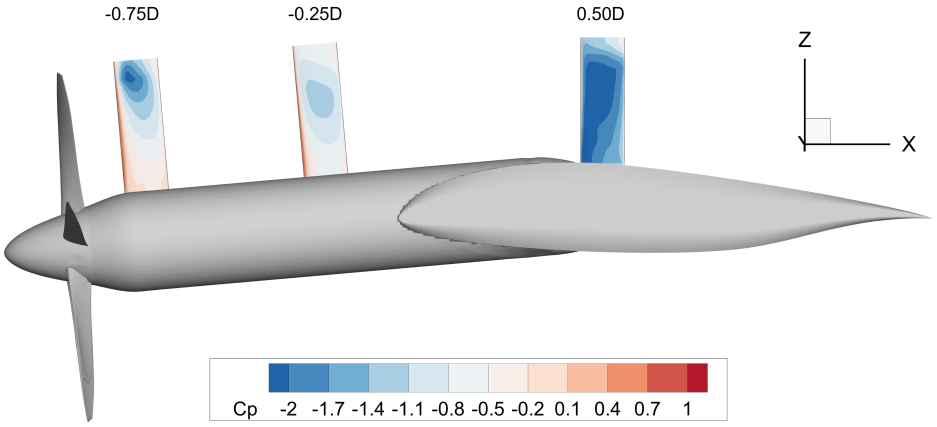

(a) *Initial vane pressure coefficients contours for SPA setting OFF, on the vane's pressure side*

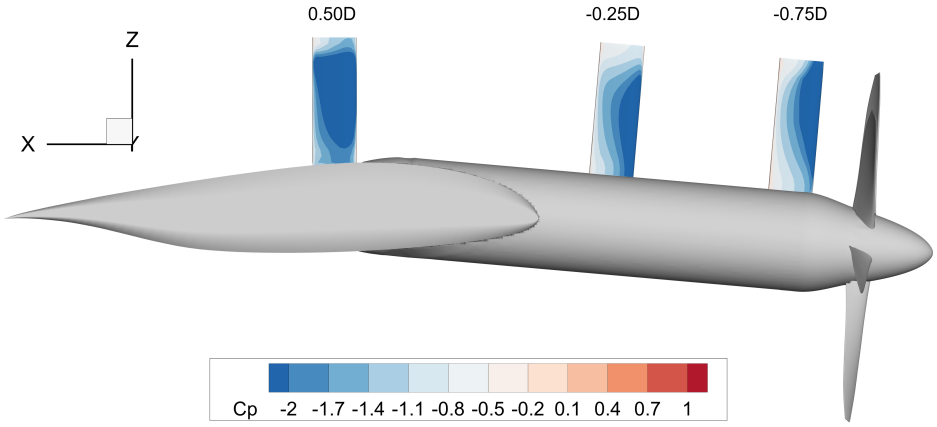

(b) *Initial vane pressure coefficients contours for SPA setting OFF, on the vane's suction side*

Figure 6.6: *Surface pressure coefficient for all initial vanes with SPA setting OFF after model convergence for pressure (a) and suction side (b)*

6.3. Vane Thrust

The SRV axial thrust, as a percentage of the propeller thrust force for each configuration and SPA setting, can be seen in Figure 6.7. The third bar of each configuration represents the average value of the SPA setting ON and OFF, as it is expected that the real wake behaviour is between these two extremes of wake handling.

There is a general trend visible between the vane thrust of the initial and optimal placement, where the vane thrust is higher for the optimal SRV placements. The only configuration and setting different from this trend is the –0.75 D SPA setting OFF configuration. The vane thrust is, for these specific conditions, higher for the initial vane placement than the optimised location. The exact aerodynamic cause for this difference and deviation from the expected behaviour is unclear, but a first hypothesis is that the unpredictable nature of the SPA setting OFF close to the model geometry causes local unrealistic flow behaviour, resulting in this higher vane thrust.

The vane thrust values for the 0.50 D configuration can be seen to be negative for both the initial and optimal positions, as previously predicted based on the vane surface pressures in Section 6.2. The force factor plot for this plane, as presented in Figure 5.6c, also showed that the vane thrust potential for this location was lower compared to the other axial positions. This was the result of the swirl recovery of the main wing and thus relatively low swirl velocities.

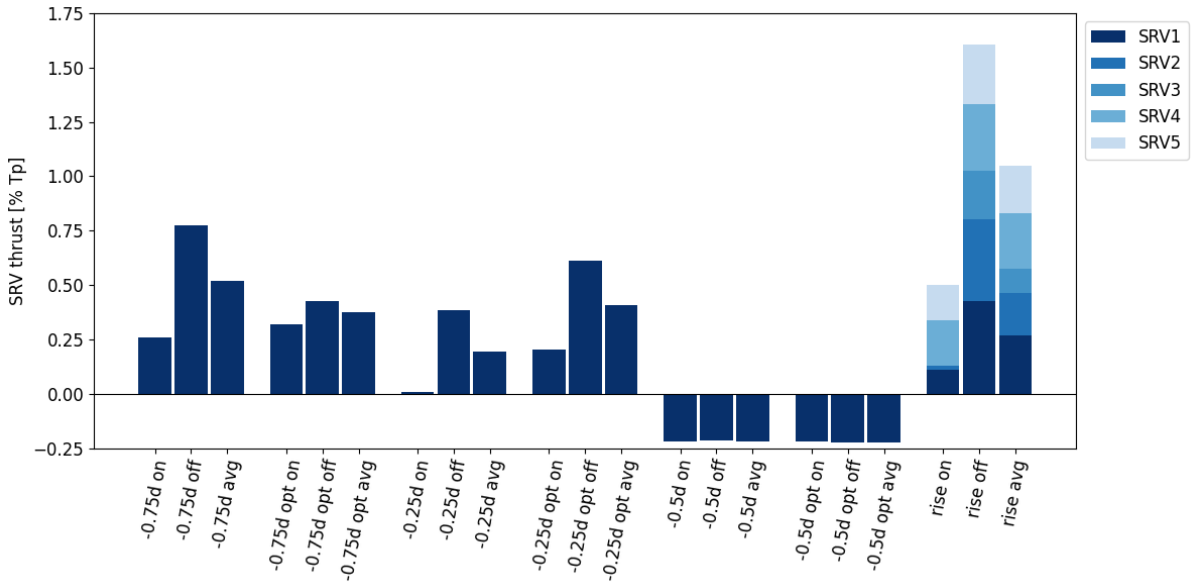

Figure 6.7: *Vane thrust bar graph for all analysed vane configurations as a percentage of the propeller thrust, for both SPA settings and averaged performance*

The last three bars in Figure 6.7 represent the RISE configuration with five vanes. The SRV numbers in the legend correspond with the earlier mentioned vane numbers in Figure 5.11. The added vanes cause more complex flow interactions, which, as a whole, result in the vane thrust contributions as shown in the bar graph. The axial positioning of the vanes in the RISE configuration is the same as for –0.75 D, meaning that the vertical (initial) vane can be compared to vane number 1. The vane thrust for the initial vane is lower for the RISE configuration compared to the same vane location in the –0.75 D configuration. A possible reason for this is the more complex interaction effects in the RISE configuration, but this can not be stated with complete certainty. It should be noted that the vane thrust contribution of several vanes of the RISE configuration with the SPA setting ON analysis is extremely small, which could, similarly to the difference in thrust, be the result of flow interactions. The difference in thrust also suggests that it is not possible to superimpose the vane thrust contributions of several individually analysed vanes to determine the combined total effect. A second indication for this can be found in the force factor contour plots, which change when a vane is placed. Figure 6.8 shows the force factor contour plots for the SPA setting ON case at –0.25 D in case no vanes are placed on the reference model (Figure 6.8a) and the contour plot at the same location with a vane placed upstream at –0.75 D (Figure 6.8b). The thrust potential in the second plot is greatly reduced due to the presence of an SRV upstream of this analysis plane. The total thrust performance and overall performance of a certain combination of vanes should thus be analysed in their entirety.

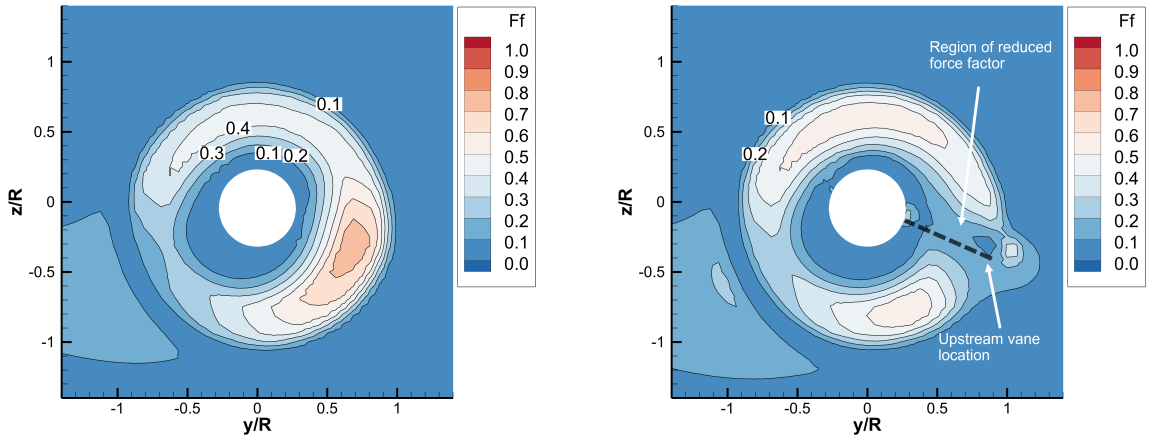

(a) –0.25 D *force factor contour plot for reference model geometry* **(b)** –0.25 D *force factor contour plot with upstream vane at* –0.75 D

Figure 6.8: *Force factor contour plots for reference model (a), and* –0.75 D *configuration (b)*

6.4. Axial Propulsive Efficiency

The objective of this thesis research is to improve the total axial propulsive efficiency by strategically placing SRVs. This section discusses the axial propulsive efficiency for each aerodynamic component and the total efficiency per configuration. Subsection 6.4.1 starts by describing the individual contributions of the aerodynamic surfaces and how differences in these contributions can be explained. Subsection 6.4.2 continues by describing the configurations' total axial propulsive efficiency and comparing this to the reference model.

6.4.1. Component Efficiency

The overall propulsive efficiency is the combined effect of all aerodynamic components of the model. The different SRV thrust contributions have been discussed in Section 6.3, which is representative of the relative efficiency contribution. The other model components are discussed below in a similar manner to the vane thrust, but in the context of axial propulsive efficiency, introduced in Section 3.3. The values as determined by Flightstream are presented for each configuration and SPA setting. This gives a clear overview of the axial propulsive efficiency contribution differences between the model components.

Propeller

The first aerodynamic surface that interacts with the free stream is the propeller. The propeller is the thrust-producing element of the model and therefore has the largest contribution to the overall efficiency. The different propeller contributions for the configurations and SPA settings can be seen in the bar graph as presented in Figure 6.9. Each third bar presents the average contribution of the SPA setting ON and OFF, which was also done for the SRV thrust comparison.

It can be seen that the overall propeller axial efficiency is similar for all configurations. There are, however, some differences visible between the reference model and especially the –0.75 D and –0.75 D opt configuration, where opt refers to the optimal vane placement discussed in the previous chapter. These configurations have the vane placed directly behind the propeller, which affects the inflow conditions and, consequently, the propeller's performance.

The relation between the propeller advance ratio and propulsive efficiency, as discussed in Subsection 2.2.3, helps to understand these differences. A vane placed in the slipstream of the propeller, and especially, in close proximity to the propeller, will affect the inflow conditions of the propeller. It is difficult to specify the exact origin of the differences, but a local change in the apparent advance ratio is most likely a reason for the performance differences observed.

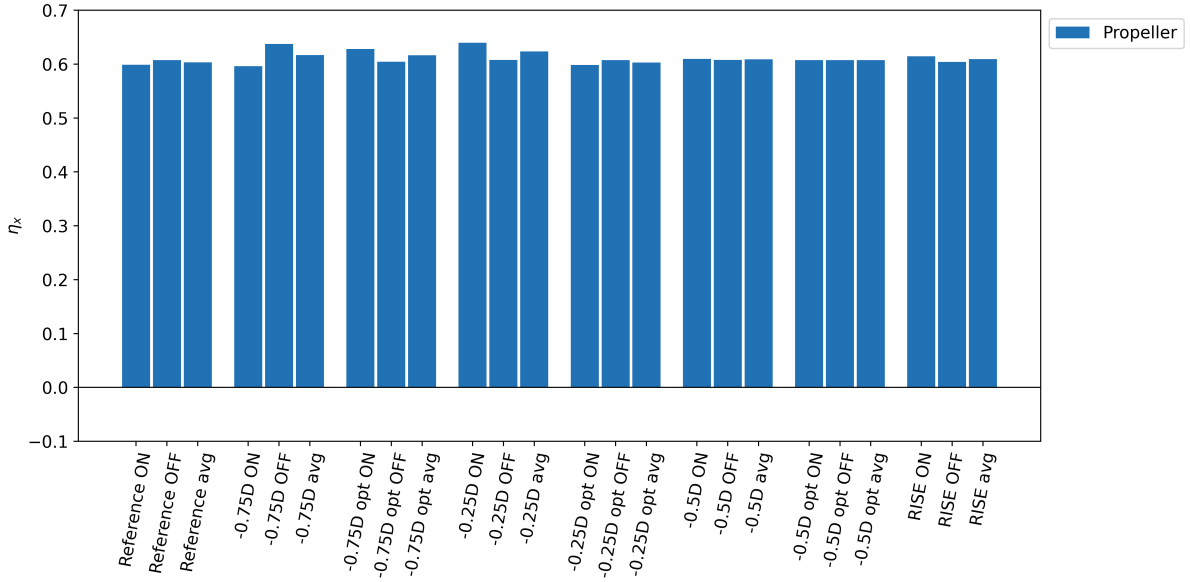

Figure 6.9: *Propeller axial propulsive efficiency bar graph for the different configurations and SPA settings*

Nacelle

The second model element is the nacelle, which connects the propeller to the wing. The axial thrust contributions of the nacelle can be seen in the bar graph as presented in Figure 6.10. A first observation of this graph is that the contribution is extremely small and that the SPA setting causes the sign of the contribution to change. The small contributions of the nacelle are unexpected, as the nacelle would normally only add to the model drag, since it is not a lifting body. These results can be explained by considering how the reference model is set up and how Flightstream determines the forces acting on each body.

Flightstream determines the forces acting on a body by integrating the pressure distribution of each body separately. Figure 6.11 shows the pressure distribution of the upper and lower surface near the nacelle for the SPA setting ON (Figure 6.11a) and OFF (Figure 6.11b). The nacelle is partly integrated into the wings' upper and lower surfaces, which causes the pressure coefficient of the nacelle to be greatly affected by the wing. The similar pressure coefficients of the upper and lower surfaces explain the small contributions to the overall performance. It can also be seen that the pressure coefficients on the upper surface are slightly more negative when the SPA setting is turned OFF compared to when this setting is turned ON. This increases the lift force of the nacelle in the SPA setting OFF case slightly, which positively contributes to the axial efficiency of the nacelle. This is because the nacelle is placed at a relative angle of –5° to the wing and free stream velocity.

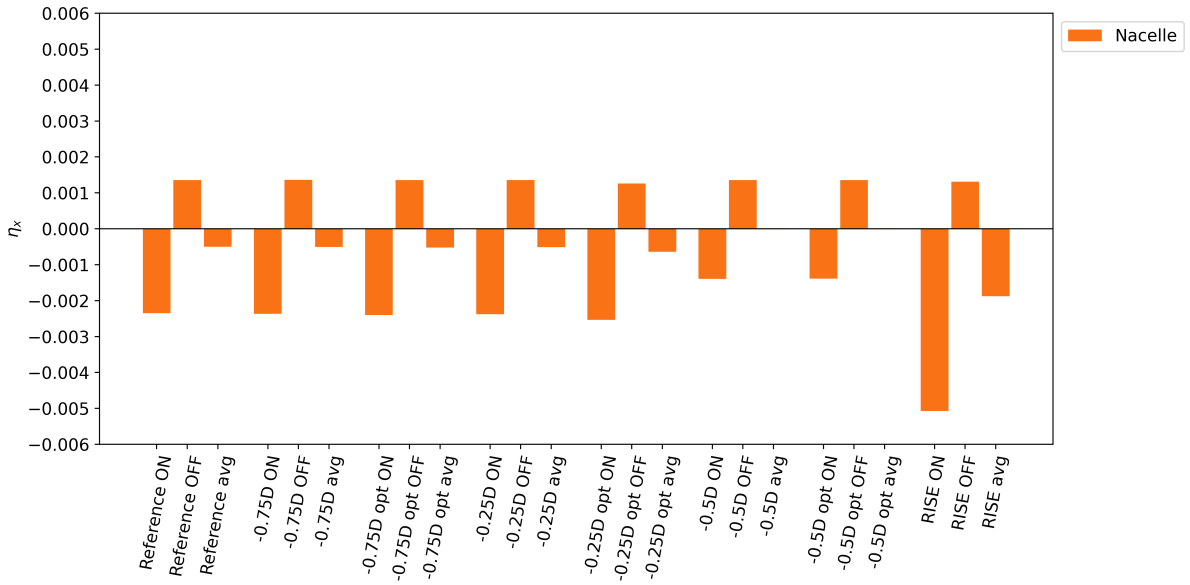

Figure 6.10: *Nacelle axial propulsive efficiency bar graph for the different configurations and SPA settings*

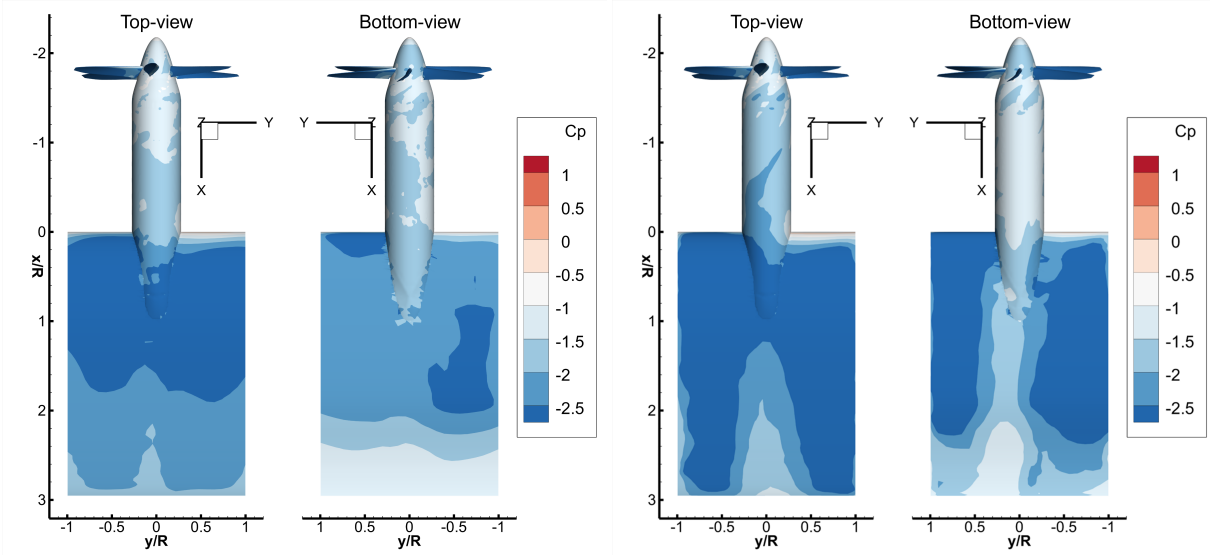

(a) *Top- and bottom-view of the average surface pressure coefficient values with the SPA setting ON*

(b) *Top- and bottom-view of the average surface pressure coefficient values with the SPA setting OFF*

Figure 6.11: *Average surface pressure coefficient of the reference model geometry for analysis with the SPA setting ON (a) and OFF (b)*

Wing

The axial efficiency contribution of the wing can be seen in Figure 6.12. The integrated pressures of the wing result in a larger negative contribution compared to the nacelle, as is expected because of the large surface area of the wing. Most contributions of the wing are similar, but some discrepancies are visible. The main reason for this is that the SRVs affect the airflow around or on the wing.

The largest difference between the wings' axial propulsive efficiency contribution is visible when a vane is placed at –0.25 D and analysed with the SPA setting ON. The axial efficiency contribution of the wing in this configuration is less negative compared to the other configurations. The exact origin of this difference is difficult to define as a number of flow interactions occur between the propeller, nacelle, wing and SRV. Figure 6.13 shows the spanwise lift distribution of the reference model and SRV –0.25 D configuration with the SPA setting ON. The modified configuration produces slightly more lift on the blade upwards-going side (negative y), which marginally increases the axial efficiency of the wing, resulting in a less negative contribution to the overall performance. One could argue that an angle of attack correction is needed based on these findings to keep the comparison between the different configurations fair. This was, however, determined not to be necessary due to the small total differences in lift coefficient, discussed Section 5.4.

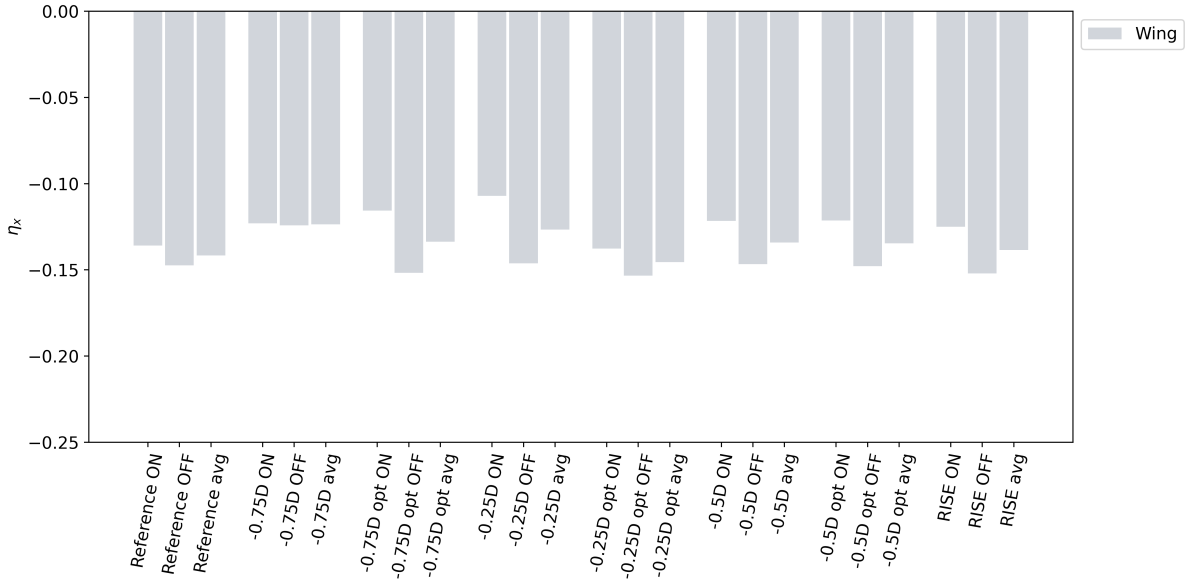

Figure 6.12: *Wing axial propulsive efficiency bar graph for the different configurations and SPA settings*

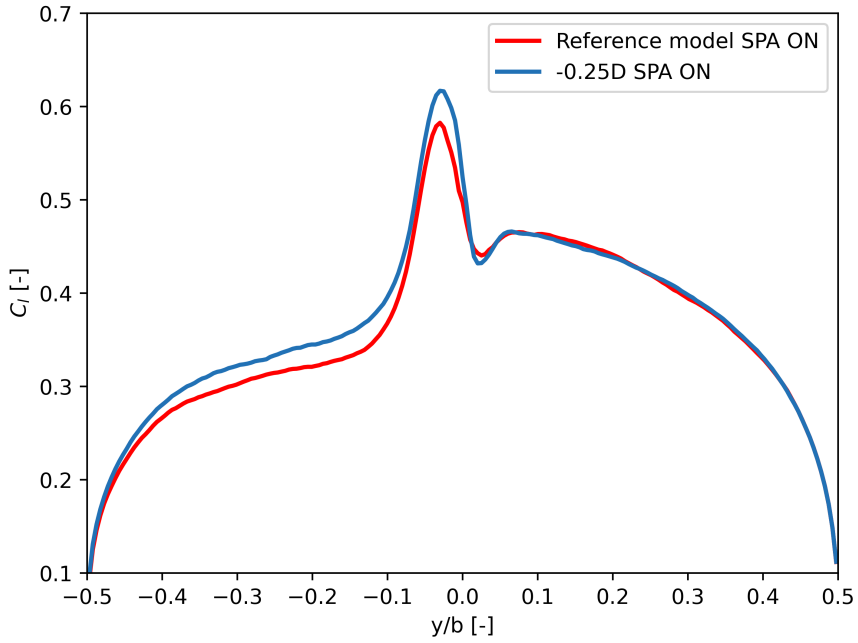

Figure 6.13: *Spanwise lift coefficient comparison between the reference model and* –0.25 D *configuration, both analysis with the SPA setting ON*

6.4.2. Total axial Efficiency

The combined individual axial propulsive efficiency components result in an overall efficiency for the configuration and corresponding SPA setting. The following paragraphs describe the total axial efficiency of the configurations with respect to the reference model based on the formula as presented in Section 3.3. An overview figure and table of these configurations will be presented at the end of this subsection.

Reference Model

The total efficiency of the reference model can be seen in Figure 6.14 below. This model consists of the propeller, nacelle and wing. The nacelle contribution, as described in the previous subsection, is very small compared to the other aerodynamic surfaces, meaning that these contributions are barely visible in this graph. The bar plots in this section will give insight into the overall performance instead of the specific contributions mentioned above. The first two bars represent, respectively, the SPA setting ON and OFF. The third bar represents the average of both SPA settings for the same reason as described in Section 6.3. The overall efficiency is represented by the black horizontal line, which for the reference model is for all bars equal to 0.461. All other configurations in this subsection will be compared to this reference model.

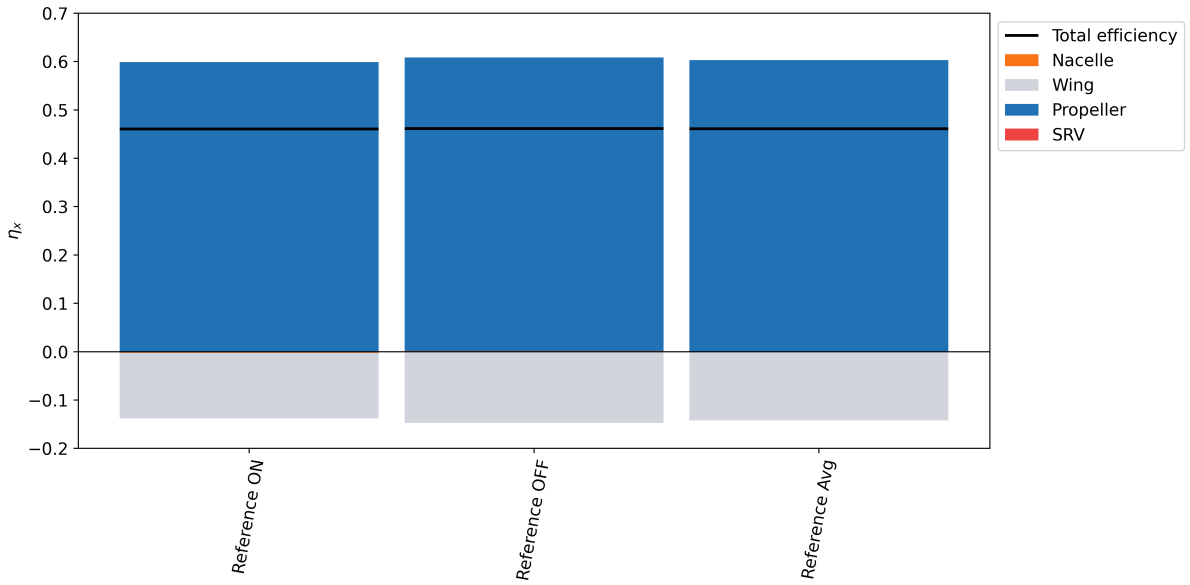

Figure 6.14: *Propulsive efficiency bar graph for reference model, representing all model components and contributions with the total axial efficiency presented by a black line*

–0.75 D Configuration

The first configuration is the –0.75 D configuration, with an additional vane placed directly behind the propeller. The overall axial propulsive efficiency of the initial vane and optimal vane position compared to the reference model can be seen in Figure 6.15 below. The propeller efficiency can be seen to have increased with the addition of a vane, as discussed in the previous subsection. A noticeable difference between the bars in this plot is that the SRV component for the –0.75 D SPA setting ON configuration is larger compared to the other configurations. This was already addressed in Section 6.3, but can not definitively be explained by the observed aerodynamic effects and available data. The average efficiency increases for both vane positions, the values of which will be presented later.

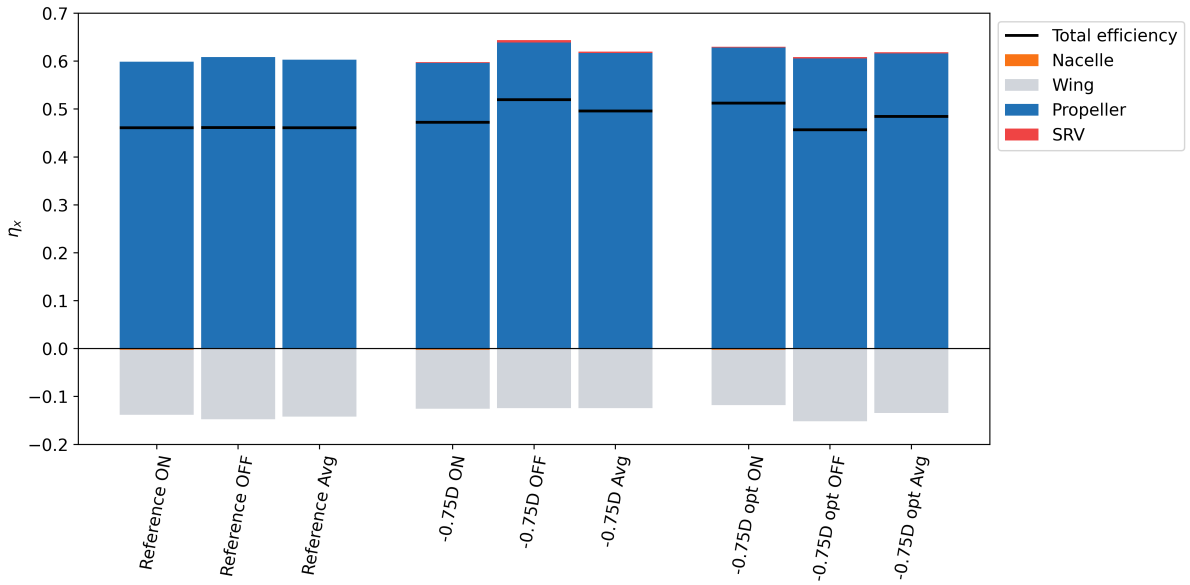

Figure 6.15: *Propulsive efficiency bar graph for SRV placement at* –0.75 D*, representing all model components and contributions with the total axial efficiency presented by a black line*

–0.25 D Configuration

A similar bar graph as for the –0.75 D configuration is presented for the –0.25 D configuration in Figure 6.16. The vane contribution is larger for optimal SRV location in this configuration for all cases, which corresponds with the vane thrust values presented. The wing contribution for the –0.25 D SPA setting ON is less negative compared to the others, which was also addressed in the previous subsection. It can be seen that the average propulsive efficiency is higher for the initial vane placement, but that the optimised vane is approximately equal to the reference model.

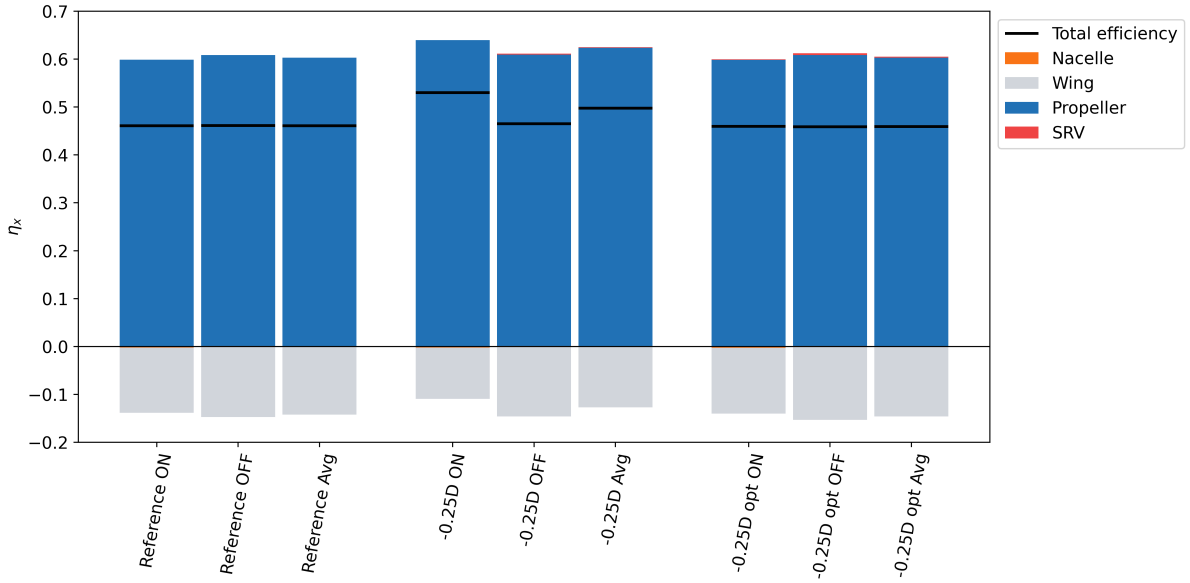

Figure 6.16: *Propulsive efficiency bar graph for SRV placement at* –0.25 D*, representing all model components and contributions with the total axial efficiency presented by a black line*

0.50 D Configuration

The 0.50 D configuration has an SRV placed on the wing's upper surface instead of on the nacelle. The results for this configuration are presented in Figure 6.17 and show a clear difference with the first two SRV locations. The vane contribution is negative for both the initial and optimal SRV placement. This was expected with the previously discussed vane surface pressure data and vane thrust, but it does not mean that the overall efficiency is lower. The interaction between the vane resulted in a less negative contribution, which will affect the overall propulsive efficiency, as will be addressed in the next subsection.

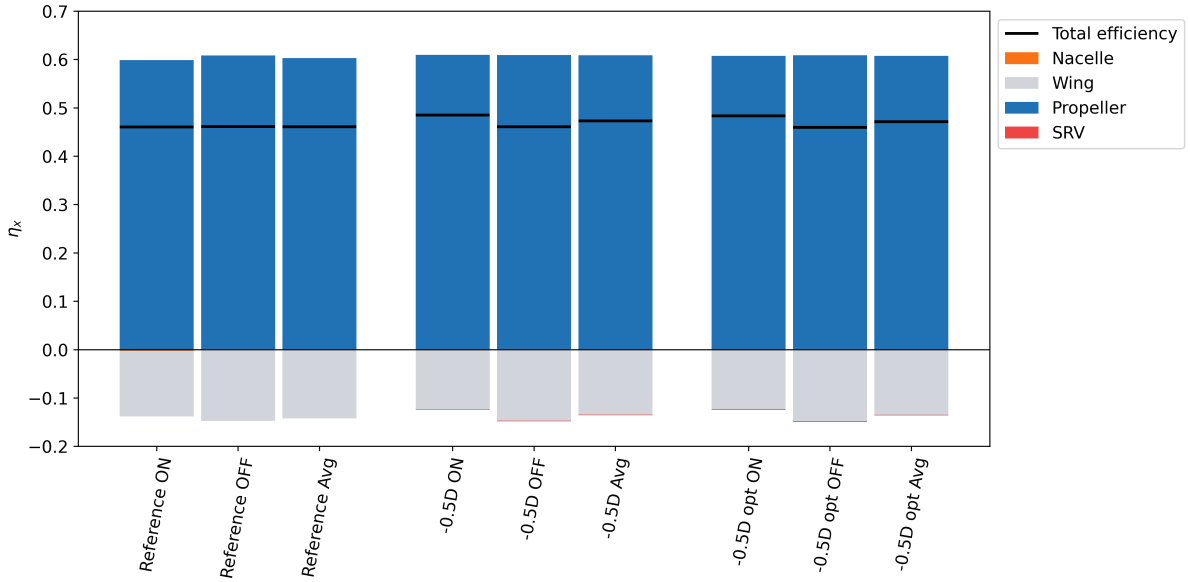

Figure 6.17: *Propulsive efficiency bar graph for SRV placement at* 0.50 D*, representing all model components and contributions with the total axial efficiency presented by a black line*

RISE Configuration

The last configuration is the RISE configuration, of which the results are presented in Figure 6.18. This configuration has a total of five SRVs placed on the nacelle at the same axial location as the –0.75 D configuration. The vane contribution to the overall efficiency is much larger as a result of these additional vanes. The overall efficiency comparison with the other components will be discussed below, as the bar graphs themselves can only provide limited insight into the overall performance.

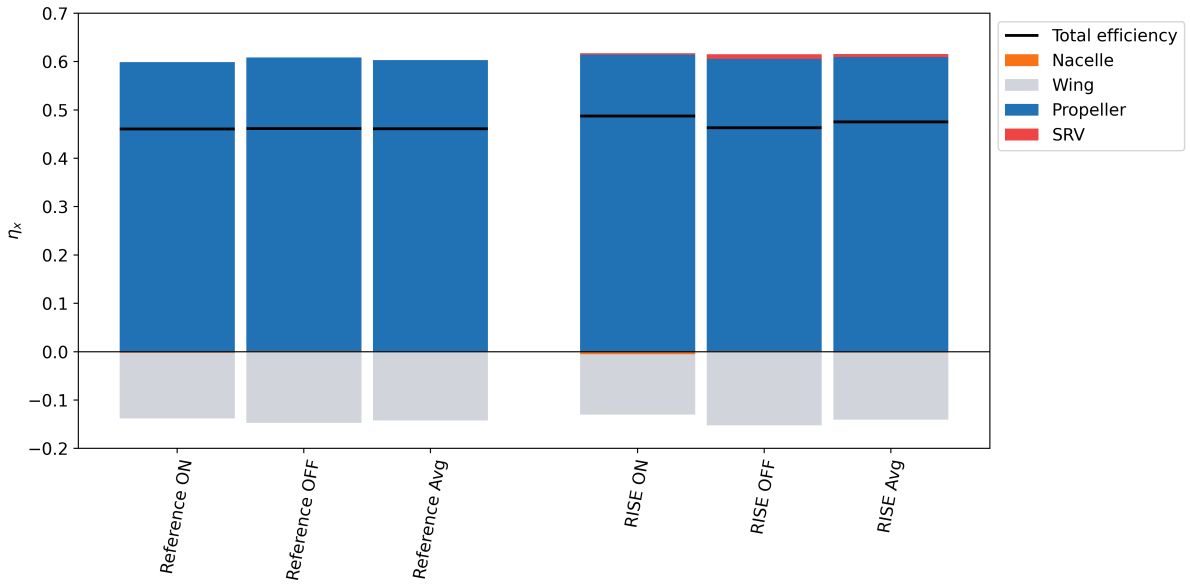

Figure 6.18: *Propulsive efficiency bar graph for the RISE configuration, representing all model components and contributions with the total axial efficiency presented by a black line*

Total Axial Configuration Propulsive Efficiency

The overall axial propulsive efficiencies, as presented by the black horizontal lines in the previously presented bar graphs, were difficult to compare in the bar graphs themselves, which is why the values are presented in Table 6.1 below. In this table, the total propulsive axial efficiency for each configuration and SPA setting is presented, as well as the average value for the SPA settings. The last column shows the percentage difference between the configuration and the reference model, which has a total axial propulsive efficiency of 0.461 for both the SPA setting ON and OFF.

The –0.75 D configuration has an average efficiency of 0.499, which is higher compared to the reference model, meaning that the placement of an additional vane at this location is beneficial for the overall performance under specified conditions. The optimal vane position at the same axial position results in an average efficiency of 0.487, which is slightly lower than the initial vane positioning. A reason for this difference could be the observed larger propeller and SRV contribution of the –0.75 D configuration, as previously discussed in the individual contributions.

The –0.25 D configuration, with the vane placed between the propeller and wings' leading edge, has an average efficiency of 0.499, similar to the –0.75 D configuration. This relatively high efficiency is the result of the less negative wing contribution for this configuration with the SPA setting ON. The propulsive efficiency is lower for the optimised vane thrust location compared to the initial vane location. This could be because of the SRV and wing interaction, reducing the negative contribution of the wing for the initial vane placement.

The optimal SRV location for this axial position is lower compared to the initial vertical vane, which could be because of the SRV and wing interaction, which reduced the negative contribution of the wing for the initial vane placement.

The SRV located at 0.50 D shows, with an average total efficiency of 0.470, that the results are similar to the reference model. An observant reader might find this surprising, as the individual vane contribution of the SRV for this axial location was found to be negative. The interaction effects with the other aerodynamic components, however, increase the axial propulsive efficiency, resulting in an overall slightly increased total efficiency.

The RISE configuration was tested to see how the current implementation of this SRV "ring" approach compares to the strategic placement of a single SRV. The overall total averaged efficiency for this configuration is 0.477, which is higher than the reference model, but does not exceed the total axial efficiency of all configurations with a singular vane. This is a significant observation as it suggests that multiple vanes do not necessarily result in a better axial propulsive efficiency.

Table 6.1: *Total axial propulsive efficiency per configuration and surface proximity avoidance setting with average value per configuration*

Configuration	**SPA**	$\eta_{\mathbf{x,tot}}$ [-]	$\eta_{\mathbf{x,avg}}$ [-]	$\Delta\eta_{\mathbf{x}}$ [%]
Base model	ON	0.461	0.461	-
	OFF	0.461		
-0.75D	ON	0.474	0.499	3.82
	OFF	0.524		
-0.75D opt	ON	0.514	0.487	2.57
	OFF	0.459		
-0.25D	ON	0.530	0.499	3.79
	OFF	0.468		
-0.25D opt	ON	0.461	0.462	0.06
	OFF	0.463		
0.50D	ON	0.484	0.472	1.09
	OFF	0.460		
0.50D opt	ON	0.482	0.470	0.92
	OFF	0.458		
RISE	ON	0.488	0.477	1.59
	OFF	0.466		

The averaged total propulsive efficiency results, as presented in Table 6.1, can be seen in Figure 6.19 below. Figure 6.19a and Figure 6.19b visually show the efficiency results for the initial and optimal SRV configurations. The RISE configuration is presented in the same figure as the optimal SRV configurations because the perspective of this figure allows for a better representation of the vanes of the RISE configuration.

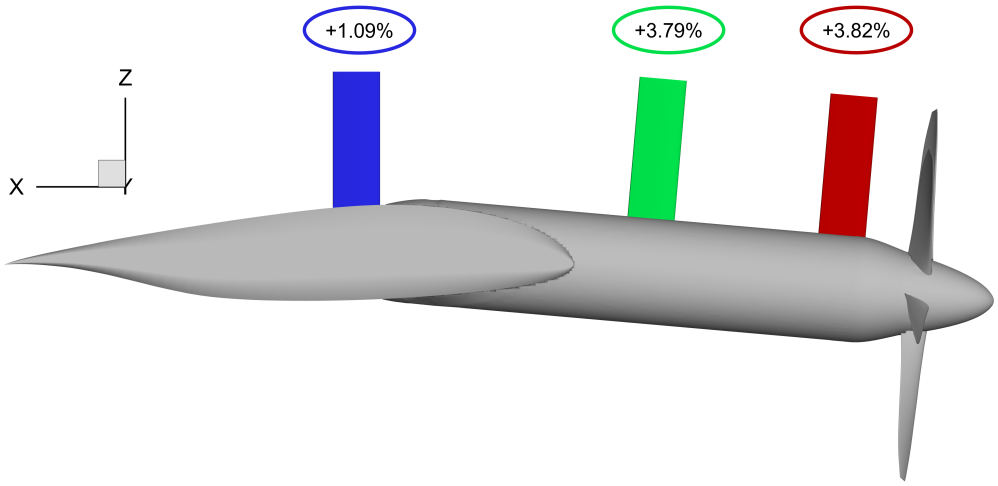

(a) *Total average axial propulsive efficiency difference for initial vane placement*

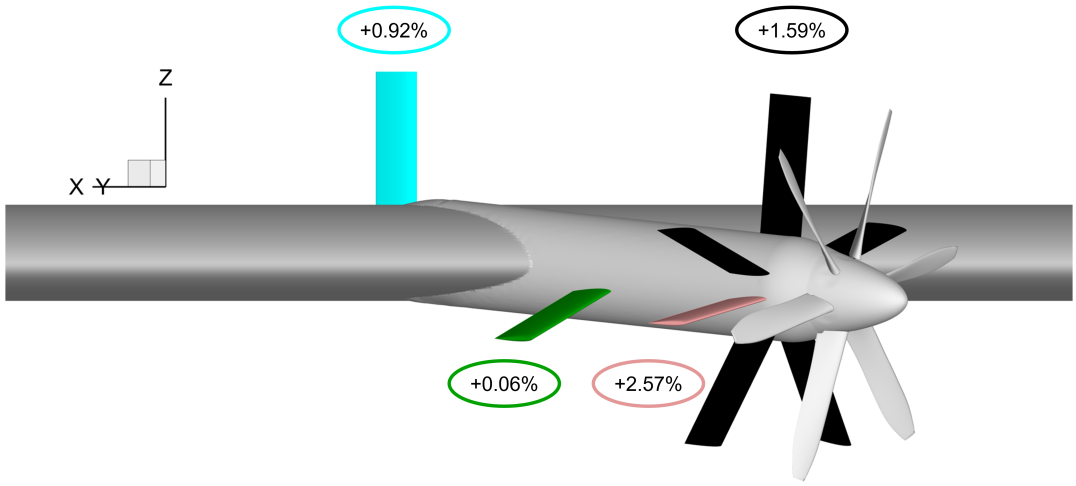

(b) *Total average axial propulsive efficiency difference for optimal vane placement and RISE configuration*

Figure 6.19: *Total average axial propulsive efficiency difference for the initial (a) and optimal / RISE (b) vane locations*

6.5. Limitations

The results presented in this chapter are based on specific model configurations and flow conditions, which were determined with a particular solver. Each of these aspects would influence the results of this study. The limitations should therefore be considered before drawing conclusions. The various aspect limitations are discussed below.

Geometric Model

The reference model used in this thesis research is based on the geometry used by Duivenvoorden et al. [29]. This geometry was described in Section 3.1 and has a nacelle positioned with a relative angle of –5° to the wing. This relative angle to the free stream velocity affects the inflow conditions of the vanes placed on the nacelle. On the blade downwards-going side, the propeller swirl is downwards (negative z-direction) and upwards on the blade upwards-going side. The free stream velocity is uniform, which will have an opposite effect on the local inflow velocity in the reference system of the vane. The free stream velocity will,

on the blade upwards-going side, reduce the tangential velocity. The opposite is true for the blade downwards-going side, where the tangential velocity and free stream velocity are both oriented in the same direction with respect to the vane. Figure 6.20 shows a schematic representation of this difference. The velocity components in this figure show a larger relative inflow angle on the blade downwards-going side, which is in agreement with the optimal SRV locations found. The optimal vane location is thus affected by the model geometry, suggesting that the results of this research are only valid for this particular model.

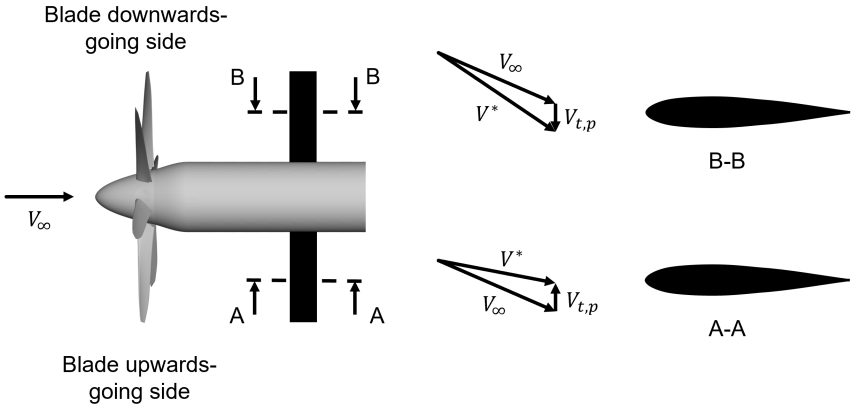

Figure 6.20: *SRV inflow conditions on the blade upwards- and downwards-going side when placed on the nacelle as seen by the vane (top-view)*

Swirl energy recovery is of interest for the future development of open-rotor propeller aircraft, which have a relatively high blade loading. The TUD-XPROP-S propeller used in this thesis has six blades, which have, compared to the desired design cases, a relatively low blade loading. This means that the swirl recovery and thus the added benefit of adding an SRV to future designs should be higher than can be determined with this model.

Another model consideration was the optimisation of the SRV blades. This was not done in this research for the reasons discussed in Chapter 5. Not optimising the vanes would result in a lower vane thrust and thus overall less efficient design. The final values are not absolute but can only be considered relative performance values.

Solver

The solver chosen for the aerodynamic analysis has a significant influence on the final results. Flightstream was chosen as a suitable lower-order solver as discussed in Section 3.2. This lower-order solver is less complex compared to more advanced CFD solvers, meaning that complex flow phenomena will not be captured. This reduced complexity does, however, also mean that the required computational time is reduced from hours to minutes[1]

The main difference between the analysis performed with Flightstream was observed when changing the surface proximity avoidance setting. This setting has been explained in detail in Section 4.1 and led to some uncertainty in the final results. The final results in this thesis are presented as the average values of each setting, as the real flow behaviour should be somewhere between these two methods of wake hand.

[1]https://www.darcorp.com/flightstream-aerodynamics-software

Another difference was observed in the method of calculating the spanwise lift distribution. Flightstream used the method of integrated circulation to determine the spanwise lift coefficient, and for local forces, a surface pressure integral. This difference is important when considering the surface and model component forces, as the total local velocities are used without considering the flow vectors. The method of integrated pressures would be affected by parallel flow components, such as cross flows, and therefore be less accurate within the propeller slipstream.

Conditions
The experiment was performed under specific conditions as discussed in Table 3.2, which were simulated for the analysis in Flightstream. The combination of advance ratio and a free stream velocity of 30 m/s means that the flight conditions are low-subsonic. A possible application of the tested SRVs and locations would be in the higher subsonic region, meaning that vane performance at different conditions could deviate from the relative differences found in this thesis.

6.6. Summary of Key Findings

The results shown in this chapter were divided into several sections, each considering a specific aspect of the Flightstream results. A summary of the key findings will be presented in this section based on these specific findings.

The SRV flow condition, described in Section 6.1, showed the axial and tangential inflow conditions for the initial and optimal SRV locations. The unsteady local angle of attack analysis showed that the AoA decreased when mowing further from the propeller. The axial local velocity was observed to be lower for the optimal vane placement but had a higher tangential inflow velocity, resulting in an overall higher vane thrust. A last important note is that the axial velocity of the 0.50 D configuration was higher compared to the vanes positioned on the nacelle, and that the tangential velocity was lower. This is caused by the wing, which increases the axial velocity of the flow over the upper surface of the wing, reducing the swirl.

Next, the surface pressure coefficients of the vanes were discussed in Section 6.2 with the SPA setting ON and OFF. The surface pressures were lower for the SPA setting OFF data as a result of higher induced velocities. The pressure coefficients on the vane located at –0.50 D were more negative, which is a consequence of the higher velocities as discussed in the previous paragraph. The vane trust contributions presented in Section 6.3 are directly related to the surface pressures, as Flightstream determines the model forces by integrating the surface pressures. Most optimal vane positions had higher vane thrust contributions except for the vane located at –0.75 D in case the SPA setting was turned OFF. This is most likely due to the propeller and vane interaction, as these geometries are located close to each other. The contributions of the vanes located at 0.50 D were negative as expected based on the inflow velocities and surface pressure data. The RISE configuration was the only configuration with several vanes, of which the vertical vane did not match the performance of the single vane at the same location in the –0.75 D configuration. This difference implies that the additional performance of several vanes can not be superimposed, as was also observed in the force factor contour plot shown in the same section.

The propulsive efficiency was discussed in Section 6.4, where both the individual component and combined model efficiencies were considered. The propeller was affected by the upstream effect of the vanes, especially for the –0.75 D vanes. The nacelle contribution was small and, depending on the SPA setting, either positive or negative. This was because of the integrated pressure method and defined nacelle and wing geometry. The last individual effect discussed was the wing, which was affected by the presence of the vanes. The combined effects result in an overall model axial propulsive efficiency. Both initial vane placements at –0.70 D and –0.25 D performed best with an approximate axial efficiency increase of approximately 3.80 %. The optimal vane efficiency was less compared to the initial location, which was attributed to the individual interaction effects. The overall efficiency of the vanes placed at 0.50 D was higher compared to the reference model, even though the vane thrust itself was negative. This is because of the interaction effect, where the wing performance increases and mitigates the additional drag of the vane. The RISE configuration performed better than the optimal vane location configurations, but was less effective than one vane.

Section 6.5 discussed the model, solver and conditions limitations. The combination of the discussed aspects results in a limited set of applicable situations for which the results of this thesis are valid. A relative comparison of the overall performance can be performed, but the limitations should be considered before extrapolating the results.

7

Conclusion and Recommendations

This chapter presents the conclusions to the posed research question stated at the beginning of this thesis in Section 7.1. Several recommendations for future research are presented in Section 7.2 based on the findings of this work.

7.1. Conclusion

This thesis report described how a lower-order aerodynamic solver was used to determine the swirl energy recovery effectiveness of swirl recovery vanes careful consideration of their placement. The research question was divided into multiple sub-questions, each focusing on a particular aspect related to this research question. The sub-questions, as stated in Section 1.1, are discussed below based on the results found in this thesis. The research question is then answered based on the discussed sub-questions.

Sub-question 1:

> *How well does a low-mid fidelity aerodynamic analysis tool capture the aerodynamic phenomena involved in the propeller slipstream?*

The first sub-question aimed to determine the accuracy of a lower-order aerodynamic analysis tool for the accurate modelling of the propeller slipstream and associated flow interactions. It was important to determine this, as this would be the foundation for all following aspects of this research. The aerodynamic solver of choice for this thesis was Flightstream, which was chosen based on the findings of previous research papers. A reference model with experimental data available was used to validate the solver, which was described in Chapter 4. This chapter started with a detailed explanation of the Surface Proximity Avoidance (SPA) setting, which had a significant effect on the final results. Both the SPA settings ON and OFF would not represent the slipstream's true behaviour, respectively under- and over-predicting the local induced velocities. Both settings have been used in this thesis as the real slipstream behaviour would be somewhere between these two extremes of wake handling.

Two main slipstream parameters were compared to experimental data to validate the solver. These parameters were the induced velocities at several analysis planes and the total pressure coefficient. The velocity ratios with in-plane velocity vectors captured the increase in propeller slipstream velocity. The velocities as determined by Flightstream were, however, lower compared to the experimental data. This was partially attributed to the fact that a small gap between the propeller and spinner was added to prevent solver divergence. A more detailed explanation could, however, not be given based on the available data. The

slipstream deformation, especially downstream of the model, was not captured accurately when compared to the experimental data.

The total pressure coefficient contour plots showed that Flightstream overestimated this parameter for both SPA settings. A possible reason for this is that Flightstream is an inviscid flow solver, which does not account for more complex flow phenomena such as wake mixing, which would reduce the total pressure. A potential flow solver, such as Flightstream, does not determine the total pressure directly, but is purely based on the local induced velocities. The presented total pressure data can thus only be used as an indication of the total pressure. The wake deformation was also not accurately captured with this parameter when the distance between the propeller and the analysis plane increased beyond the model geometry. It was observed from the propeller thrust values that Flightstream overestimates the propeller thrust as a result of the overestimated total pressures in the propeller slipstream.

The chordwise pressure and spanwise lift distributions, as discussed in the same chapter, show that the method of determining the pressure coefficient affects the Flightstream results. The pressure tab data from the experiment, located at ±0.7 y/R, were compared to the numerical data. The chordwise pressure in Flightstream is based on the incompressible pressure coefficient formula, which is only dependent on the local total induced velocities. The pressure coefficient can, according to this formula, not exceed 1.0. This has been addressed by Gothow et al. [45], who proposed a dynamic pressure correction in the propeller slipstream. This correction was applied to the numerical data, capturing the stagnation point much better. The numerical results with the SPA setting ON underestimated the chordwise pressures, as the wake elements close to the model surface were removed. The opposite effect was observed with the SPA setting OFF, which overestimated the pressure coefficients. Lastly, integrated pressure coefficients were compared to the spanwise lift coefficient plot from Flightstream. The different method used for the spanwise lift distribution and the lack of experimental data related to forces and coefficients made it difficult to compare this aspect with the results.

The aerodynamic flow phenomena in the propeller slipstream were, to some extent, captured by Flightstream. The results have a significant dependency on the surface proximity avoidance setting, but show similar behaviour for both settings. The total pressure coefficient results of Flightstream were less accurate, as were the chordwise pressures and spanwise lift distribution. The absolute performance of different configurations could thus not be determined. Only a comparative study, based on the relative performance of different configurations, would be possible.

Sub-question 2:

> *What is the effect of implementing Swirl Recovery Vanes on the overall propulsive efficiency of an aircraft with an open-rotor propeller?*

The second sub-question aimed to determine if the overall effect of placing an SRV would be beneficial for the total axial efficiency. This was done by placing an additional vane at different locations on the reference model. The results of an initial vane and optimised vane location for thrust show that an additional vane generates an axial thrust force. This contribution was found to be positive for the SRVs on the nacelle, but negative when placed on

the upper surface of the wing. The overall axial propulsive efficiency increased for all tested configurations as a result of flow interactions, which have been described in Chapter 6. The implementation of an SRV has, according to the findings of this research, the potential to increase the performance of current and future propeller-driven aircraft.

Sub-question 3:

> *Can the vane thrust contribution of individual SRVs, placed in the propeller slipstream, be added to accurately predict the overall aerodynamic performance of a multi-vane configuration?*

This sub-question considered if the performance of a single SRV could be superimposed to estimate the overall performance of a model with several vanes. The vane thrust contributions as presented in Section 6.3 showed the axial thrust for different configurations, where the last configuration, named RISE, had five vanes. SRV1 is located at the same location as the initial vanes in the –0.75 D configurations. It was observed that the vane thrust of the vane, at the same location, was lower in the RISE configuration. This indicates that there are interaction effects between the different vanes and model that affect the individual performance. This was also seen in the contour plots of the same location with and without an additional vane placed upstream of the analysis plane. It can thus be concluded that it is not possible to add the performance of individual vanes to determine the overall performance of a multi-vane configuration.

Sub-question 4:

> *What is the optimal SRV placement for the generation of thrust and propulsive efficiency?*

Three axial SRV positions were analysed for the optimal location of vane thrust and overall propulsive efficiency. Each of these axial locations represented a different design case. A first vane location would be directly behind the propeller. A second vane was placed between the propeller and the leading edge of the wing to determine the effect of increased axial distance between the propeller and SRV. A final vane position would be on the upper surface of the wing. An initial vertical vane and vane location for optimal thrust were determined for each of these axial positions. The optimal location for vane thrust was based on the force factor integral, as introduced in this work.

It was found that the single initial vertical vane located at –0.75 or –0.25 D performed the best with almost identical efficiency increments. It could thus be concluded that the axial distance between the propeller blades has no significant effect on the propulsive axial efficiency. This is in agreement with previous research papers, as discussed in Chapter 2, concluding the same. The configurations with optimised SRV positions produced more vane thrust, but performed overall worse due to flow interactions. The total axial efficiency values, as stated in the final section of the results, indicate that a single vane, strategically placed in the propeller slipstream, performed better than the RISE configuration with multiple vanes. This statement should be interpreted cautiously, as the results of the aerodynamic solver used during this thesis were not representative of the experimental data, which was discussed in the first research question.

Research Question:

To what extent can the effectiveness of swirl recovery design in open-rotor propeller aircraft be improved utilising a lower-order aerodynamic solver by implementation and careful placement of swirl recovery vanes on the nacelle or wing?

The sub-questions above allow for the formulation of a conclusion to the research question posed at the beginning of this thesis. The findings of this thesis indicate that the lower-order aerodynamic tool, used in this thesis, was not able to accurately capture the propeller slipstream effects. The induced velocity and total pressure coefficient data were respectively under- and overpredicted. Limited wake contraction and deformation were observed compared to the experimental data. Lastly, chordwise pressure and spanwise lift coefficients were difficult to validate due to the limited experimental data for these modelling aspects. The solver could, however, be used for a comparative study of the overall performance to determine what location is potentially worth investigating in more detail, even if the absolute performance parameters are not accurate.

The analyses of several vane locations on the reference model showed that an additional vane could contribute to the overall propulsive efficiency of a propeller-driven aircraft. The optimal position was found to be a vertical vane placed directly behind the propeller or slightly further aft, between the propeller and the leading edge of the wing, as the performance of these locations was very similar. Vane locations optimised for maximum thrust performed worse than the just-mentioned vertical vanes, likely due to interaction effects between the vane and model geometry. This can not be concluded definitively, given the accuracy limitations of the analysis tool. The RISE configuration with multiple vanes was overall less efficient compared to a single strategically placed vane, showing that specific vane design and positioning are important for the overall performance.

7.2. Recommendations

Based on the findings presented in this thesis report, several recommendations are proposed for future work. First, several recommendations regarding the aerodynamic solver are presented, after which some model aspects are considered. General recommendations for future research are described at the end of this section.

Flightstream recommendations

1. **Surface proximity avoidance setting**
   The surface proximity avoidance setting had a significant effect on the results. This setting has been described in detail, but some uncertainties remain regarding the correct implementation and physical implementation. It is recommended to perform a more detailed analysis with several models to better understand the exact implications of this setting before considering more complex model compositions.

2. **Model forces**
   The model forces in Flightstream are based on integrated pressures. It is recommended to check the forces predictions with experimental or a high-fidelity CFD solver to ensure that the solver is reliable. Such an analysis was unfortunately not possible during this research, as there were no model forces known for the reference model.

3. **Sensitivity study**
   This research focused on performing a comparative analysis between several configurations on the effectiveness of adding vanes. Flightstream allows for a lot of different settings to be changed, of which only the most significant settings could be considered during this research. It is recommended to perform a sensitivity study on most or all settings to confirm or determine the settings that reach the most accurate results.

Model recommendations

1. **Blade trailing edges**
   The reference model was sourced from an existing experimental geometric file to ensure that the same geometry was used as during the experiment. The propeller blades in this model featured blunt trailing edges, which could affect the stability and computational time of the analysis. For future analysis, it is recommended to modify the blade trailing edge to include a sharp trailing edge, preventing possible solver issues.

2. **Mesh**
   The mesh density affects the number of panels and thus the required computational time. The provided model geometry mesh used in this thesis was not optimised for numerical analysis, likely resulting in a longer computational time than necessary for the same accuracy. A mesh sensitivity study is recommended for future work to optimise the use of resources.

3. **Simplicity**
   The reference model for this thesis is based on an existing experimental model. The nacelle in this model is positioned with a relative angle of –5° to the wing, potentially influencing propeller-induced swirl and vane performance. It is recommended for future studies to use a simplified, axis-aligned configuration to prevent component misalignments.

4. **Advance ratio**
   The experimental data used in this study reflect a specific operating condition with a free stream velocity of 30 m/s and a propeller advance ratio of 0.8. The proposed application of the studied SRV concept is in the high subsonic region with higher blade loading, for which this research is not representative. Future research should investigate a range of flow conditions and propeller designs to confirm that the conclusions drawn in this thesis hold.

Research recommendation

1. **Blade optimisation**
   The SRV blades in this work have not been optimised, allowing for a better comparison between different configurations. Future work, considering the absolute performance of SRVs and their relative placement, should optimise the SRV blades to determine what the increase in total efficiency could be.
2. **Multiple vanes**
   It was found that the individual performance of vanes could not be added to estimate the overall performance of a configuration with multiple vanes. There is likely a configuration with more than one vane that is more efficient than the proposed single vane

in this research. It is for this reason that it is recommended for future work to analyse models with more than one vane.

3. **Model forces**
   The experimental data used in this research consisted of several analysis planes and two spanwise locations of pressure tabs. There was, however, no data available regarding the sectional or spanwise forces to compare these aspects of Flightstream to. It is suggested to use data from a high-fidelity CFD analysis or experiment with force measurements to compare these aspects of the Flightstream analysis.
4. **Highly loaded propeller**
   It was previously mentioned that only one set of flight conditions and propeller characteristics was analysed. This combination would represent a relatively lowly loaded propeller at low sub-sonic conditions, which does not match the conditions for which these SRVs are most interesting. High subsonic flight conditions and propellers with a higher blade loading are advised to be considered in future research to better represent the conditions for which the RISE engine was designed.
5. **SRV weight**
   Lastly, there is the structural consideration of adding one or more SRVs to a model. The SRV performance in this thesis research is assumed to be a direct effect of the design aspects and the flow components. This research does not include the structural impact of an additional vane, such as the required structural changes for the model or added weight. These aspects will play a role in a real application of SRVs and should therefore be considered in future research.

Bibliography

[1] R. Singh, G. Ameyugo and F. Noppel, *Jet engine design drivers: past, present and future*. Cranefield: Woodhead Publishing Limited, 2012, ch. 4, pp. 56–82, doi: https://doi.org/10.1533/9780857096098.1.56.

[2] R. Parker and M. Lathoud, "Green aero-engines: Technology to mitigate aviation impact on environment," *Proc. of the Institution of Mechanical Engineers, Part C: Journal of Mechanical Engineering Science*, vol. 224, pp. 529–538, 2010, doi: https://doi.org/10.1243/09544062JMES1515.

[3] T. Sinnige, A.M.N. Malgoezar, D. Ragni, K.Y.W. Scheper, M. Snellen, G. Eitelberg and L.L.M. Veldhuis, "APIAN-INF: a Low-Speed Aerodynamic and Aeroacoustic Investigation of Pylon-Pusher Propeller Interaction Effects," in *CEAS 2015: 5th CEAS Air and Space Conf.*, 2015.

[4] CFM international, "Revolutionary Innovation for Sustainable Engines (RISE)," 2021. [Online]. Available: https://www.cfmaeroengines.com/rise/

[5] T. Sinnige, J.J.A. Van Kuijk, K.P. Lynch, D. Ragni, G. Eitelberg and L.L.M. Veldhuis, "The effects of swirl recovery vanes on single - Rotation propeller aerodynamics and aeroacoustics," in *21st AIAA/CEAS Aeroacoustics Conf.*, 2016, doi: https://doi.org/10.2514/6.2015-2358.

[6] Y. Wang, Q. Li, G. Eitelberg, L.L.M. Veldhuis and M. Kotsonis, "Design and numerical investigation of swirl recovery vanes for the Fokker 29 propeller," *Chinese Journal of Aeronautics*, vol. 27, no. 5, pp. 1128–1136, 2014, doi: https://doi.org/10.1016/j.cja.2014.03.009.

[7] L.L.M. Veldhuis, "Propeller Wing Aerodynamic Interference," Ph.D. dissertation, TU Delft, 2005. [Online]. Available: https://resolver.tudelft.nl/uuid:8ffbde9c-b483-40de-90e0-97095202fbe3

[8] W.C. Strack, G. Knip, A.L. Weisbrich, J. Godston and E. Bradley, "Technology and Benefits of Aircraft Counter Rotation Propellers," in *Aerospace Cong. and Expo.*, 1982. [Online]. Available: https://ntrs.nasa.gov/citations/19830002859

[9] D.C. Mikkelson, G.A. Mitchell and L.J. Bober, "Summary of Recent NASA Propeller Research," in *AGARD Fluid Dynamics Panel Meeting on Aerodynamics and Acoustics of Propellers*, 1984. [Online]. Available: https://ntrs.nasa.gov/citations/19840024274

[10] J. Dominy and R.A. Midgley, "A transmission for the contra-rotating propfan powerplant," in *AIAA//SAE/ASEE 20th Joint Propulsion Conf.*, 1984, doi: https://doi.org/10.2514/6.1984-1196.

[11] J. Godston and F.J. Mike, "Evaluation of single and counter rotation gearboxes for propulsion systems," in *AIAA//SAE/ASEE 20th Joint Propulsion Conf.* AIAA, 1984, doi: https://doi.org/10.2514/6.1984-1195.

[12] L.L.M. Veldhuis, T.C.A. Stokkermans, T. Sinnige and G. Eitelberg, "Analysis of swirl recovery vanes for increased propulsive efficiency in tractor propeller aircraft,"

in *30th Congr. ICAS*, 2016. [Online]. Available: https://resolver.tudelft.nl/uuid:4823e070-7829-4666-bc82-db1282391bd1

[13] A. Stürmer, C.O.M. Gutierrez, E.M.R. Roosenboom, A. Schröder, R. Geislerm, D. Pallek, J. Agocs and K.P. Neitzke, "Experimental and numerical investigation of a contra rotating open-rotor flowfield," *Journal of Aircraft*, vol. 49, no. 6, pp. 1868–1877, 2012, doi: https://doi.org/10.2514/1.C031698.

[14] V.P. Blandeau and P.F. Joseph, "Broadband noise due to rotor-wake/rotor interaction in contra-rotating open rotors," *AIAA Journal*, vol. 48, no. 11, pp. 2674–2686, 2010, doi: https://doi.org/10.2514/1.J050566.

[15] Q. Li, "Towards optimum swirl recovery for propeller propulsion systems," Ph.D. dissertation, TU Delft, 2019, doi: https://doi.org/10.4233/uuid:ef966464-6b76-434d-b147-81ec247b023c.

[16] E. Obert, *Aerodynamic Design of Transport Aircraft*. Amsterdam: IOS Press, 2009, doi: https://doi.org/10.3233/978-1-58603-970-7-i.

[17] O. Bergmann, F.Götten and F. Janser, "Comparison and eveluation of blade elemetn methods agains RANS simulations and test data," *CEAS Aeronautical Journal*, 2022, doi: https://doi.org/10.1007/s13272-022-00579-1.

[18] A.F. Ribeiro, R.R. Duivenvoorden and D. Martins, "High-Fidelity Simulations of Propeller-Wing Interactions in High-Lift Conditions," in *AIAA AVIATION 2023 Forum*, 2023, doi: https://doi.org/10.2514/6.2023-3541.

[19] I. Samuelsson, "Experimental investigation of low speed model propeller slipstream }aerodynamic characteristics including flow field surveys and nacelle/wing static pressure measurements," in *Congr., 17th, Stockholm, Sweden*. ICAS, 1990, pp. 71–84.

[20] T.C.A. Stokkermans, "Aerodynamics of Propellers in Interaction Dominated Flowfields An Application to Novel Aerospace Vehicles," Ph.D. dissertation, TU Delft, 2020, doi: https://doi.org/10.4233/uuid:46178824-bb80-4247-83f1-dc8a9ca7d8e3.

[21] W.F. Philips, *Mechanics of flight*. New Jersey: John Wiley & Sons, Inc., 2004.

[22] Q. Li, X. Liu, G. Eitelberg and L.L.M. Veldhuis, "Numerical investigation of configurations with optimum swirl recovery for propeller propulsion systems," *AIAA Journal: devoted to aerospace research and development*, vol. 57, no. 4, pp. 1502–1513, 2019, doi: https://doi.org/10.2514/1.J057704.

[23] T.C.A. Stokkermans, "Design and Analysis of Swirl Recovery Vanes for an Isolated and a Wing Mounted Tractor Propeller," Master's thesis, TU-Delft, 2015. [Online]. Available: https://resolver.tudelft.nl/uuid:4ef56c0f-1dbd-4edb-8b89-f672dd3597ec

[24] T.C.A. Stokkermans, N. Van Arnhem and L.L.M. Veldhuis, "Mitigation of propeller kinetic energy losses with boundary layer ingestion and swirl recovery vanes," in *RAeS Applied Aerodynamics Conf.*, 2016. [Online]. Available: https://www.researchgate.net/publication/306359052_Mitigation_of_propeller_kinetic_energy_losses_with_boundary_layer_ingestion_and_swirl_recovery_vanes

[25] O. Yamamoto, "Numerical calculations of propfan/swirl recovery vane flow field," in *AIAA/ASME/SAE/ASEE 28th Joint Propulsion Conf. and Exhibit*, 1992, doi: https://doi.org/10.2514/6.1992-3771.

[26] C.J. Miller, "Euler Analysis of a Swirl Recovery Vane Design for Use With an Advanced Single-Rotation Propfan," in *24th Joint Proplusion Conf.*, 1899, doi: https://doi.org/10.2514/6.1988-3152.

[27] F. Avallone, L. van den Ende, Q. Li, D. Ragni, D. Casalino, G. Eitelberg and L.L.M. Veldhuis, "Aerodynamic and aeroacoustic effects of swirl recovery vanes length," *Journal of Aircraft*, 2019, doi: https://doi.org/10.2514/1.C035552.

[28] R.R. Duivenvoorden, N. Suard, T. Sinnige and L.L.M. Veldhuis, "Experimental Investigation of Aerodynamic Interactions of a Wing with Deployed Fowler Flap under Influence of a Propeller Slipstream," in *AIAA AVIATION 2022 Forum*, 2022, doi: https://doi.org/10.2514/6.2022-3216.

[29] R.R. Duivenvoorden, "Aerodynamic phenomena of propeller-wing-flap interaction," Ph.D. dissertation, TU-Delft, 2025, doi: https://doi.org/10.4233/uuid:1a705c0a-b0aa-4ddd-a350-8c663cf2fdb0.

[30] L.M.M. Boermans and P.B. Rutten, "Two-dimensional Aerodynamic Characteristics of Airfoil NLF-MOD22 with Fowler Flap," TU-Delft, Tech. Rep., 1995.

[31] J. Anderson, *Fundamentals of Aerodynamics*, 6th ed. MvGraw-Hill Education, 2011.

[32] B. Peerlings, "A review of aerodynamic flow models, solution methods and solvers-and their applicability to aircraft conceptual design literature study report," Master's thesis, TU Delft, 2018.

[33] N. van Arnhem, R. de Vries,T. Sinnige, R. Vos, G. Eitelberg and L.L.M. Veldhuis, "TUD-XPROP-S propeller geometry," Zenodo, 2022, doi: https://doi.org/10.5281/zenodo.6355669.

[34] F. Mariën, "Software Testing: VSPAERO," Master's thesis, HAW Hamburg, 2021, doi: https://doi.org/10.7910/DVN/0S1R14.

[35] E.E.A. Beyne, "Aerodynamic analysis of a propeller-powered strut-braced wing," Master's thesis, TU-Delft, 2023. [Online]. Available: https://resolver.tudelft.nl/uuid:581b8540-d67b-42a0-94cc-0a2523cfd0a9

[36] L. Prandtl, "Application of Modern Hydrodynamics to Aeronautics," NASA, Tech. Rep., 1923. [Online]. Available: https://ntrs.nasa.gov/citations/19930091180

[37] W.F. Phillips and D.O. Snyder, "Modern adaptation of Prandtl's classic lifting-line theory," *Journal of Aircraft*, vol. 37, no. 4, pp. 662–670, 2000, doi: https://doi.org/10.2514/2.2649.

[38] G. Ferraro, T. Kipouros, A.M. Savill, A. Rampurawala and C. Agostinelli, "Propeller-Wing Interaction Prediction for Early Design," in *52nd AIAA Aerospace Sciences Meeting - AIAA Science and Technology Forum and Expo., SciTech 2014*, 2014, doi: https://doi.org/10.2514/6.2014-0564.

[39] B. Sarıgöl, "An evaluation of methods and assumptions used in potential flow modelling of swirl recovery vanes," TU Delft, Bachelor thesis, 2023. [Online]. Available: https://resolver.tudelft.nl/uuid:f173b38c-7aae-4b30-b303-4df989e150f9

[40] P. Zinjarde, "Aerodynamic design integration of strut braced wings," Master's thesis, TU-Delft, 2023. [Online]. Available: https://resolver.tudelft.nl/uuid:b7b28c9c-6da8-42e3-90ce-99e4d524f1f0

[41] V. Ahuja and B.L. Litherland, "Comparison of Aerodynamic Analysis Tools Applied to a Propeller-Blown Wing," Research in Flight, Tech. Rep., 2023, doi: https://doi.org/10.2514/6.2023-1753.

[42] X. Fei, "Evaluation of a Commercial Surface Vorticity Flow Solver for the Modeling of Propeller-Wing Interaction," NASA, Tech. Rep., 2019, doi: https://doi.org/10.2514/6.2019-1046.

[43] N.J. Blaesser, "Propeller-Wing Integration on the Parallel Electric-Gas Architecture with Synergistic Utilization Scheme (PEGASUS) Aircraft," in *AIAA Scitech 2019 Forum*, 2019, doi: https://doi.org/10.2514/6.2019-1809.

[44] R.R. Duivenvoorden, T. Sinnige and L.L.M. Veldhuis, "Experimental dataset of a single propeller-wing-flap model (TUD-PWF) at various flap deflections, angles of attack and propeller conditions," 4TU.ResearchData, 2024, doi: https://doi.org/10.4121/3161b813-ad38-4f9c-bb9d-333b895f46bc.

[45] A. Gothow, F. Felicia J. Weiss, V. Ahuja and C. Gates, "Comparative Analysis: Validating FlightStream with Experimental Results of a High-Lift Configured Wing Model Equipped with Distributed Electric Propulsion," TU Berlin, Tech. Rep., 2024, doi: https://doi.org/10.2514/6.2024-3602.

[46] V. Ahuja and R.J. Hartfield, "Aerodynamic loads over arbitrary bodies by method of integrated circulation," *Journal of Aircraft*, vol. 53, no. 6, pp. 1719–1730, 2016.

[47] Q. Li, K. Öztürk, T. Sinnige, D. Ragni, G. Eitelberg, L.L.M. Veldhuis and Y. Wang, "Design and experimental validation of swirl-recovery vanes for propeller propulsion systems," *AIAA Journal: devoted to aerospace research and development*, vol. 56, no. 12, pp. 4719–4729, 2018, doi: https://doi.org/10.2514/1.J057113.

[48] F.I. Romli and M.A. Nasir, "Parametric Study of NACA 4-Series Airfoil Designs for Lift-to-Drag Performance," *Journal of Aeronautics, Astronautics and Aviation*, vol. 56, no. 1, pp. 85–92, 2024, doi: https://doi.org/10.6125/JoAAA.202403_56(1S).01.

A

Wing NLF-mod22(B) airfoil

This appendix presents the coordinates for the combined main element and fowler flap. These elements were combined with third-order polynomials to ensure smooth surface transitions. The x and y coordinates are non-dimensionalised with the chord length and describe the airfoil surface from trailing edge to trailing edge, first moving over the upper surface of the airfoil.

x/c	y/c	0.96550	0.01090	0.92963	0.01927
1.00000	0.00000	0.96489	0.01105	0.92901	0.01941
0.99941	0.00023	0.96427	0.01121	0.92839	0.01955
0.99882	0.00046	0.96366	0.01137	0.92777	0.01969
0.99822	0.00069	0.96304	0.01152	0.92715	0.01982
0.99763	0.00092	0.96242	0.01168	0.92653	0.01996
0.99704	0.00114	0.96181	0.01183	0.92591	0.02010
0.99644	0.00136	0.96119	0.01199	0.92529	0.02023
0.99585	0.00159	0.96058	0.01214	0.92467	0.02037
0.99525	0.00181	0.95996	0.01229	0.92405	0.02051
0.99466	0.00202	0.95934	0.01244	0.92343	0.02064
0.99406	0.00224	0.95872	0.01259	0.92281	0.02078
0.99346	0.00246	0.95811	0.01274	0.92219	0.02091
0.99286	0.00267	0.95749	0.01289	0.92157	0.02105
0.99226	0.00288	0.95687	0.01304	0.92095	0.02118
0.99167	0.00309	0.95626	0.01319	0.92033	0.02131
0.99107	0.00330	0.95564	0.01333	0.91971	0.02145
0.99047	0.00351	0.95502	0.01348	0.91909	0.02158
0.98986	0.00372	0.95440	0.01363	0.91847	0.02172
0.98926	0.00392	0.95378	0.01377	0.91784	0.02185
0.98866	0.00412	0.95317	0.01392	0.91722	0.02198
0.98806	0.00432	0.95255	0.01407	0.91660	0.02211
0.98746	0.00452	0.95193	0.01421	0.91598	0.02225
0.98685	0.00472	0.95131	0.01435	0.91536	0.02238
0.98625	0.00492	0.95069	0.01450	0.91474	0.02251
0.98564	0.00512	0.95007	0.01464	0.91412	0.02264
0.98504	0.00531	0.94945	0.01478	0.91350	0.02277
0.98444	0.00550	0.94884	0.01493	0.91287	0.02290
0.98383	0.00570	0.94822	0.01507	0.91225	0.02303
0.98322	0.00589	0.94760	0.01521	0.91163	0.02316
0.98262	0.00608	0.94698	0.01535	0.91101	0.02329
0.98201	0.00626	0.94636	0.01550	0.91039	0.02342
0.98140	0.00645	0.94574	0.01564	0.90976	0.02355
0.98080	0.00664	0.94512	0.01578	0.90914	0.02368
0.98019	0.00682	0.94450	0.01592	0.90852	0.02381
0.97958	0.00700	0.94388	0.01606	0.90790	0.02393
0.97897	0.00718	0.94326	0.01620	0.90728	0.02406
0.97836	0.00736	0.94264	0.01634	0.90665	0.02419
0.97775	0.00754	0.94203	0.01649	0.90603	0.02431
0.97714	0.00772	0.94141	0.01663	0.90541	0.02444
0.97653	0.00790	0.94079	0.01677	0.90479	0.02456
0.97592	0.00807	0.94017	0.01691	0.90416	0.02469
0.97531	0.00825	0.93955	0.01705	0.90354	0.02481
0.97470	0.00842	0.93893	0.01719	0.90292	0.02493
0.97409	0.00859	0.93831	0.01733	0.90229	0.02506
0.97348	0.00876	0.93769	0.01747	0.90167	0.02518
0.97287	0.00893	0.93707	0.01761	0.90105	0.02530
0.97225	0.00910	0.93645	0.01775	0.90042	0.02542
0.97164	0.00927	0.93583	0.01789	0.85000	0.03538
0.97103	0.00944	0.93521	0.01803	0.84824	0.03575
0.97042	0.00960	0.93459	0.01817	0.84649	0.03612
0.96980	0.00977	0.93397	0.01831	0.84473	0.03649
0.96919	0.00993	0.93335	0.01844	0.84297	0.03686
0.96858	0.01010	0.93273	0.01858	0.84122	0.03722
0.96796	0.01026	0.93211	0.01872	0.83946	0.03758
0.96735	0.01042	0.93149	0.01886	0.83770	0.03794
0.96673	0.01058	0.93087	0.01900	0.83594	0.03830
0.96612	0.01074	0.93025	0.01914	0.83418	0.03865

0.83242	0.03901	0.72993	0.05717	0.62713	0.07354
0.83066	0.03936	0.72816	0.05747	0.62535	0.07381
0.82890	0.03971	0.72639	0.05776	0.62358	0.07408
0.82714	0.04005	0.72462	0.05806	0.62181	0.07436
0.82538	0.04040	0.72285	0.05836	0.62003	0.07463
0.82362	0.04074	0.72108	0.05865	0.61826	0.07490
0.82186	0.04108	0.71931	0.05895	0.61648	0.07517
0.82009	0.04142	0.71754	0.05924	0.61471	0.07544
0.81833	0.04176	0.71577	0.05954	0.61293	0.07571
0.81657	0.04209	0.71400	0.05983	0.61116	0.07597
0.81480	0.04242	0.71222	0.06012	0.60938	0.07624
0.81304	0.04275	0.71045	0.06042	0.60761	0.07651
0.81127	0.04308	0.70868	0.06071	0.60583	0.07678
0.80951	0.04341	0.70691	0.06100	0.60406	0.07704
0.80775	0.04374	0.70514	0.06129	0.60228	0.07731
0.80598	0.04406	0.70337	0.06158	0.60051	0.07757
0.80421	0.04438	0.70160	0.06187	0.59873	0.07783
0.80245	0.04470	0.69983	0.06216	0.59696	0.07810
0.80068	0.04502	0.69806	0.06245	0.59518	0.07836
0.79892	0.04534	0.69628	0.06273	0.59341	0.07862
0.79715	0.04565	0.69451	0.06302	0.59163	0.07888
0.79538	0.04597	0.69274	0.06330	0.58986	0.07914
0.79361	0.04628	0.69097	0.06359	0.58808	0.07939
0.79185	0.04659	0.68920	0.06387	0.58630	0.07965
0.79008	0.04690	0.68742	0.06416	0.58453	0.07990
0.78831	0.04721	0.68565	0.06444	0.58275	0.08016
0.78654	0.04752	0.68388	0.06472	0.58097	0.08041
0.78477	0.04783	0.68211	0.06500	0.57920	0.08066
0.78301	0.04813	0.68033	0.06528	0.57742	0.08092
0.78124	0.04844	0.67856	0.06556	0.57564	0.08117
0.77947	0.04874	0.67679	0.06584	0.57386	0.08142
0.77770	0.04905	0.67502	0.06612	0.57209	0.08167
0.77593	0.04935	0.67324	0.06640	0.57031	0.08191
0.77416	0.04966	0.67147	0.06668	0.56853	0.08216
0.77239	0.04996	0.66970	0.06696	0.56675	0.08241
0.77062	0.05026	0.66792	0.06723	0.56498	0.08265
0.76886	0.05056	0.66615	0.06751	0.56320	0.08290
0.76709	0.05087	0.66438	0.06779	0.56142	0.08314
0.76532	0.05117	0.66260	0.06806	0.55964	0.08339
0.76355	0.05147	0.66083	0.06834	0.55786	0.08363
0.76178	0.05177	0.65906	0.06862	0.55609	0.08387
0.76001	0.05207	0.65728	0.06889	0.55431	0.08412
0.75824	0.05237	0.65551	0.06917	0.55253	0.08436
0.75647	0.05267	0.65373	0.06944	0.55075	0.08460
0.75470	0.05297	0.65196	0.06971	0.54897	0.08484
0.75293	0.05327	0.65019	0.06999	0.54719	0.08508
0.75116	0.05357	0.64841	0.07026	0.54541	0.08532
0.74939	0.05388	0.64664	0.07054	0.54364	0.08556
0.74762	0.05418	0.64487	0.07081	0.54186	0.08580
0.74585	0.05448	0.64309	0.07108	0.54008	0.08604
0.74408	0.05478	0.64132	0.07136	0.53830	0.08628
0.74231	0.05508	0.63954	0.07163	0.53652	0.08652
0.74055	0.05538	0.63777	0.07190	0.53474	0.08676
0.73878	0.05568	0.63600	0.07218	0.53296	0.08700
0.73701	0.05597	0.63422	0.07245	0.53118	0.08723
0.73524	0.05627	0.63245	0.07272	0.52941	0.08747
0.73347	0.05657	0.63068	0.07300	0.52763	0.08771
0.73170	0.05687	0.62890	0.07327	0.52585	0.08794

0.52407	0.08818	0.42066	0.10006	0.31673	0.10508
0.52229	0.08841	0.41887	0.10022	0.31493	0.10507
0.52051	0.08865	0.41708	0.10038	0.31314	0.10505
0.51873	0.08888	0.41530	0.10053	0.31134	0.10503
0.51695	0.08912	0.41351	0.10069	0.30955	0.10501
0.51517	0.08935	0.41172	0.10084	0.30775	0.10498
0.51339	0.08958	0.40993	0.10099	0.30596	0.10495
0.51161	0.08981	0.40814	0.10114	0.30416	0.10491
0.50983	0.09004	0.40635	0.10129	0.30237	0.10487
0.50805	0.09027	0.40457	0.10143	0.30057	0.10483
0.50627	0.09050	0.40278	0.10157	0.29878	0.10478
0.50449	0.09073	0.40099	0.10171	0.29699	0.10473
0.50271	0.09096	0.39920	0.10185	0.29519	0.10468
0.50093	0.09118	0.39741	0.10198	0.29340	0.10462
0.49915	0.09141	0.39562	0.10212	0.29160	0.10456
0.49737	0.09163	0.39383	0.10225	0.28981	0.10450
0.49559	0.09185	0.39204	0.10238	0.28802	0.10443
0.49381	0.09208	0.39025	0.10250	0.28622	0.10436
0.49203	0.09230	0.38846	0.10263	0.28443	0.10428
0.49024	0.09252	0.38667	0.10275	0.28264	0.10421
0.48846	0.09274	0.38488	0.10287	0.28085	0.10413
0.48668	0.09295	0.38308	0.10298	0.27905	0.10404
0.48490	0.09317	0.38129	0.10310	0.27726	0.10395
0.48312	0.09339	0.37950	0.10321	0.27547	0.10386
0.48134	0.09360	0.37771	0.10332	0.27368	0.10377
0.47955	0.09381	0.37592	0.10342	0.27188	0.10367
0.47777	0.09403	0.37413	0.10353	0.27009	0.10357
0.47599	0.09424	0.37233	0.10363	0.26830	0.10346
0.47421	0.09445	0.37054	0.10372	0.26651	0.10335
0.47242	0.09465	0.36875	0.10382	0.26472	0.10324
0.47064	0.09486	0.36696	0.10391	0.26293	0.10313
0.46886	0.09507	0.36517	0.10400	0.26113	0.10301
0.46708	0.09527	0.36337	0.10409	0.25934	0.10289
0.46529	0.09547	0.36158	0.10417	0.25755	0.10276
0.46351	0.09568	0.35979	0.10425	0.25576	0.10263
0.46173	0.09588	0.35799	0.10432	0.25397	0.10250
0.45994	0.09607	0.35620	0.10440	0.25218	0.10237
0.45816	0.09627	0.35441	0.10447	0.25039	0.10223
0.45637	0.09647	0.35261	0.10453	0.24861	0.10209
0.45459	0.09666	0.35082	0.10460	0.24682	0.10194
0.45281	0.09686	0.34903	0.10466	0.24503	0.10179
0.45102	0.09705	0.34723	0.10471	0.24324	0.10164
0.44924	0.09724	0.34544	0.10476	0.24145	0.10148
0.44745	0.09743	0.34364	0.10481	0.23966	0.10132
0.44567	0.09762	0.34185	0.10486	0.23788	0.10116
0.44388	0.09780	0.34006	0.10490	0.23609	0.10099
0.44210	0.09798	0.33826	0.10494	0.23430	0.10082
0.44031	0.09817	0.33647	0.10497	0.23252	0.10065
0.43853	0.09835	0.33467	0.10500	0.23073	0.10047
0.43674	0.09853	0.33288	0.10503	0.22895	0.10029
0.43495	0.09870	0.33108	0.10505	0.22716	0.10010
0.43317	0.09888	0.32929	0.10507	0.22538	0.09991
0.43138	0.09905	0.32749	0.10508	0.22359	0.09971
0.42959	0.09923	0.32570	0.10509	0.22181	0.09952
0.42781	0.09940	0.32390	0.10510	0.22002	0.09931
0.42602	0.09956	0.32211	0.10510	0.21824	0.09911
0.42423	0.09973	0.32031	0.10510	0.21646	0.09890
0.42245	0.09990	0.31852	0.10509	0.21468	0.09868

0.21290	0.09846	0.11101	0.07775	0.01883	0.03109
0.21112	0.09824	0.10930	0.07722	0.01751	0.02987
0.20934	0.09801	0.10758	0.07668	0.01621	0.02864
0.20756	0.09778	0.10587	0.07614	0.01493	0.02737
0.20578	0.09755	0.10416	0.07559	0.01368	0.02608
0.20400	0.09731	0.10246	0.07504	0.01246	0.02477
0.20222	0.09706	0.10075	0.07447	0.01128	0.02342
0.20044	0.09681	0.09905	0.07390	0.01012	0.02205
0.19867	0.09656	0.09735	0.07332	0.00901	0.02064
0.19689	0.09630	0.09566	0.07274	0.00793	0.01920
0.19511	0.09604	0.09396	0.07214	0.00690	0.01774
0.19334	0.09577	0.09227	0.07154	0.00590	0.01624
0.19156	0.09550	0.09058	0.07093	0.00495	0.01472
0.18979	0.09523	0.08890	0.07032	0.00405	0.01317
0.18802	0.09495	0.08721	0.06969	0.00319	0.01159
0.18625	0.09467	0.08553	0.06906	0.00239	0.00999
0.18447	0.09438	0.08386	0.06842	0.00163	0.00836
0.18270	0.09409	0.08218	0.06777	0.00096	0.00670
0.18093	0.09379	0.08051	0.06711	0.00041	0.00499
0.17916	0.09349	0.07885	0.06645	0.00003	0.00324
0.17739	0.09319	0.07719	0.06577	-0.00011	0.00145
0.17563	0.09288	0.07553	0.06508	0.00005	-0.00034
0.17386	0.09256	0.07387	0.06439	0.00049	-0.00207
0.17209	0.09225	0.07222	0.06368	0.00114	-0.00375
0.17033	0.09192	0.07058	0.06296	0.00194	-0.00535
0.16856	0.09160	0.06894	0.06223	0.00288	-0.00688
0.16680	0.09127	0.06730	0.06149	0.00393	-0.00833
0.16504	0.09093	0.06568	0.06074	0.00510	-0.00970
0.16327	0.09059	0.06405	0.05997	0.00635	-0.01098
0.16151	0.09024	0.06243	0.05920	0.00768	-0.01219
0.15975	0.08989	0.06082	0.05841	0.00908	-0.01331
0.15799	0.08954	0.05921	0.05761	0.01053	-0.01437
0.15623	0.08918	0.05761	0.05680	0.01202	-0.01537
0.15448	0.08881	0.05602	0.05598	0.01355	-0.01630
0.15272	0.08844	0.05443	0.05514	0.01511	-0.01719
0.15097	0.08807	0.05285	0.05429	0.01670	-0.01802
0.14921	0.08769	0.05127	0.05344	0.01831	-0.01882
0.14746	0.08730	0.04970	0.05257	0.01994	-0.01957
0.14571	0.08691	0.04814	0.05168	0.02159	-0.02029
0.14396	0.08651	0.04658	0.05079	0.02324	-0.02098
0.14221	0.08611	0.04503	0.04989	0.02491	-0.02163
0.14046	0.08570	0.04349	0.04897	0.02659	-0.02226
0.13872	0.08528	0.04195	0.04804	0.02828	-0.02287
0.13697	0.08486	0.04042	0.04710	0.02998	-0.02345
0.13523	0.08443	0.03890	0.04615	0.03169	-0.02402
0.13349	0.08400	0.03739	0.04518	0.03339	-0.02456
0.13175	0.08356	0.03589	0.04420	0.03511	-0.02509
0.13001	0.08311	0.03439	0.04320	0.03683	-0.02561
0.12827	0.08266	0.03291	0.04219	0.03855	-0.02611
0.12654	0.08220	0.03144	0.04116	0.04028	-0.02660
0.12480	0.08173	0.02998	0.04012	0.04201	-0.02708
0.12307	0.08126	0.02854	0.03905	0.04374	-0.02755
0.12134	0.08077	0.02711	0.03797	0.04547	-0.02801
0.11962	0.08029	0.02569	0.03687	0.04721	-0.02846
0.11789	0.07979	0.02428	0.03575	0.04895	-0.02890
0.11617	0.07929	0.02290	0.03462	0.05069	-0.02933
0.11445	0.07878	0.02152	0.03346	0.05244	-0.02975
0.11273	0.07827	0.02017	0.03228	0.05419	-0.03017

0.05593	-0.03057	0.15873	-0.04665	0.26239	-0.05600
0.05768	-0.03097	0.16051	-0.04686	0.26419	-0.05612
0.05943	-0.03136	0.16229	-0.04706	0.26598	-0.05625
0.06119	-0.03175	0.16408	-0.04726	0.26777	-0.05638
0.06294	-0.03213	0.16586	-0.04746	0.26956	-0.05650
0.06470	-0.03250	0.16764	-0.04766	0.27135	-0.05662
0.06645	-0.03287	0.16943	-0.04786	0.27314	-0.05675
0.06821	-0.03323	0.17121	-0.04805	0.27493	-0.05687
0.06997	-0.03359	0.17300	-0.04825	0.27672	-0.05699
0.07173	-0.03394	0.17478	-0.04844	0.27851	-0.05711
0.07349	-0.03429	0.17656	-0.04863	0.28030	-0.05722
0.07525	-0.03463	0.17835	-0.04881	0.28209	-0.05734
0.07702	-0.03497	0.18014	-0.04900	0.28388	-0.05746
0.07878	-0.03530	0.18192	-0.04918	0.28567	-0.05757
0.08054	-0.03562	0.18371	-0.04936	0.28746	-0.05769
0.08231	-0.03595	0.18549	-0.04954	0.28926	-0.05780
0.08408	-0.03626	0.18728	-0.04972	0.29105	-0.05791
0.08584	-0.03658	0.18906	-0.04989	0.29284	-0.05802
0.08761	-0.03688	0.19085	-0.05007	0.29463	-0.05813
0.08938	-0.03719	0.19264	-0.05024	0.29642	-0.05824
0.09115	-0.03749	0.19442	-0.05041	0.29821	-0.05835
0.09292	-0.03778	0.19621	-0.05058	0.30000	-0.05845
0.09469	-0.03807	0.19800	-0.05074	0.30180	-0.05856
0.09646	-0.03836	0.19979	-0.05091	0.30359	-0.05866
0.09824	-0.03864	0.20157	-0.05107	0.30538	-0.05877
0.10001	-0.03892	0.20336	-0.05123	0.30717	-0.05887
0.10178	-0.03919	0.20515	-0.05140	0.30896	-0.05897
0.10356	-0.03946	0.20694	-0.05156	0.31076	-0.05907
0.10533	-0.03972	0.20872	-0.05171	0.31255	-0.05917
0.10711	-0.03999	0.21051	-0.05187	0.31434	-0.05927
0.10889	-0.04025	0.21230	-0.05203	0.31613	-0.05936
0.11066	-0.04050	0.21409	-0.05218	0.31792	-0.05946
0.11244	-0.04075	0.21588	-0.05234	0.31972	-0.05955
0.11422	-0.04100	0.21766	-0.05249	0.32151	-0.05965
0.11599	-0.04125	0.21945	-0.05264	0.32330	-0.05974
0.11777	-0.04150	0.22124	-0.05279	0.32509	-0.05983
0.11955	-0.04174	0.22303	-0.05294	0.32689	-0.05992
0.12133	-0.04198	0.22482	-0.05309	0.32868	-0.06001
0.12311	-0.04222	0.22661	-0.05324	0.33047	-0.06010
0.12489	-0.04245	0.22839	-0.05338	0.33226	-0.06018
0.12667	-0.04269	0.23018	-0.05353	0.33406	-0.06027
0.12845	-0.04292	0.23197	-0.05367	0.33585	-0.06036
0.13023	-0.04315	0.23376	-0.05382	0.33764	-0.06044
0.13201	-0.04338	0.23555	-0.05396	0.33943	-0.06052
0.13379	-0.04361	0.23734	-0.05410	0.34123	-0.06060
0.13557	-0.04384	0.23913	-0.05425	0.34302	-0.06068
0.13735	-0.04406	0.24092	-0.05439	0.34481	-0.06076
0.13913	-0.04428	0.24271	-0.05453	0.34661	-0.06084
0.14091	-0.04451	0.24450	-0.05466	0.34840	-0.06092
0.14269	-0.04473	0.24629	-0.05480	0.35020	-0.06099
0.14447	-0.04495	0.24808	-0.05494	0.35200	-0.06107
0.14625	-0.04516	0.24987	-0.05507	0.35379	-0.06114
0.14803	-0.04538	0.25166	-0.05521	0.35558	-0.06122
0.14982	-0.04560	0.25344	-0.05534	0.35737	-0.06129
0.15160	-0.04581	0.25523	-0.05548	0.35916	-0.06136
0.15338	-0.04602	0.25702	-0.05561	0.36095	-0.06143
0.15516	-0.04623	0.25881	-0.05574	0.36275	-0.06149
0.15694	-0.04644	0.26060	-0.05587	0.36454	-0.06156

0.36633	-0.06163	0.47041	-0.06360	0.57447	-0.06138
0.36812	-0.06169	0.47220	-0.06360	0.57626	-0.06128
0.36992	-0.06176	0.47399	-0.06360	0.57805	-0.06118
0.37171	-0.06182	0.47579	-0.06359	0.57984	-0.06108
0.37351	-0.06188	0.47758	-0.06359	0.58163	-0.06098
0.37530	-0.06194	0.47938	-0.06358	0.58343	-0.06087
0.37710	-0.06200	0.48117	-0.06357	0.58522	-0.06077
0.37889	-0.06206	0.48297	-0.06357	0.58701	-0.06066
0.38068	-0.06212	0.48476	-0.06356	0.58880	-0.06055
0.38248	-0.06217	0.48656	-0.06355	0.59059	-0.06044
0.38427	-0.06223	0.48835	-0.06354	0.59238	-0.06033
0.38606	-0.06228	0.49015	-0.06352	0.59417	-0.06021
0.38786	-0.06234	0.49194	-0.06351	0.59596	-0.06009
0.38965	-0.06239	0.49374	-0.06350	0.59776	-0.05998
0.39145	-0.06244	0.49553	-0.06348	0.59955	-0.05986
0.39324	-0.06249	0.49733	-0.06347	0.60134	-0.05973
0.39503	-0.06254	0.49912	-0.06345	0.60313	-0.05961
0.39683	-0.06259	0.50092	-0.06343	0.60492	-0.05948
0.39862	-0.06264	0.50271	-0.06341	0.60671	-0.05935
0.40042	-0.06268	0.50450	-0.06339	0.60850	-0.05922
0.40221	-0.06273	0.50630	-0.06337	0.61029	-0.05909
0.40401	-0.06277	0.50809	-0.06335	0.61208	-0.05895
0.40580	-0.06281	0.50989	-0.06333	0.61387	-0.05881
0.40759	-0.06285	0.51168	-0.06331	0.61565	-0.05866
0.40939	-0.06290	0.51348	-0.06328	0.61744	-0.05852
0.41118	-0.06293	0.51527	-0.06326	0.61923	-0.05836
0.41298	-0.06297	0.51707	-0.06323	0.62102	-0.05821
0.41477	-0.06301	0.51886	-0.06321	0.62281	-0.05805
0.41657	-0.06305	0.52066	-0.06318	0.62459	-0.05788
0.41836	-0.06308	0.52245	-0.06315	0.62638	-0.05771
0.42015	-0.06312	0.52425	-0.06312	0.62817	-0.05753
0.42195	-0.06315	0.52604	-0.06309	0.62995	-0.05735
0.42374	-0.06318	0.52783	-0.06305	0.63174	-0.05717
0.42554	-0.06321	0.52963	-0.06302	0.63352	-0.05698
0.42733	-0.06324	0.53142	-0.06298	0.63531	-0.05678
0.42913	-0.06327	0.53322	-0.06294	0.63709	-0.05658
0.43092	-0.06330	0.53501	-0.06290	0.63887	-0.05637
0.43272	-0.06333	0.53681	-0.06285	0.64065	-0.05615
0.43451	-0.06335	0.53860	-0.06281	0.64244	-0.05593
0.43631	-0.06338	0.54039	-0.06276	0.64422	-0.05571
0.43810	-0.06340	0.54219	-0.06271	0.64600	-0.05548
0.43989	-0.06342	0.54398	-0.06266	0.64777	-0.05524
0.44169	-0.06344	0.54578	-0.06260	0.64955	-0.05500
0.44348	-0.06346	0.54757	-0.06255	0.65133	-0.05475
0.44528	-0.06348	0.54936	-0.06249	0.65311	-0.05450
0.44707	-0.06350	0.55116	-0.06242	0.65488	-0.05424
0.44887	-0.06351	0.55295	-0.06236	0.65666	-0.05398
0.45066	-0.06353	0.55474	-0.06229	0.65843	-0.05371
0.45246	-0.06354	0.55654	-0.06222	0.66021	-0.05344
0.45425	-0.06355	0.55833	-0.06215	0.66198	-0.05316
0.45605	-0.06356	0.56012	-0.06207	0.66375	-0.05288
0.45784	-0.06357	0.56192	-0.06199	0.66553	-0.05260
0.45964	-0.06358	0.56371	-0.06191	0.66730	-0.05231
0.46143	-0.06359	0.56550	-0.06183	0.66907	-0.05201
0.46323	-0.06359	0.56730	-0.06174	0.67084	-0.05171
0.46502	-0.06360	0.56909	-0.06165	0.67261	-0.05141
0.46682	-0.06360	0.57088	-0.06156	0.67437	-0.05110
0.46861	-0.06360	0.57267	-0.06147	0.67614	-0.05078

0.67791	-0.05046	0.74823	-0.03489	0.78398	-0.02601
0.67967	-0.05014	0.74884	-0.03473	0.78459	-0.02587
0.68144	-0.04981	0.74946	-0.03458	0.78521	-0.02572
0.68320	-0.04947	0.75007	-0.03442	0.78583	-0.02557
0.68496	-0.04912	0.75068	-0.03426	0.78645	-0.02542
0.68672	-0.04877	0.75130	-0.03409	0.78706	-0.02527
0.68848	-0.04841	0.75191	-0.03393	0.78768	-0.02512
0.69023	-0.04804	0.75253	-0.03377	0.78830	-0.02497
0.69199	-0.04767	0.75314	-0.03361	0.78891	-0.02482
0.69374	-0.04728	0.75376	-0.03345	0.78953	-0.02467
0.69549	-0.04689	0.75437	-0.03329	0.79015	-0.02452
0.69724	-0.04648	0.75499	-0.03314	0.79077	-0.02437
0.69760	-0.04640	0.75561	-0.03298	0.79138	-0.02422
0.72037	-0.04125	0.75622	-0.03282	0.79200	-0.02407
0.72099	-0.04114	0.75683	-0.03267	0.79262	-0.02392
0.72162	-0.04103	0.75745	-0.03252	0.79323	-0.02377
0.72225	-0.04092	0.75807	-0.03236	0.79385	-0.02362
0.72287	-0.04081	0.75868	-0.03221	0.79447	-0.02347
0.72349	-0.04069	0.75930	-0.03205	0.79509	-0.02332
0.72412	-0.04056	0.75991	-0.03190	0.79570	-0.02317
0.72474	-0.04044	0.76053	-0.03174	0.79632	-0.02302
0.72536	-0.04031	0.76115	-0.03159	0.79694	-0.02287
0.72598	-0.04018	0.76176	-0.03143	0.79755	-0.02272
0.72660	-0.04005	0.76238	-0.03128	0.79817	-0.02257
0.72723	-0.03992	0.76300	-0.03113	0.79879	-0.02242
0.72785	-0.03978	0.76361	-0.03097	0.79941	-0.02227
0.72847	-0.03965	0.76423	-0.03082	0.80002	-0.02212
0.72909	-0.03951	0.76484	-0.03067	0.80064	-0.02197
0.72971	-0.03937	0.76546	-0.03052	0.80126	-0.02182
0.73033	-0.03923	0.76608	-0.03036	0.80187	-0.02167
0.73095	-0.03909	0.76670	-0.03021	0.80249	-0.02152
0.73156	-0.03895	0.76731	-0.03006	0.80311	-0.02137
0.73218	-0.03881	0.76793	-0.02991	0.80373	-0.02123
0.73280	-0.03866	0.76855	-0.02976	0.80434	-0.02108
0.73342	-0.03852	0.76916	-0.02961	0.80496	-0.02093
0.73404	-0.03837	0.76978	-0.02946	0.80558	-0.02078
0.73466	-0.03823	0.77040	-0.02931	0.80620	-0.02063
0.73528	-0.03808	0.77101	-0.02915	0.80681	-0.02048
0.73589	-0.03793	0.77163	-0.02900	0.80743	-0.02033
0.73651	-0.03779	0.77225	-0.02885	0.80805	-0.02019
0.73713	-0.03764	0.77287	-0.02870	0.80867	-0.02004
0.73775	-0.03749	0.77348	-0.02855	0.80928	-0.01989
0.73836	-0.03734	0.77410	-0.02840	0.80990	-0.01975
0.73898	-0.03719	0.77471	-0.02825	0.81052	-0.01960
0.73960	-0.03704	0.77533	-0.02810	0.81114	-0.01946
0.74021	-0.03689	0.77595	-0.02795	0.81176	-0.01931
0.74083	-0.03674	0.77657	-0.02780	0.81238	-0.01917
0.74145	-0.03658	0.77719	-0.02765	0.81299	-0.01902
0.74206	-0.03643	0.77780	-0.02751	0.81361	-0.01888
0.74268	-0.03628	0.77842	-0.02736	0.81423	-0.01873
0.74330	-0.03613	0.77904	-0.02721	0.81485	-0.01859
0.74391	-0.03597	0.77965	-0.02706	0.81547	-0.01845
0.74453	-0.03582	0.78027	-0.02691	0.81609	-0.01831
0.74515	-0.03567	0.78089	-0.02676	0.81671	-0.01816
0.74576	-0.03551	0.78151	-0.02661	0.81733	-0.01802
0.74638	-0.03536	0.78212	-0.02646	0.81795	-0.01788
0.74699	-0.03520	0.78274	-0.02631	0.81856	-0.01774
0.74761	-0.03505	0.78336	-0.02616	0.81918	-0.01760

0.81980	-0.01746	0.85592	-0.01025	0.89230	-0.00447
0.82042	-0.01733	0.85655	-0.01013	0.89293	-0.00440
0.82104	-0.01719	0.85717	-0.01001	0.89356	-0.00432
0.82166	-0.01705	0.85780	-0.00990	0.89419	-0.00425
0.82228	-0.01692	0.85842	-0.00978	0.89482	-0.00417
0.82291	-0.01678	0.85904	-0.00967	0.89545	-0.00410
0.82353	-0.01665	0.85967	-0.00955	0.89608	-0.00403
0.82415	-0.01651	0.86030	-0.00944	0.89671	-0.00396
0.82477	-0.01638	0.86092	-0.00932	0.89734	-0.00388
0.82539	-0.01625	0.86155	-0.00921	0.89798	-0.00381
0.82601	-0.01611	0.86217	-0.00910	0.89861	-0.00374
0.82663	-0.01598	0.86279	-0.00898	0.89924	-0.00367
0.82725	-0.01585	0.86342	-0.00887	0.89987	-0.00361
0.82787	-0.01572	0.86404	-0.00876	0.90050	-0.00354
0.82850	-0.01559	0.86467	-0.00865	0.90113	-0.00347
0.82912	-0.01546	0.86530	-0.00853	0.90176	-0.00340
0.82974	-0.01533	0.86592	-0.00842	0.90240	-0.00333
0.83036	-0.01520	0.86655	-0.00831	0.90303	-0.00327
0.83098	-0.01507	0.86717	-0.00820	0.90366	-0.00320
0.83160	-0.01495	0.86780	-0.00810	0.90429	-0.00314
0.83223	-0.01482	0.86842	-0.00799	0.90492	-0.00307
0.83285	-0.01469	0.86905	-0.00788	0.90555	-0.00301
0.83347	-0.01457	0.86968	-0.00777	0.90619	-0.00294
0.83409	-0.01444	0.87030	-0.00767	0.90682	-0.00288
0.83472	-0.01432	0.87093	-0.00756	0.90745	-0.00281
0.83534	-0.01419	0.87155	-0.00745	0.90808	-0.00275
0.83596	-0.01407	0.87218	-0.00735	0.90871	-0.00269
0.83659	-0.01394	0.87281	-0.00725	0.90934	-0.00262
0.83721	-0.01382	0.87343	-0.00714	0.90998	-0.00256
0.83783	-0.01370	0.87406	-0.00704	0.91061	-0.00250
0.83846	-0.01358	0.87469	-0.00694	0.91124	-0.00244
0.83908	-0.01345	0.87532	-0.00684	0.91187	-0.00238
0.83970	-0.01333	0.87594	-0.00674	0.91250	-0.00231
0.84032	-0.01321	0.87657	-0.00664	0.91314	-0.00225
0.84095	-0.01309	0.87720	-0.00654	0.91377	-0.00219
0.84157	-0.01297	0.87782	-0.00645	0.91440	-0.00213
0.84220	-0.01285	0.87845	-0.00635	0.91503	-0.00207
0.84282	-0.01273	0.87908	-0.00626	0.91567	-0.00201
0.84344	-0.01261	0.87971	-0.00616	0.91630	-0.00195
0.84407	-0.01249	0.88034	-0.00607	0.91693	-0.00189
0.84469	-0.01237	0.88097	-0.00598	0.91756	-0.00183
0.84531	-0.01225	0.88159	-0.00588	0.91820	-0.00177
0.84594	-0.01213	0.88222	-0.00579	0.91883	-0.00171
0.84656	-0.01201	0.88285	-0.00571	0.91946	-0.00166
0.84719	-0.01189	0.88348	-0.00562	0.92009	-0.00160
0.84781	-0.01177	0.88411	-0.00553	0.92073	-0.00154
0.84843	-0.01165	0.88474	-0.00544	0.92136	-0.00148
0.84906	-0.01154	0.88537	-0.00536	0.92199	-0.00143
0.84968	-0.01142	0.88600	-0.00527	0.92263	-0.00137
0.85031	-0.01130	0.88663	-0.00519	0.92326	-0.00131
0.85093	-0.01118	0.88726	-0.00511	0.92389	-0.00126
0.85155	-0.01107	0.88789	-0.00502	0.92452	-0.00120
0.85218	-0.01095	0.88852	-0.00494	0.92516	-0.00115
0.85280	-0.01083	0.88915	-0.00486	0.92579	-0.00110
0.85343	-0.01071	0.88978	-0.00478	0.92642	-0.00104
0.85405	-0.01060	0.89041	-0.00470	0.92705	-0.00099
0.85468	-0.01048	0.89104	-0.00463	0.92769	-0.00094
0.85530	-0.01036	0.89167	-0.00455	0.92832	-0.00088

0.92895	-0.00083	0.96573	0.00104
0.92958	-0.00078	0.96637	0.00105
0.93022	-0.00073	0.96700	0.00106
0.93085	-0.00068	0.96764	0.00106
0.93148	-0.00063	0.96827	0.00107
0.93212	-0.00058	0.96891	0.00107
0.93275	-0.00053	0.96954	0.00108
0.93338	-0.00049	0.97018	0.00108
0.93402	-0.00044	0.97081	0.00108
0.93465	-0.00039	0.97145	0.00108
0.93529	-0.00034	0.97208	0.00108
0.93592	-0.00030	0.97272	0.00108
0.93655	-0.00025	0.97335	0.00108
0.93719	-0.00021	0.97399	0.00108
0.93782	-0.00017	0.97462	0.00107
0.93845	-0.00012	0.97526	0.00107
0.93908	-0.00008	0.97590	0.00106
0.93972	-0.00004	0.97653	0.00105
0.94035	0.00000	0.97717	0.00104
0.94099	0.00004	0.97780	0.00103
0.94162	0.00008	0.97844	0.00102
0.94225	0.00012	0.97907	0.00101
0.94289	0.00016	0.97971	0.00100
0.94352	0.00020	0.98034	0.00099
0.94416	0.00024	0.98098	0.00097
0.94479	0.00027	0.98161	0.00096
0.94542	0.00031	0.98225	0.00094
0.94606	0.00035	0.98288	0.00092
0.94669	0.00038	0.98352	0.00090
0.94733	0.00041	0.98415	0.00088
0.94796	0.00045	0.98478	0.00086
0.94860	0.00048	0.98542	0.00084
0.94923	0.00051	0.98605	0.00081
0.94986	0.00054	0.98669	0.00079
0.95050	0.00057	0.98732	0.00076
0.95113	0.00060	0.98796	0.00074
0.95177	0.00063	0.98859	0.00071
0.95240	0.00065	0.98923	0.00068
0.95304	0.00068	0.98986	0.00065
0.95367	0.00071	0.99049	0.00062
0.95431	0.00073	0.99113	0.00058
0.95494	0.00076	0.99176	0.00055
0.95558	0.00078	0.99240	0.00052
0.95621	0.00080	0.99303	0.00048
0.95684	0.00083	0.99367	0.00044
0.95748	0.00085	0.99430	0.00040
0.95811	0.00087	0.99493	0.00036
0.95875	0.00089	0.99557	0.00032
0.95938	0.00090	0.99620	0.00028
0.96002	0.00092	0.99683	0.00024
0.96065	0.00094	0.99747	0.00019
0.96129	0.00095	0.99810	0.00015
0.96192	0.00097	0.99873	0.00010
0.96256	0.00098	0.99937	0.00005
0.96319	0.00100	1.00000	0.00000
0.96383	0.00101		
0.96446	0.00102		
0.96510	0.00103		

B

Blade Element-like Sectional Lift Code

The Blade element-like sectional lift code used for this thesis research is relatively simple. This appendix discusses the general setup of the code and how it was used.

A representation of how this code was set up can be seen in Figure B.1. The input variables for this code are related to the radial inflow conditions and vane parameters. The inflow conditions for this thesis were taken from a previous research paper as presented by Li et al. [47]. The author of this paper tested several NACA 4-series airfoils, which were defined in the input. The $C_l - \alpha$ and $C_d - \alpha$ for each airfoil were determined with an external 2D aerodynamic programme called XFOIL[1]. The correct implementation of this external analysis tool was checked manually for several NACA 4-series airfoils.

The discretised vane, in combination with the inflow conditions and lift and drag coefficient data, allowed for the lift and thrust forces to be calculated with 2D aerodynamic force equations. These forces are then integrated over the span to determine the vane forces and thrust, which was verified by performing several simple integrations on known integral functions. The total vane thrust could be compared to the results of the research papers discussed.

[1]XFOIL Subsonic Airfoil Development System by M. Drela, H. Youngren, version 6.99 (2000).

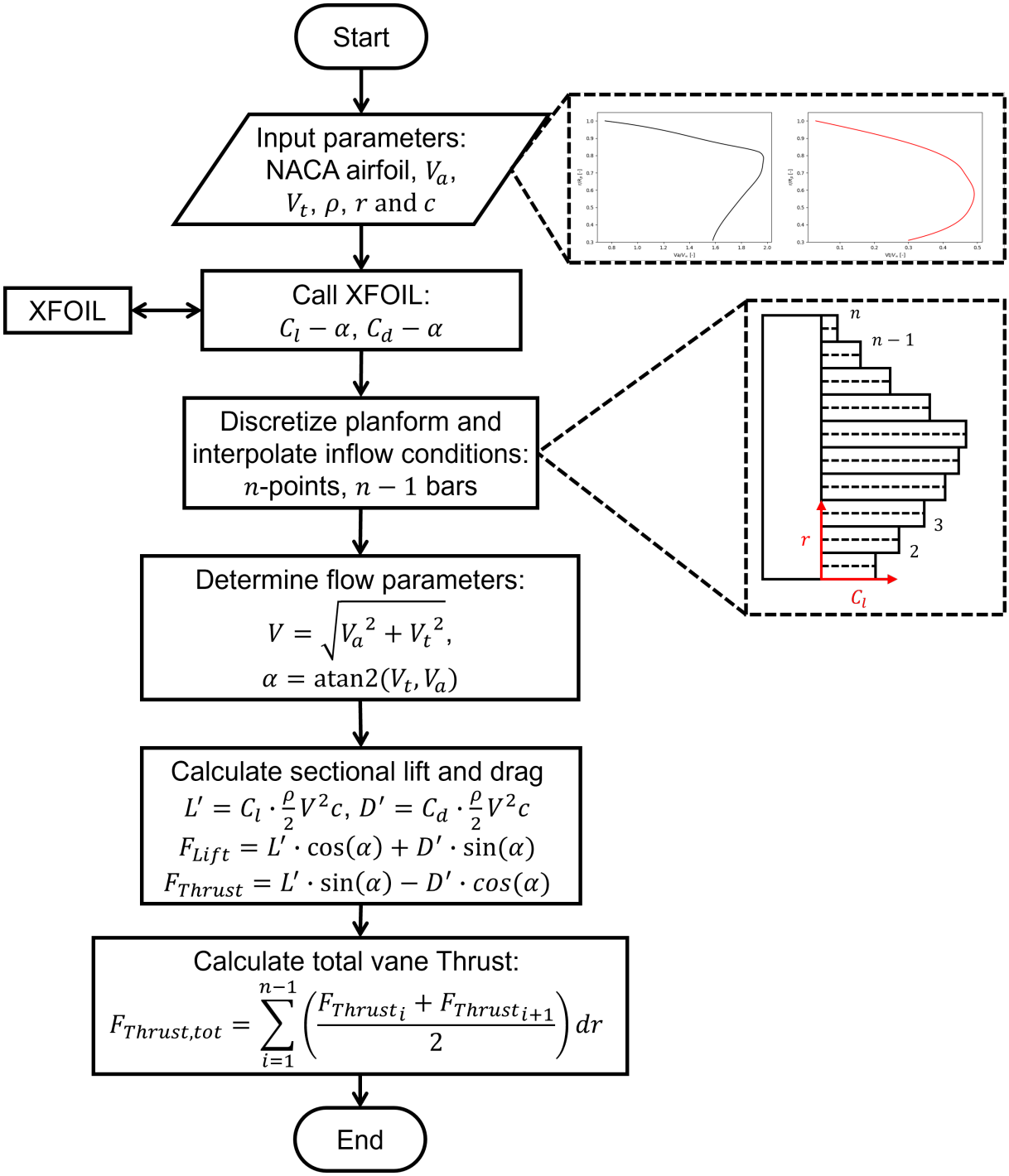

Figure B.1: *Flowchart of the blade element-like sectional lift code used in this thesis research*